

Development of Analytical Methods to Characterize Organic Aerosol
And Black Carbon

by

Yiyi Wei, B. S.

A Dissertation

In

CHEMISTRY

Submitted to the Graduate Faculty
of Texas Tech University in
Partial Fulfillment of
the Requirements for
the Degree of

DOCTOR OF PHILOSOPHY

Approved

Jonathan E. Thompson
Chair of Committee

Dimitri Pappas

Yehia Mechref

Mark Sheridan
Dean of the Graduate School

May, 2014

Copyright 2014, Yiyi Wei

ACKNOWLEDGMENTS

I would first like to express my appreciation to my research advisor, Dr. Jonathan Thompson, for his patient guidance and encouragement throughout the past four years in Texas Tech University. I have learned a lot from him in both class and lab. His diligent and persistent in research will encourage me all my life.

I am also grateful to Dr. Pappas and Dr. Mechref for serving as my committee members and providing me valuable suggestions in many aspects.

I also wish to thank my group members: Hao Tang, Kathy Dial, Haley Redmond, Fang Qian, Lulu Ma, Tingting Cao and Qing Zhang, for their help in both research and daily life.

At last, I would like to thank my parents and friends for their support, love, and encouragement to finish my Ph. D. program.

TABLE OF CONTENTS

ACKNOWLEDGMENTS	ii
ABSTRACT.....	vi
LIST OF TABLES	viii
LIST OF FIGURES	ix
LIST OF ABBREVIATIONS	xii
I. INTRODUCTION.....	1
1.1 A General Description of Atmospheric Aerosols	1
1.1.1 Importance of Studying Aerosols	1
1.1.2 Size Distribution and Growth of Aerosols.....	2
1.2 Composition of Aerosols	2
1.2.1 Organic Aerosols	3
1.2.1.1 Volatile Organic Compounds (VOCs).....	3
1.2.1.2 Kinetics of VOCs	3
1.2.1.3 Gas-to-particle Phase Partitioning and Viscosity	4
1.2.1.4 Measurement Techniques for Organic Aerosol.....	5
1.2.2 Black Carbon (BC)	6
1.2.2.1 Measurement Techniques of Black Carbon	7
1.2.3 Inorganic Aerosols	9
1.3 Optical Properties of Atmospheric Aerosols	11
1.4 Motivation of dissertation work.....	12
II. THE CHEMICAL EVOLUTION & PHYSICAL PROPERTIES OF ORGANIC AEROSOL: A MOLECULAR STRUCTURE BASED APPROACH.....	21
2.1 Introduction.....	21
2.2 Methods.....	23
2.2.1 The 3D Coordinate System	23
2.2.2 Test Compound Database & QSPR Modeling.....	23
2.2.3 Squalene Ozonolysis Experiment	24
2.2.4 Ambient Aerosol Sampling.....	25
2.2.5 High-resolution Mass Analysis.....	26
2.2.6 Assigning Molecular Formulas.....	26
2.3 Results and discussion	27
2.3.1 Advantages of The Approach	27

2.3.2 Prediction of Physical & Chemical Properties.....	28
2.3.3 Prediction of Chemical Reactivity	30
2.3.4 Comparison of 3D Approach to Alternate Schemes.....	30
2.3.5 Properties of Chamber & Ambient Organic Aerosol.....	32
2.3.6 General Trends: Similarity between Aerosol Types	34
2.3.7 Current Limitations & Future Directions.....	35
2.4 Acknowledgments.....	36
III. LIGHT SCATTERING AND EXTINCTION MEASUREMENTS COMBINED WITH LASER-INDUCED INCANDESCENCE FOR THE REAL-TIME DETERMINATION OF SOOT MASS ABSORPTION CROSS SECTION.....	44
3.1 Introduction.....	44
3.2 Methods.....	46
3.2.1 Description of Optical Measurements Using the Aerosol Albedometer with Laser-induced Incandescence.	46
3.2.2 Scanning Mobility Particle Sizing (SMPS) and Particle Size Selection.....	48
3.2.3 Transmission Electron Microscopy (TEM) Analysis.	48
3.2.4 Generation & Characteristics of Soot and Ambient Sampling.....	49
3.2.5 Thermal Denuding.	50
3.3 Results and Discussion	50
3.3.1 LII Response Function and Effect of Coating/Mixing State.	50
3.3.2 Consequences of the LII Measurement: ns-Soot Morphology Changes	52
3.3.3 Effect of Coating/Mixing State on ns-Soot M.A.C.....	54
3.3.4 M.A.C. Values for Dispersed Kerosene ns-Soot and Ambient Aerosol.....	56
3.4 Conclusions.....	56
3.5 Acknowledgments.....	57
IV. ATMOSPHERIC BLACK CARBON CAN EXHIBIT ENHANCED LIGHT ABSORPTION AT HIGH RELATIVE HUMIDITY	65
4.1 Introduction.....	65
4.2 Experimental methods.	66
4.2.1 Sampling conditions.....	66
4.2.2 Measurements	67
4.3 Results and Discussion	68
4.3.1 BC Mixing State Analysis	68
4.3.2 BC Size and Mass Concentration	69
4.3.3 Optical Measurement Results	69
4.3.3.1 Mechanism of Enhanced Absorption.....	72
4.4 Significance and Conclusion.....	74

4.5 Acknowledgement	74
V. CONCLUSION AND FUTURE WORK	85
APPENDICES	88
A. SUPPLEMENTARY INFORMATION FOR CHAPTER II.....	88
B. SUPPLEMENTARY FIGURES FOR CHAPTER III.....	92
C. SUPPLEMENTARY FIGURES FOR CHAPTER IV.....	98
REFERENCE.....	102

ABSTRACT

Aerosols in the atmosphere are ranging from nm to μm size, which can not only absorb and scatter sunlight, but also reduce visibility and cause health problems. In this dissertation research we present a comprehensive introduction of aerosol in order to thoroughly understand its properties. In addition, a molecular structure based model is developed to characterize organic aerosol. Furthermore, optical data of black carbon is presented in this dissertation to illustrate its light-absorbing properties.

Chapter II shows coupling a 3-dimensional coordinate system defined by the molecular descriptors of molecular weight, heteroatom mass, and double bond equivalents (D.B.E.) with high-resolution molecular mass spectrometry is a powerful approach for describing key properties of the organic aerosol. The scheme is conceptually simple, yet maintains sufficient complexity to be compatible with quantitative structure-property relationships (QSPRs) used to predict chemical and physical properties that govern aerosol behavior. From available data, both ambient organic aerosol and laboratory generated organic aerosol frequently occupy the region characterized by <10 D.B.E. <600 M.W. and <200 heteroatom mass. A QSPR analysis conducted illustrates spatial trends within the 3D space for volatility and Henry's law constants for 31,000 organic compounds considered.

In Chapter III an aerosol albedometer was combined with laser-induced incandescence (LII) to achieve simultaneous measurements of aerosol scattering, extinction coefficient, and soot mass concentration. Thermo-denuder experiments showed the LII signals were not affected by the particle mixing state when laser peak power was 1.5 – 2.5 MW. Fresh kerosene nanosphere soot (ns-soot) exhibited a mean mass absorption cross section (M.A.C) and standard deviation of $9.3 \pm 2.7 \text{ m}^2 / \text{g}$ while limited measurements on dry ambient aerosol yielded an average of $8.2 \pm 5.9 \text{ m}^2 / \text{g}$ when soot was $> 0.25 \mu\text{g} / \text{m}^3$. The method also detected increases in M.A.C. values associated with enhanced light absorption when polydisperse, laboratory generated ns-soot particles were embedded within or coated with ammonium nitrate, ammonium sulfate, and glycerol. Glycerol coatings produced the largest fractional increase in M.A.C. (1.41 fold increase),

while solid coatings of ammonium sulfate and ammonium nitrate produced increases of 1.10 and 1.06, respectively. Fresh, ns-soot did not exhibit increased M.A.C. at high relative humidity (R.H.), however, lab generated soot coated with ammonium nitrate and held at 85% R.H. exhibited M.A.C. values nearly double the low humidity case. The hybrid instrument for simultaneously tracking soot mass concentration and aerosol optical properties in real-time is a valuable tool for probing enhanced absorption by soot at atmospherically relevant concentrations.

Chapter IV shows that hygroscopic growth of atmospheric aerosol particles sampled at Houston, TX leads to an enhancement in both light scattering and absorption. Measurements suggest light absorption increases roughly three-four fold at high ambient humidity for coated soot particles. However, when the fraction of coated BC particles was reduced, the absorption enhancement was also reduced, suggesting coatings are crucial for the effect to occur. In addition, the extent to which MAC was increased at high humidity varied considerably over time, even for BC that consistently presented as being coated. This suggests the chemical composition of the coating and/or source of BC may also be an important parameter to constrain MAC enhancement at high humidity. Nonetheless, the results are largely consistent with previous laboratory and model results predicting absorption enhancement. We conclude that the enhanced absorption increases the warming effect of soot aerosol aloft, and global climate models should include parameterizations for RH effects to accurately describe absorptive heating by BC.

LIST OF TABLES

1.1	Natural and anthropogenic emission of atmospheric aerosol	14
2.1	Properties of compounds that are located at identical coordinates of alternate classification schemes. Every compound on this list can be resolved in the 3D coordinate system presented in this work.	37
3.1	Observed enhancement in soot mass absorption cross-section (m^2/g) as a function of mixing state and coating material.	59
4.1	Mean aerosol optical values observed at Houston, TX for dried aerosol (RH < 60%) during 19-24 July 2013	76
A.1	Best-fit parameters for prediction of vapor pressure.	88

LIST OF FIGURES

1.1	Global radiative forcing of climate between 1750 and 2005.	15
1.2	Size distribution of a typical atmospheric aerosol. DGV means volume median diameter; σ_g means geometric standard deviation	16
1.3	Pie charts show the average composition and mass concentration in different site of the world	17
1.4	Schematic of Single Particle Soot Photometer (SP2).	18
1.5	Schematic of refinement PILS.	19
1.6	Schematic of Cavity Ring-down Spectroscopy (CRDS).	20
2.1	Distribution of common organic components of atmospheric aerosol in the 3D space. The dimensions were chosen to effectively sort organic matter in aerosol by volatility, polarity, water solubility, and reactivity.	38
2.2	Reaction trajectories in the 3D space. Knowledge of an expected or proposed reaction mechanism allows prediction of the reaction trajectory in the 3D space.	39
2.3	Physical and chemical properties of organic compounds can be correlated to coordinates in the 3D space. Plots for vapor pressure (A), and Henry's law constant (B).	40
2.4	Plots of QSPR predicted rate constants for reaction with hydroxyl radical (OH) (A,B), and ozonolysis rate constant (C,D) for test compounds considered in this study.	41
2.5	Distribution of squalene (black), isoprene (blue) and limonene (red) secondary organic aerosol (SOA) in the 3D space.	42
2.6	<i>Center</i> – Distribution of organic matter observed for ambient aerosols in the 3D coordinate system. <i>Right</i> – Histograms of molecular weight and DBE distributions for the samples. Biomass data, Fresno fog data, and rainwater data. <i>Left</i> – The figures on the top left illustrate the distribution of all observed peaks from the combined data set through element specific filters.	43
3.1	Experimental apparatus.	60
3.2	Observed LII response as a function of coating state for (A) ammonium nitrate coated soot at low humidity, (B) glycerol-coated soot, (C) ambient aerosol, and (D) ammonium nitrate coated soot at various relative humidities.	61
3.3	(A) Observed size distributions of fresh kerosene ns-soot at various laser fluences. (B) TEM images of lased and unlased kerosene ns-	

soot. (C) High-resolution TEM images of fresh ns-soot that has been lased and nonlased ns-soot.	62
3.4 Plot of experimental data in time for atomized glycerol plus ns-soot..	63
3.5 Effect of relative humidity on M.A.C. value for (A) fresh kerosene ns-soot and (B) atomized BC internally mixed with ammonium nitrate.....	64
4.1 Experimental setup for field measurements at Houston, TX.....	77
4.2 Left – Hygroscopic growth factor (G.F) model employed in this study (red) compared to select observational data. Right – Correction factor for integrating sphere nephelometer derived from hygroscopic growth model and Qian et al.....	78
4.3 Laboratory validation of lag time analysis to assess rBC mixing state. Data is for fresh, uncoated kerosene lamp soot and atomized kerosene lamp soot coated with ammonium sulfate, ammonium nitrate, and glycerol.....	79
4.4 (A) Daily average size distributions of rBC cores sampled at Houston, TX as reported by the SP2. (B) Time series plot of BC coat fraction and mass concentration with histograms summarizing the data..	80
4.5 Plot of observed mass scattering coefficient vs. relative humidity for aerosol sampled in Houston, TX during 19–24 July 2013.....	81
4.6 Data collected during 19–24 July 2013 at Houston TX that exhibit rapid changes in observed absorption enhancement due to RH.....	82
4.7 Observed soot MAC at $\lambda = 532$ nm vs. RH and coating state for all data.	83
4.8 (A) Modeled electric field within and near a 2 micron water droplet. (B) Plot of modeled soot MAC vs. the shell diameter or water sphere diameter for the core-shell and sphere-on-sphere models.....	84
A.1 Plots of the vapor pressure predicted by the 3 parameter fit vs. the QSPR predicted values for the training set data.	89
A.2 Histograms of the difference between QSPR predicted and parameterized prediction of the logarithm of vapor pressure for the various subsets of data.	90
A.3 Box plot of results for error in vapor pressure predictions for 380 test compounds containing C,H,and O.	91
B.1 Thermogravimetric analysis (TGA) of fresh kerosene ns-soot used in this study.	92

B.2	Observed LII responses vs. indicated BC concentration as measured using the PSAP.....	93
B.3	(a) Histogram of observed aerosol absorption coefficient (b_{abs} , Mm^{-1}) during the ambient monitoring at Lubbock, TX during May 2013. (b) Histogram of observed BC mass concentrations ($\mu\text{g}/\text{m}^3$) during the ambient monitoring at Lubbock, TX during May 2013. (c) Histogram of observed SSA during the ambient monitoring at Lubbock, TX during May 2013. (d) Histogram of observed aerosol extinction coefficient (b_{ext} , Mm^{-1}) during the ambient monitoring at Lubbock, TX during May 2013. (e) Histogram of observed aerosol scatter coefficient (b_{scat} , Mm^{-1}) during the ambient monitoring at Lubbock, TX during May 2013.....	96
B.4	(A) Indicated size distribution of BC cores for atomized kerosene soot suspensions used in this study. (B) Size distribution of scattering particles for the same atomized kerosene soot suspensions.	97
C.1	Laboratory calibration of SP2 after the field campaign.....	98
C.2	Evaluation of possible “brown carbon” interference. UV-VIS Spectra of filter extracts collected from Houston, TX and a spectroscopic blank (black).	99
C.3	NOAA HYSPLIT Back Trajectory Analysis during the sampling period.....	100
C.4	Uncertainty analysis that accompanies Figure 4.7 of this work. Figure C.4 presents propagated absolute uncertainty in MAC vs. coat fraction and RH.	101

LIST OF ABBREVIATIONS

AE	Angstrom Exponent
AMS	Aerosol Mass Spectrometry
BC	Black Carbon
CCN	Cloud Condensation Nuclei
CPC	Condensation Particle Counter
CRDS	Cavity Ring-Down Spectroscopy
DBE	Double Bond Equivalent
DMA	Differential Mobility Analyzer
DRF	Direct Radiative Forcing
EC	Element Carbon
EPA	Environmental Protection Agency
GC	Gas Chromatography
IPCC	Intergovernmental Panel On Climate Change
LC	Liquid Chromatography
LII	Laser-Induced Incandescence
MAC	Mass Absorption Cross section
OC	Organic Carbon
PAH	Polycyclic Aromatic Hydrocarbon
PILS	Particle Into Liquid Sampler
PMT	Photomultiplier Tube
POA	Primary Organic Aerosol
PSAP	Particle Soot Absorption Photometer
QSPR	Quantative Structure Property Relationship

RH	Relative Humidity
SMPS	Scanning Mobility Particle Sizing
SOA	Secondary Organic Aerosol
SP2	Single Particle Soot Photometer
TCEQ	Texas Commission on Environmental Quality
TEM	Transmission Electron Microscopy
TGA	Thermo-Gravimetric Analysis
VOC	Volatile Organic Aerosol
RH	Relative Humidity

CHAPTER I

INTRODUCTION

1.1 A General Description of Atmospheric Aerosols

Aerosols are nm- μ m size particles suspended in the atmosphere. These particles can be either liquids or solids and are ubiquitous in our environment.¹ Aerosols are challenging to study as they have wide range of size distributions, extremely complex composition, very limited sample mass and multi-phase characteristics that simultaneously allows heterogeneous phase chemistry and complicates study of diffusion and mass transfer.

1.1.1 Importance of Studying Aerosols

Atmospheric aerosols can contribute to climate modification since they absorb and scatter sunlight. These effects directly alter the energy flux at the surface of earth by removing or reflecting solar radiation.² The Intergovernmental Panel on Climate Change (I.P.C.C.) estimate of direct radiative forcing by aerosols is -0.55 W/m^2 which compares to $+2.5 \text{ W/m}^2$ for greenhouse gas warming.³ Figure 1.1 shows the global radiative forcing of climate between 1750 and 2005.

Aerosols can also alter climate through indirect effects which relate to cloud formation and lifetime. Aerosols serve as cloud condensation nuclei (CCN), and the number concentration of aerosols determine the number of CCN. This can alter the size distribution of cloud water drops, which affects cloud lifetime and optical properties. For instance, *Andreae et al.* found that cloud droplet diameters decreased from 24 to 12 micron over the Amazon when clouds were mixed with biomass burning aerosol.⁴ This shift in size distribution makes clouds more efficient back-scatters of sunlight, and would be expected to cool climate. The I.P.C.C. estimate for this indirect forcing effect is currently -0.7 W/m^2 with high uncertainty.³

On the other hand, aerosols can also cause health problems. Evidence shows that most of ambient aerosols are inhalable. Once they enter into the human body, they will adhere to the throat and lung tissue. In some cases, these aerosols may damage the

respiratory system of humans and eventually result in dysfunction.⁵ For instance, *Gauderman et al.* found the Forced Vital Capacity (FVC), corresponding to number and size of alveoli decreased by 105.2 ml in high air pollution areas compared with normal air quality regions, indicating deficit of lung function.⁶ In addition, polluted aerosols may even cause cardiovascular disease.⁷ Moreover, investigation shows the hospitalization pattern changed due to emission of excess aerosols, such as PM_{2.5} by which excess risk of 4.1% has been found, 3.4% excess risk of organic aerosols are indicated.⁸ Birth weight is also related to the aerosol pollution that increasing the exposure to organic aerosols for nine month pregnancy result in an average of 17.1 grams decrease in birth weight.⁹

1.1.2 Size Distribution and Growth of Aerosols

Ambient aerosols have a wide range of size distribution owing to formation mechanisms. Physical and mechanical processes (abrasive and windblown dispersion of mineral dust or sea spray) generally result in larger, coarse mode (>2.5 micron diam.) particles. Fine mode (< 2.5 micron diam.) particles are produced through chemical processes. The fine mode can be further subdivided into nucleation and accumulation mode. Nucleation mode particles are the smallest, with diameters < 10 nm. These aerosols have high diffusion coefficients, and can rapidly coagulate and enter the accumulation mode. Accumulation mode particles have sizes >100 nm diameter, and slower diffusion. However, these particles can continue to grow in size as volatile material from the gas-phase deposits onto their surfaces.¹⁰ Figure 1.2 below illustrates a typical size distribution of atmospheric aerosol.

1.2 Composition of Aerosols

The chemical composition of ambient aerosols is diverse and varies by location and formation process. Primary particles are introduced directly into the atmosphere and common examples include wind-blown dust, sea-spray and elemental carbon (e.g. soot). A large quantity of coarse mineral dust aerosol comprised of earth-oxides is often present in windy, arid regions such as Lubbock. However, over the oceans sea-spray aerosol (mainly chloride and sulfate salts) is more abundant. Secondary aerosol is generated through chemical reactions in the atmosphere. Common secondary aerosol phase

materials include ammonium sulfate, ammonium nitrate, and an unknown fraction of organic carbon.¹⁰ Table 1.1 below shows the annual flux of both natural and anthropogenic aerosols emitted to the atmosphere. This table is reproduced from data reported in Intergovernmental Panel on Climate Changes (I.P.C.C). The relative proportions of concentration between aerosol types are not always the same and a variety of chemical or physical processes can change the composition of aerosols after dispersion in the air.^{1,10} Figure 1.3 below shows the averaging composition of aerosols in different site.

1.2.1 Organic Aerosols

Organic aerosol accounts for approximate 50% of all ambient aerosols. *Spracklen et al.* estimated the 50-380 Tg/yr formation of SOA with high uncertainty.^{11, 12} It is believed primary organic aerosol (POA) can be directly emitted from biomass burning, fossil fuel burning, suspension of soil and dust, and cooking. The major compounds of POA are alkanes, alkanolic acids and polycyclic aromatic hydrocarbons (PAHs).¹³ Secondary organic aerosol (SOA) is mainly produced by gas-phase oxidation of volatile organic compounds (VOCs), or by heterogeneous reactions on particle surfaces. In addition, VOCs can react with radicals such as OH, NO_x and O₃, forming products that are functionalized with hydroxyl, carbonyl, carboxyl groups and other heteroatoms.^{13, 14}

1.2.1.1 Volatile Organic Compounds (VOCs)

The Environmental Protection Agency (EPA) defines the VOC as the organic compound having a boiling point up to 260 °C at atmospheric pressure. Sources of anthropogenic VOCs include biomass burning, industrial processes and fossil fuel combustion. An estimate of anthropogenic VOC emissions is 186 Tg / yr.¹⁵ However, biogenic VOCs contribute to the emission of approximate 442 Tg / yr which consists of soil, vegetation, and oceanic sources.¹⁵

1.2.1.2 Kinetics of VOCs

VOC is prone to react with oxidants; examples are OH, O₃, NO₃, NO_x, etc. Understanding the reaction kinetics of these processes is important for us to better

estimate the lifetime of compounds under specific conditions. Aerosols are aged by OH and O₃ radicals, the major oxidants, during daytime and nighttime with the rate constant reaching the magnitude of 10⁻¹² cm³ molecule⁻¹ s⁻¹. The concentration of OH in the daytime is about 10⁶ radical cm⁻³, and for O₃ is 40-80 ppb. Lifetime of aerosols are varied, for example, alkanes have lifetimes of 2-30 days, except methane, whose lifetime is 10 years; alkenes have lifetime ranging from 0.4 to 4 days.¹⁵ However NO₃ radical can only play a role at nighttime since it will absorb visible light and photodissociate. Reacting with NO₃ is often somewhat slower, as rate constants as small as 10⁻¹⁸ cm³ molecule⁻¹ s⁻¹ are often observed.¹⁶

1.2.1.3 Gas-to-particle Phase Partitioning and Viscosity

Phase partitioning is related to the volatility of VOCs. High volatility organic compounds (HVOCs) appear predominately in gas phase, and often have high reactivity. These substances can be aged by OH or O₃ on a timescale of minutes to hours. However, low volatility organic compounds (LVOCs) tend to stay in the condensed phases. These molecules are often encompassed in the core of particles which makes reaction with gas-phase oxidants difficult. Semi-volatile organic compounds will be detected in both gas and condensed phases and are often treated through models of reversible partitioning.¹⁴ Following are the equations of partition coefficient ξ_i :

$$\xi_i = \left(1 + \frac{C_i^*}{C_{oA}}\right)^{-1}; \quad C_{oA} = \sum_i C_i \xi_i \quad (1)$$

In this equation, C_i^* is the effective saturation concentration, C_{oA} is the total mass concentration of organic aerosols, and ξ_i indicates the fraction of compound i found in the condensed phase.¹⁷ So when $C_i^* > C_{oA}$, ξ_i is smaller than 0.5 which means more than half fraction of compounds will exist in the gas phase. In contrast, if $C_i^* < C_{oA}$, more compounds will stay in the condensed phase.

Viscosity is another important physical property of organic aerosols, and it has a very close relate to the diffusion coefficient D_{org} :

$$D_{org} = \frac{kT}{6\pi a \nu} \quad (2)$$

Where k is Boltzmann constant ($1.38 \times 10^{-23} \text{J K}^{-1}$), T is temperature (K), a is effective molecule radius (m), and ν is the dynamic viscosity (Pa s).¹⁸ Since the viscosity of aerosols is much smaller in liquid compared with in solid, the diffusion is much rapid in liquid, and much slower in solid.

1.2.1.4 Measurement Techniques for Organic Aerosol.

Many techniques are involved to measure organics in particles.¹⁹⁻²¹ A major technique is aerosol time-of-flight mass spectrometry (ATOFMS). *Prather et al.* contributed a great deal in developing ATOFMS.^{22, 23} In this method, a laser is used to both vaporize and ionize aerosols. Aerodynamic particle size is measured based on the transit time between two laser beams, and then the complete particle composition is derived from time-of-flight mass spectrometer. A variety of similar techniques have been developed,²⁴⁻²⁶ for example, *Huffman et al.* contributed to the design of Aerodyne aerosol mass spectrometer (AAMS).²⁷⁻²⁹ *Jimenez et al.* developed Quadrupole Aerosol Mass Spectrometer (Q-AMS).^{30, 31} In general, these techniques often use electron impact ionization (EI) which causes fragmentation.

Electrospray ionization mass spectrometry (ESI-MS) is recently used to measure molecules of organic aerosols. ESI is a soft ionization mode generating less fragmentation of analytes, therefore more complete molecular characterization can be derived.^{32, 33} For instance, *Smith et al.* use ESI-MS to identify biomass burning samples. They acquire the molecular formula such as $\text{C}_5\text{H}_8\text{N}_2$, $\text{C}_4\text{H}_{10}\text{O}_3$, etc.^{34, 35} High resolution can be obtained when ESI combined with Fourier transform ion cyclotron resonance mass spectrometry (FT-ICR MS). It provides ultrahigh mass accuracy (<1 ppm) and mass resolving powers, allowing distinct peaks to be identified.³² For example, *Kujawinski et al.* use ESI-FT-ICR MS to measure organic matters;^{36, 37} *LeClair et al.* use this technique to identify the function groups in water soluble organic matter.^{38, 39}

Gas chromatography has been recently used to separate organic aerosols in the ambient atmosphere combined with mass spectrometry based on the volatility difference of aerosols.⁴⁰ However traditional GC-MS has drawbacks that peak co-elutions often appears, and the chromatographic resolution is insufficient.⁴¹ In order to overcome these shortcomings, two dimensional GC (i.e. two GC columns) are introduced. Different stationary phases (“orthogonal” phases) are required for two columns to provide better separation effect.⁴² The primary column is responsible for a volatility separation, following by the second column for a polarity separation. Therefore aerosols having similar volatility but different polarity can be separated which greatly increase the resolution of measurement.⁴³ This method provide a novel insight to assign aerosols in the two dimensional plots based on the specific retention time during the measurement.

Liquid chromatography is often coupled with mass spectrometry to analyze ambient aerosols due to its high efficiency in separating samples. For example, *Hamilton et al.* combined LC with ion trap mass spectrometry to identify the characterization of polar compounds;⁴⁴ *Muller et al.* coupled LC with electrospray ionization Fourier transform ion cyclotron resonance mass spectrometry to study the properties of oligomeric compounds in SOA;⁴⁵ However, limitations are exist for the single LC column because of poor efficient separation. Therefore *Pol et al.* came up with a promising method using comprehensive two dimensional LC coupled with time of flight mass spectrometry to analyze ambient aerosols.⁴⁶ Two LC columns contribute to fast and more efficient separation, and provide better foundation for the following mass detection.

1.2.2 Black Carbon (BC)

Black carbon is defined as the carbonaceous material that is formed by incomplete combustion of fossil fuels and other sources, such as open burning of forest and on-road and off-road diesel engines. *Bond et al* estimated approximate 7500 Gg yr⁻¹ of global emission of black carbon in the year of 2000.⁴⁷ Because of the aggregation property, the size of BC can range from several nanometers to centimeters. The small size of BC tends to remain in the air and transport through wind events regionally or even globally, resulting in the impairment of visibility.⁴⁸ BC also plays a significant role in absorbing

the sunlight, which leads to the global warming. According to the IPCC report, the total climate forcing for BC is 1.1 W m^{-2} , which is the second most important climate forcing agent comparing with greenhouse gas CO_2 (radiative forcing is 1.56 W m^{-2}).⁴⁷ On the other hand, BC has a harmful effect on human health, causing damage of respiratory system.⁵ Therefore, monitoring the concentration of BC and developing methods to explore its effect have drawn the scientist's attention. For example, *Thompson* group combined aerosol albedometer and laser induced incandescence to measure the optical properties and the mass absorption cross section (MAC) in real time.⁴⁹ *Liu et al* postulated an increase of MAC when BC is coated with other hygroscopic material, indicating more light absorption.⁵⁰

1.2.2.1 Measurement Techniques of Black Carbon

In order to quantify the black carbon in the air, numerous techniques have been developed. The most common methods include thermo-optical measurement, light absorption measurement and laser-induced incandescence (LII).

The thermo-optical is a method that separates organic carbon (OC) and elemental carbon (EC) based on the thermo sensitivity of each carbon components in which both OC and EC are oxidized to CO_2 at temperature as high as 4000 K. Then the CO_2 is either quantified by nondispersive infrared detector, or reduced to CH_4 which is analyzed by flame ionization detector (FID).⁵¹ *Birch et al* conducted the thermo-optical experiment to determine the concentrations of OC and EC using NIOSH 5040 standard in which both temperature and atmosphere were controlled.⁵² *Cavalli et al* put forward an optimized thermo evolution protocol for EUSAAR (European Supersites for Atmospheric Aerosol Research) project to improve the accuracy of separation.⁵³

Black carbon is known as the most strongly light absorbing component of the particulate matter, thus the measuring of absorption coefficient (b_{abs}) is a valuable method to quantify BC in the atmosphere. Particle soot absorption photometer (PSAP) is a filter based instrument that monitors the light absorption in real time by recording the transmittance of filter caused by particle deposition. To date, 3 wavelengths ($\lambda=467, 530$

and 660 nm) of PSAP is developed for more diverse measurement. The calculation of the b_{abs} is given by the following equation:

$$b_{\text{abs}} = \frac{A}{V} \ln \left(\frac{I_0}{I} \right) \quad (3)$$

Where A is the sample spot area (m^2), V is the volume of air flowed into filter (m^3); I_0 is the average filter transmittance during prior time, and I is the filter transmittance of current time.⁵⁴ Although PSAP is very simple to operate, filter needs to be manually changed when the transmittance drop to 0.7, which makes the collection not so stable.

Photoacoustic spectrometer is also a commonly used instrument to measure the light absorption coefficient of black carbon. When the light absorbing components absorb the laser beam power and convert it to the acoustic pressure, this acoustic signal is detected by the microphone, and hence produces the light absorption through the acoustic resonance. *Arnott et al* reported the detection limit of b_{abs} is 0.4 Mm^{-1} for their design of photoacoustic spectrometer.⁵⁵ While *Lack et al* developed a more sensitive method to measure aerosol absorption by photoacoustic spectrometer with a detection limit as 0.08 Mm^{-1} at 532 nm wavelength.⁵⁶

Laser-induced incandescence (LII) is a very important technique that has been recently commonly used to measure the mass concentration of black carbon. It introduces a high peak power laser to rapidly heat the sample to over 3000°C . The sample then absorbs the laser energy and incandesces, producing the broad-band visible emission. The intensity of the LII signal is related to the BC mass concentration. It is a very sensitive and precise measurement in that it can measure against dark background at high laser power. *Wei et al* developed an innovative method to determine the soot mass absorption cross section in real time by combining the aerosol albedometer with LII.⁴⁹ Recently, Droplet Measurement Technologies commercialized an LII instrument named Single Particle Soot Photometer (SP2) which is powerful in detecting the BC mass concentration (as low as 10 ng/m^3) and mixing state of single particle level.⁵⁷ The continuous ND:YAG laser beam illuminates the aerosols coming from sample inlet, and heat them to produce

incandescence. Both the scattering and incandescence signal are captured by the detectors then. The schematic of SP2 is shown in Figure 1.4.⁵⁸ The SP2 has been utilized in HIPPO (Haiper pole-to-pole observations) campaign to measure soot concentration above Pacific area.⁵⁹

1.2.3 Inorganic Aerosols

Inorganic aerosols account for 25-50% of atmospheric fine aerosol mass, among which the sodium, nitrate, sulfate and ammonium are predominant.⁶⁰ Nitrate is normally formed by gas-phase oxidation of NO_x emission, and neutralized by ammonia to produce ammonium nitrate. Sulfate is formed by oxidation of SO_2 in the gas phase, while the sodium is commonly found in the ocean area and formed by sea spray. Due to the partition and transportation of inorganic aerosols, many scientists are interested in monitoring their concentrations in both lab and field.⁶¹⁻⁶³ One remarkable property of inorganic aerosol is the deliquescence, which improves the ability in absorbing water. Evidence shows that when the black carbon is internally mixed or coated with inorganic materials, such as sulfates and nitrates, it becomes more hygroscopic under wet condition, and absorbs more sunlight.^{64, 65}

More and more efforts are made to measure the inorganic aerosol in the atmosphere, including the composition and concentration. Two most popular techniques are Particle into Liquid Sampler (PILS) and Aerosol mass spectrometer (AMS).

The particle into liquid sampler (PILS) was originally designed by R.Weber's group. It involves a process in which aerosols are mixed with steam and then cooled. Aerosol particles grow into droplets as water condenses, and particles become large enough to be collected by inertial impaction.⁶⁶ Refinements to PILS have been made to improve its collection efficiency. Figure 1.5 is the schematic of refinement PILS which has better efficiency of collection. The design idea of this instrument is to mix ambient aerosols with high temperature water steam in a long tube. Then rapid cooling of steam provides supersaturation of water vapor. In this environment, aerosols grow into droplets which are large enough to be collected by an inertial impactor. There is a little cavity in

the impactor used to collect sample droplet, it's an innovative design since it can concentrate the droplets and reduce the flow rate of water which is needed to wash the sample to the analysis system.⁶⁷ In addition, this method is an automated process for real time measurement when directly coupled with ion chromatography (IC), or mass spectrometry (MS). Moreover, *Noblitt et al* measured the concentration of sulfate and nitrate with limit of detection of 70-140 ng/m³ when coupled the PILS with microchip electrophoresis.⁶⁸ *Sorooshian et al* successfully quantified the inorganic ion in the atmosphere for 2004 International Consortium for Atmospheric Research on Transport and Transformation (ICARTT) field campaign with modified PILS.⁶⁹

Aerosol Mass Spectrometer (AMS) is a very powerful technique that provides detailed information about the size distribution and composition of the ambient aerosol. The AMS consists of three main parts: aerosol inlet, particle sizing part, and composition detection chamber. Firstly, the aerosols are introduced into AMS through aerodynamic lens to form a narrow particle beam (i.e. size diameter ranging from 70 to 500 nm). Then the aerosols are transmitted into a detection chamber where they are impacted on a heated surface. Finally, the vaporized aerosols are ionized through electron impact and analyzed by mass spectrometry. During this process, the transmission of the particle beam to the detector is modulated by a mechanical chopper to obtain time of flight information.^{19, 24, 70} Nowadays, the AMS are popular in field measurement. For example, in 2008, *Huang et al* developed an Aerodyne High-Resolution Time-of-Flight Aerosol Mass Spectrometer (HR-ToF-AMS) to measure the PM composition in the atmosphere during Campaigns of Air Quality Research in Beijing, and reported the percentages of sulfate, ammonium and nitrate are 26.7%, 15.9% and 15.8%, respectively.⁷¹ *Sun et al* utilized the HR-TOF-AMS to measure the concentration of non-refractory submicron particulate matter in the Intercontinental Chemical Transport Experiment Phase B (INTEX-B) campaign, and suggested that the organics and sulfate were the dominant species, on average accounting for 55% and 30%, respectively.⁷²

1.3 Optical Properties of Atmospheric Aerosols

Light will be attenuated by particles through varieties of processes, such as refraction, reflection, and absorption, all of which cause the loss the initial energy. The net loss of the energy is called extinction and modeled by Beer- Lambert law:

$$I = I_0 e^{-(b_{ext}z)} \quad (4)$$

Where I (W/m^2) is the light intensity travelling through aerosol, I_0 (W/m^2) is the initial light intensity, b_{ext} (m^{-1}) is the extinction coefficient, and z (m) is the path length. A larger extinction coefficient with constant path length results in a lower transmittance which is described as the ratio of I and I_0 . On the other hand, the extinction coefficient is the sum of scattering coefficient (b_{scat} , m^{-1}) and absorption coefficient (b_{abs} , m^{-1}). The interplay between scatter and absorption can be described by a variable named single scatter albedo (SSA), which is in a range of 0-1. For aerosol that absorbing no light, the SSA is equal to 1, otherwise, SSA is less than 1. Equations below suggest their relationship,

$$b_{ext} = b_{scat} + b_{abs} \quad (5)$$

$$SSA = \frac{b_{scat}}{b_{ext}} \quad (6)$$

In order to better measure the optical properties of aerosol, varieties of technique were developed. The Cavity Ring-down Spectroscopy (CRDS) is a very sensitive method to determine the extinction coefficient. As shown in Figure 1.6, a short (5 ns) laser pulse is introduced into the optical resonator form by two highly reflective mirrors ($R > 0.999$) so that the light bounces between the mirrors multiple times. On each pass, a small portion of the light is lost since the mirrors are not perfect reflectors. Additionally, the light intensity will drop if the particles that absorbing or scattering light are introduced into the resonator. Therefore, the rate at which light is lost from the measurement cell can be measured and relate that to the sample extinction coefficient (b_{ext}) by monitoring the attenuated time constant (τ). The time constant (τ) is the time when the light signal decay to $1/e$ of its original value, which is explained in the equation below.⁷³

$$\tau = \frac{t_r}{2[(1 - R) + b_{exttotal}L]} \quad (7)$$

Where t_r is the round trip time of laser beam, R is the reflectivity of mirror, $b_{exttotal}$ is the total extinction coefficient, and L is the path length of the cavity cell. However, the b_{ext} can be calculated by Equation (8):

$$b_{ext} = \frac{1}{c} \left(\frac{1}{\tau_{sam}} - \frac{1}{\tau_{air}} \right) \quad (8)$$

Where c is the velocity of light in the vacuum; τ_{sam} is the time constant of sample aerosol and τ_{air} is the time constant of filtered air. Due to the long path length, CRDS can achieve impressive sensitivity, of which detection limit is lower than 1 Mm^{-1} . Thompson, *et al* reported an average extinction coefficient of 34.5 Mm^{-1} and 31.1 Mm^{-1} utilizing the laser with a wavelength of 510 nm and 578 nm, respectively in Florida.⁷⁴ Li, *et al* conducted the air monitoring in Fudan University, China, obtaining the b_{ext} as 417 Mm^{-1} at a wavelength of 532 nm.⁷⁵

In addition, lots of other methods are developed to measure the optical properties. For instance, integrating nephelometer is used to determine the scattering coefficient, and the PASP is utilized to measure the absorption coefficient of aerosol. With the development of the instruments, simultaneously measurement of b_{ext} and b_{scat} are becoming possible.⁷⁶⁻⁷⁸ Dial, *et al* performed a CRDS on aerosol within an integrating nephelometer sphere at a wavelength of 532 nm.⁷⁶ Ma, L *et al* tested the SSA of biomass burning aerosol and mineral dust as 0.83 and 0.75, respectively in the near UV region, i.e. $\lambda=355 \text{ nm}$.⁷⁸

1.4 Motivation of dissertation work

In this dissertation, I will focus on research related to secondary organic aerosols (SOA) and black carbon (BC) in earth's atmosphere. SOA appears to consist of a complex mixture of thousands of compounds, and the complete atmospheric life-cycle of this material is not currently known. Our ability to unravel this mystery and understand SOA is directly linked to development of analytical methods and straightforward

approaches to data treatment. The focus of my dissertation work will be to develop analytical methods influenced by engineered frameworks to describe SOA and understand its chemical evolution in the atmosphere. In one effort, we created a 3-dimensional coordinate system to distribute SOA within. High resolution mass spectrometry was used to populate the 3D space with organic material from aerosols based on molecular weight, heteroatom mass, and double bond equivalents. This 3D approach works as air quality model, and both the physical property and chemical reactivity can be obtained for each compound.

Black carbon is the most light absorbing component of particulate matter, which absorbs sunlight and leads to global warming. Evidences also show the black carbon can be quickly internally mixed with other non-absorbing materials in the atmosphere, causing the change of the absorption property. Therefore quantifying the absorption property of black carbon is crucial to the climate knowledge. In this dissertation, we developed an analytical method in which aerosol albedometer was coupled with laser-induced incandescence (LII) to measure the mass absorption cross section M.A.C. (i.e. absorption efficiency) of black carbon in real time. In addition, both optical properties and M.A.C. value of coated soot sample, fresh soot and ambient aerosols were compared in order to illustrate the differences of absorption efficiency. On the other hand, water vapor is abundant in the environment, and the water uptake in the coated black carbon will also leads to the enhancement of light absorption, which is corresponding to the core-shell type lensing. To study this effect, both the lab and field measurements were conducted varied by relative humidity and coating fraction.

Table 1.1 Natural and anthropogenic emission of atmospheric aerosol (Reproduced from data report of I.P.C.C)

Source	Amount Emitted (Tg/yr)	Best Estimate (Tg/yr)
Natural		
Soil dust	1000-3000	1500
Sea salt	1000-10000	1300
Botanical debris	26-80	50
Volcanic dust	4-10000	30
Forest fires	3-150	20
Gas to particle conversion	100-260	180
Photochemical	40-200	60
<i>Total for natural source</i>	2200-24000	3100
Anthropogenic		
Direct emissions	50-160	120
Gas to particle conversion	260-460	330
Photochemical	5-25	10
<i>Total for anthropogenic source</i>	320-640	460

Radiative forcing of climate between 1750 and 2005

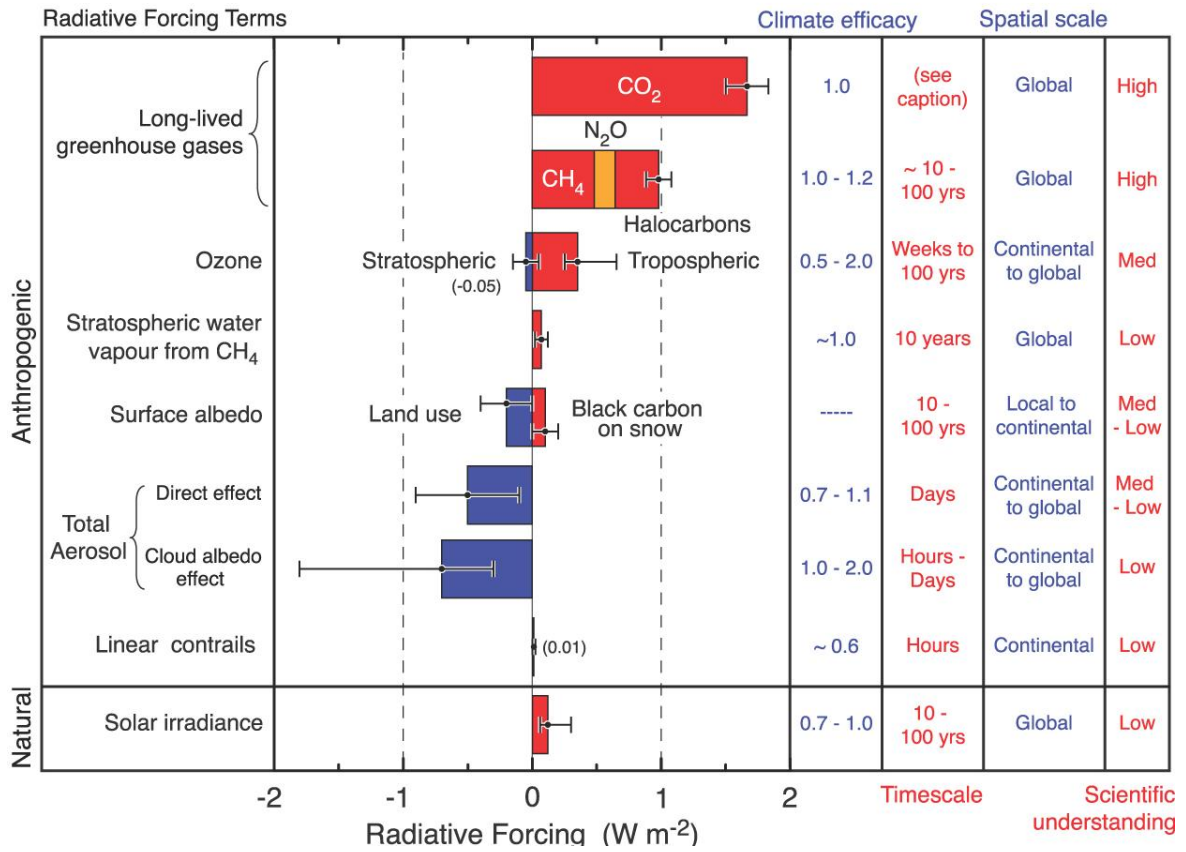


Figure 1.1 Global radiative forcing of climate between 1750 and 2005. This figure is adapted from IPCC report, 2007.³

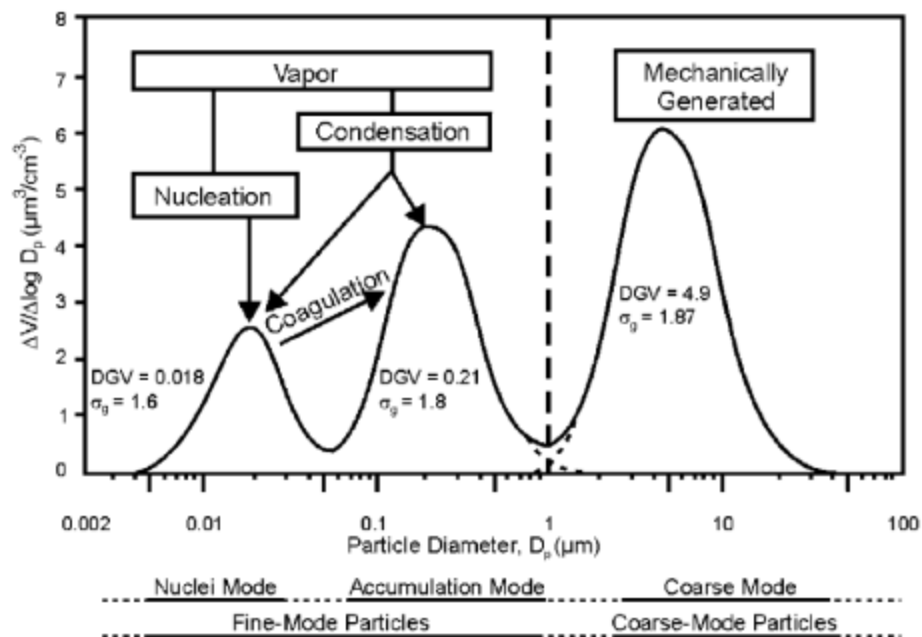


Figure 1.2 Size distribution of a typical atmospheric aerosol. DGV means volume median diameter; σ_g means geometric standard deviation (Reproduced from Wilson, W.E., Chow, J.C., Claiborn, C., Fusheng, W., Engelbrecht, J., and Watson, J.G., "Monitoring of Particulate Matter Outdoors", *Chemosphere*, 49 (2002), 1009-1043 with permission of publisher)⁷⁹

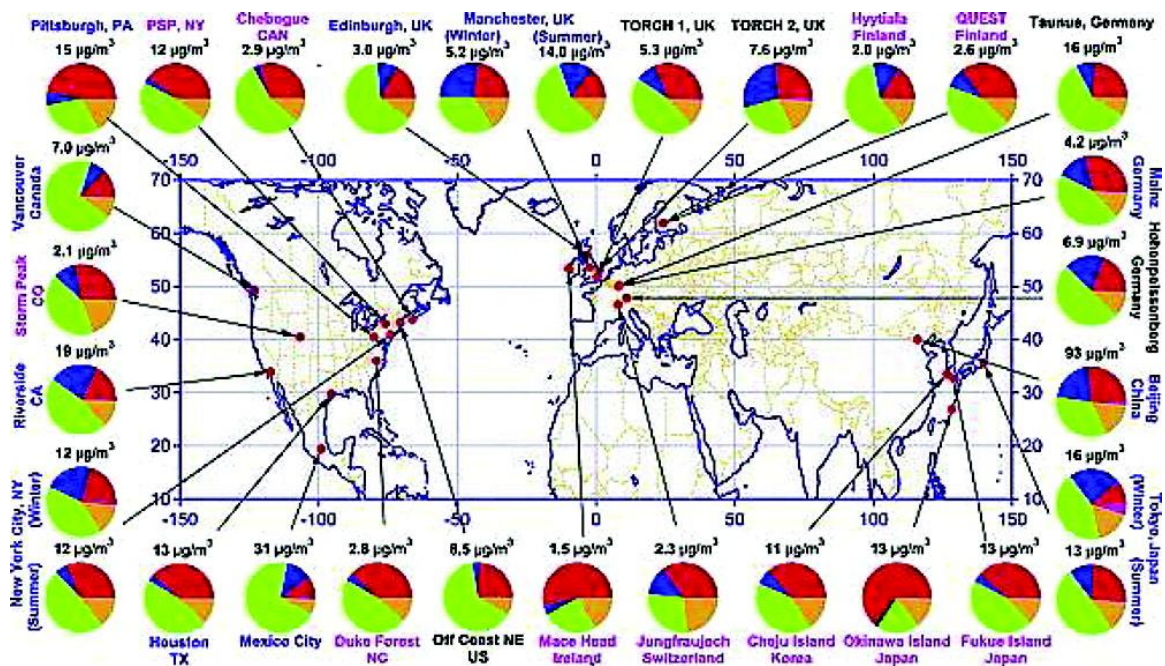


Figure 1.3 Pie charts show the average composition and mass concentration in different site of the world: organic (green), sulfate (red), nitrate (blue), ammonium (orange), and chloride (purple). This figure is reprinted with permission of Lee, S.H., and Allen, H.C., "Analytical Measurements of Atmospheric Urban Aerosol", *Anal Chem*, 84 (2012), 1196-1201¹

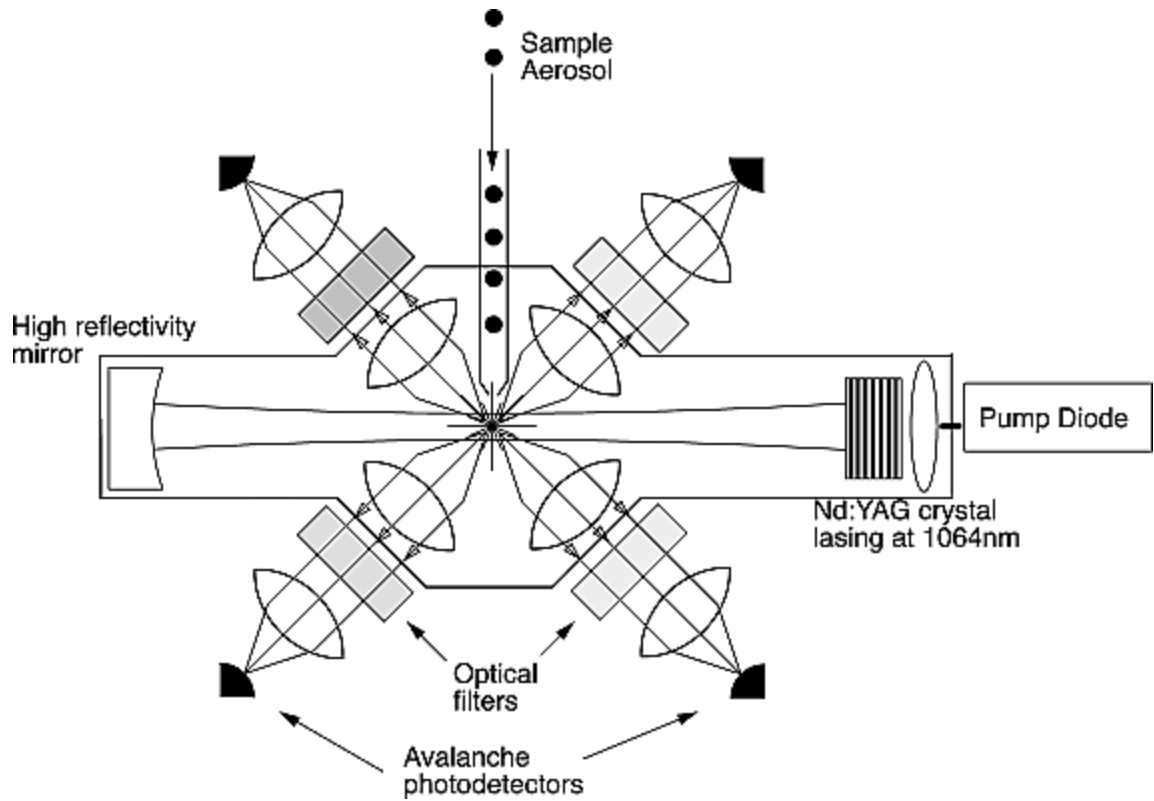


Figure 1.4 Schematic of Single Particle Soot Photometer (SP2). (Obtained copyright clearance from Schwarz, J. P.; Gao, R. S.; Fahey, D. W.; Thomson, D. S.; Watts, L. A.; Wilson, J. C.; Reeves, J. M.; Darbeheshti, M.; Baumgardner, D. G.; Kok, G. L.; Chung, S. H.; Schulz, M.; Hendricks, J.; Lauer, A.; Karcher, B.; Slowik, J. G.; Rosenlof, K. H.; Thompson, T. L.; Langford, A. O.; Loewenstein, M.; Aikin, K. C., Journal of Geophysical Research-Atmospheres 2006, 111 (D16).)⁵⁸

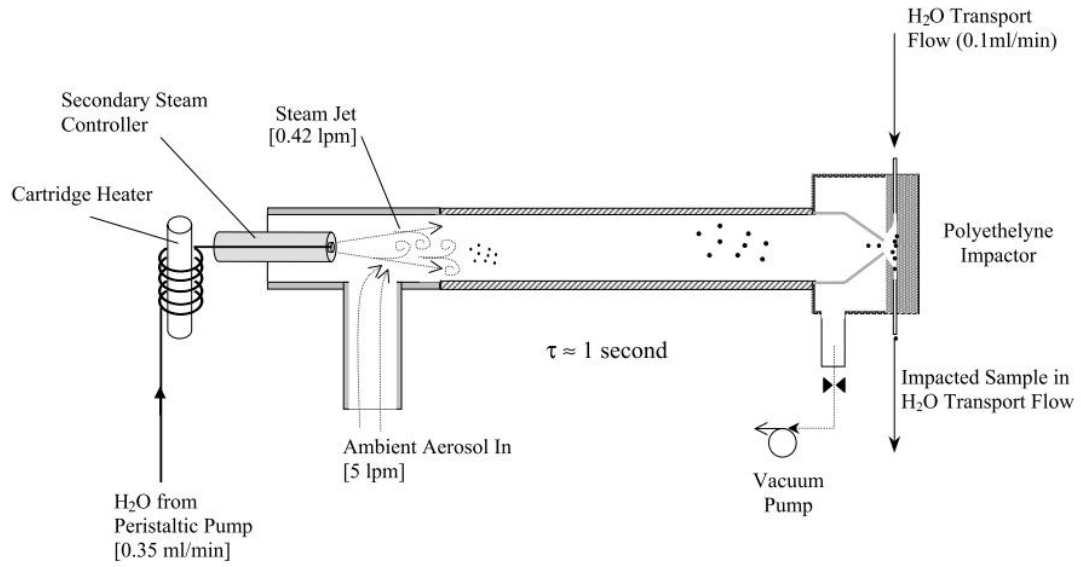


Figure 1.5 Schematic of refinement PILS. This figure is reprinted with the permission of Orsini, D. A.; Ma, Y. L.; Sullivan, A.; Sierau, B.; Baumann, K.; Weber, R. J., *Atmospheric Environment* 2003, 37 (9-10), 1243-1259⁶⁷

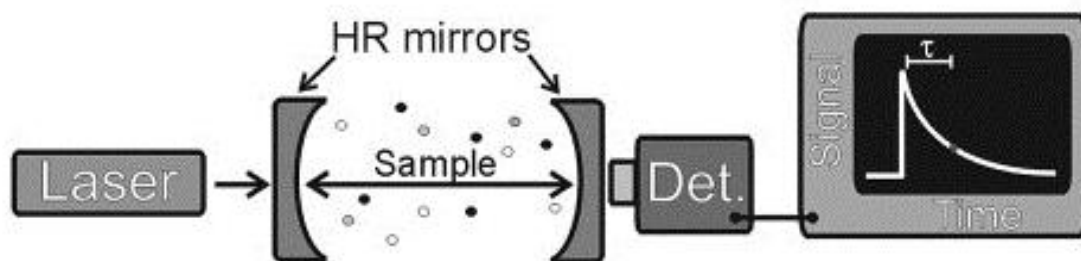


Figure 1.6 Schematic of Cavity Ring-down Spectroscopy (CRDS). (Reproduced from Redmond, H. E.; Dial, K. D.; Thompson, J. E., *Aeolian Research* 2010, 2 (1), 5-26.)⁷³

CHAPTER II

THE CHEMICAL EVOLUTION & PHYSICAL PROPERTIES OF ORGANIC AEROSOL: A MOLECULAR STRUCTURE BASED APPROACH

Atmospheric Environment **2012**, 62, 199-207

2.1 Introduction

Molecular structure is important to quantitatively describe polarity, volatility, hygroscopicity, and chemical reactivity of materials dispersed in earth's atmosphere. Recent models of atmospheric secondary organic aerosol (SOA) classify matter in two dimensional (2-D) space based on parameters such as volatility, number of carbon atoms in a molecule, mean carbon oxidation state, and/or atomic ratios of O:C or H:C.^{14, 80-82} These engineered approaches develop a cognitively pleasing framework within which the complexity of the organic aerosol can be treated tractably and often provides clues of chemical functionalization of the aerosol. In addition, key physical properties of the compounds that govern phase partitioning (e.g. volatility) may be estimated by a substances location in the 2D space, and the chemical state of the organic aerosol can be tracked empirically through a variety of techniques, including aerosol mass spectrometry (AMS).^{83, 84} However, any coordinate point in the 2D space corresponds to many, many types of molecules – both structural isomers and even different compounds. The models rely on the supposition that averaging the chemical and physical properties of all molecules within an address bin yields a result that is meaningful to describe atmospheric processing and phase partitioning. When the number of carbon atom in a molecule is ≥ 6 -7 a significant number of structural isomers are possible for any given molecular formula (>100 isomers). This number increases rapidly to $\approx 10^{10}$ isomers for 15-20 C atoms, and it may be tempting to assume an average taken over a large number of isomers is appropriate. However, since molecular structure is important to quantitatively describe polarity, volatility, hygroscopicity, and both rates and mechanistic routes for chemical reaction it is not clear averaging across many compounds yields meaningful insights. In fact, averaging fundamentally dissimilar items improves neither the precision nor accuracy of a data set (e.g. apples vs. oranges comparison). At present, the 2D

approaches are generally limited to considering only 3 elements in the organic aerosol: carbon, hydrogen, and oxygen. This is not optimal since recent measurements suggest organosulfates and nitrogen containing organics are present in atmospheric aerosol.⁸⁵⁻⁹⁴

Use of molecular descriptors that are simple to use but provide more complete characterization of the physical behavior and reactivity of organic aerosol would offer an advance. Traditionally, researchers have been limited by the lack of analytical techniques able to provide such molecularly speciated data on substances present at $\ll 1 \mu\text{g m}^{-3}$ concentration in ambient air. However, in recent years multiple investigators have employed high-resolution mass spectrometry (HR-MS) with soft ionization techniques (ESI, DESI, MALDI etc...) for measurements on atmospheric aerosols.⁹⁵⁻⁹⁸ Ionization through these methods produces intact molecular ions (minimal source fragmentation), and high-resolution mass analyzers can provide up to 25 billion theoretical plates of separation.⁹⁹ This performance is >3 orders-of-magnitude larger than what even the most advanced gas or liquid separation-based techniques can offer in terms of separation efficiency. HR-MS also offers rapid and definitive molecular mass determination with limits of detection often in the low femtomole (10^{-15} mol) range without the need for chemical derivatization or extensive sample pre-treatment.

In this report, we introduce an alternate classification scheme for organic aerosol that is easy to understand and simple to use. The approach is based on a 3-dimensional coordinate system in which organic molecules are arranged based on molecular weight, heteroatom mass (O, N, S, Cl etc...) and double bond equivalents (DBE). The approach is similar to the previous 2D approaches in that heteroatom mass can be linked to either O:C ratio or carbon oxidation state. Similarly, molecular weight is directly proportional to volatility. However, we argue heteroatom mass is a more descriptive parameter while simultaneously being much more inclusive (can consider inclusion of N, S, Cl etc... in the aerosol). Addition of a third dimension (DBE) allows the possibility for improved description of chemical reactivity of the material through ozonolysis or hydroxyl (OH) addition. After defining the coordinate system, we then couple it to measurements made through high-resolution mass spectrometry. For this work, we analyze both lab generated

aerosol (SOA from squalene ozonolysis), and ambient aerosol collected with a high-volume air sampler at our site. To provide a more complete analysis, mass spectral data for both chamber and ambient aerosol reported by other investigators in previous literature is also considered. By using a QSPR for a large number of organic compounds, we illustrate trends in volatility and water solubility as a function of location within the 3D space.

2.2 Methods

2.2.1 The 3D Coordinate System

Figure 2.1 introduces the 3D coordinate system, and locates several well-known aerosol types and tracer compounds within the space. Figure 2.1 also lists (open circles) locations of the top 10 ozone promoting VOCs for the Pearl River Delta of China (isoprene, xylene, toluene, ethylene, propene, 1,2,4-trimethylbenzene, 2-methyl-2-butene, 1-butene, α -pinene).¹⁰⁰ These compounds can be considered possible precursors to SOA. Organic matter is distributed throughout a wedge-shaped region that is constrained by the heteroatom mass = molecular weight plane. Here, heteroatoms are considered to be any element other than carbon and hydrogen. All three dimensional parameters used to classify aerosol can easily and quickly be derived from a molecular formula. In turn, molecular formula for organics in the aerosol can be empirically determined through high resolution molecular mass spectrometry (HR-MS). The region very near the heteroatom mass = molecular weight plane is not well-populated with organic compounds as it is chemically impractical (requires formulas inconsistent with laws of chemical bonding such as C_2O_{15} etc...). For materials in organic aerosol, it would be very rare for heteroatom mass to exceed 65% of molecular weight.

2.2.2 Test Compound Database & QSPR Modeling

The database of test compounds used for QSPR analysis was downloaded from the National Cancer Institute (NCI) open database at <http://cactus.nci.nih.gov/download/nci/>. The “August 2000 SMILES” file was truncated to compounds containing only C, H, O, S, and N. This yielded 31,066 unique compounds

and corresponding SMILES codes. The SMILES strings were imported into the U.S. Environmental Protection Agencies EPI Suite Software for Microsoft® Windows, v 4.10 to return estimates of vapor pressure, Henry's constants, and reaction rate constants when available. Reaction rate constants were predicted with the AOP-WIN module within EPI suite that is described in Meylan and Howard (1993).¹⁰¹ HENRYWIN¹⁰² was used for Henry's law constant prediction, and MPBPVP used for estimation of volatility. In 2007, the EPI Suite was reviewed by a panel of independent scientists to assess predictive ability and a report of findings is available at <http://www.epa.gov/sab/pdf/sab-07-011.pdf>. In general, it was found that each QSPR module has its own inherent limitations, but overall the modules were rooted in sound science and generally useful for demonstrating trends for regulatory use. To demonstrate the spirit of the panel's findings, when the OH reaction rate constants were predicted for 647 test compounds, over 95% of results were within a factor of three of experimental values. In many cases, a factor of three may be useful to demonstrate trends in data or for model building. Here, we use values returned by EPI Suite, but for increased accuracy we encourage use of actual measurements whenever they are available. Greater than 31,000 compounds have been used for the k_{OH} , vapor pressure, and Henry's law analysis. However, k_{O_3} values could be predicted for only 4681 compounds. The vapor pressure data is reported in mm Hg, and Henry's law data in units of atm m³ per mole. The negative logarithm of the predicted values have been plotted in Figure 2.3 to better account for the very large range of the datasets.

2.2.3 Squalene Ozonolysis Experiment

The experiment was conducted inside of a 3.6 m³ chamber lined with FEP. Briefly, 15 μ L of squalene (>99%, ACROS) was added to a clean flask and allowed to evaporate into an air stream that perfused the flask. This air stream was then passed into the experimental chamber. The zero air perfusing the flask and the chamber was filtered sequentially with an activated carbon and HEPA filter prior to use. No seed particles were used for experiment. Ozone was generated from zero air using a photolytic ozone generator and then added to the chamber. Both ozone and NO_x concentration were continually monitored in the chamber (2B Technologies ozone sensor and Horiba APNA-

370 for NO_x). Particle mass concentration was monitored with a Mie RAM-1 real time aerosol monitor, and rough size distribution information obtained via a MetOne GT-526 particle monitor. The NO₂ concentration initially increased to approx. 15 ppbv at the onset of the experiment, but NO was generally < 1.5 ppbv. After the initial rise, total NO_x then fell exponentially to < 2 ppbv for the remainder of the experiment. Aerosol sample was collected onto membrane filters (Pall E70-2075W) at a sample flow rate of 2.5 LPM. The filters were washed before sampling with HPLC grade 50:50 water/acetonitrile (ACN). The experiment continued from roughly 0 to 1300 squalene ozonolysis lifetimes, and multiple samples were collected during the experiment in an attempt to demonstrate chemical aging of the aerosol. After analysis it was determined all samples were chemically very similar. Results presented in this work describe the aerosol sample collected between 50 and 1100 squalene ozonolysis lifetimes. After collection of sample, the filter was transferred to a small vial and immersed in 100 μL of 50:50 water/ ACN with 0.05% formic acid. Samples were stored in a refrigerator until analysis. A filter blank (no sampling period) was also treated via this process, and any peaks observed in the mass spectrum for the filter blank have been discarded from our analysis. Prior to analysis, the liquid extract was centrifuged at 14,700 RPM for 80 min to remove insoluble material. Approximately 20 μL of the supernatant was used for analysis via HR-ESI-MS on the Orbitrap mass spectrometer.

2.2.4 Ambient Aerosol Sampling

Quartz filters (8" × 10") for blank measurement and sample (Whatman, 18209932) were pre-fired at 210°C overnight to remove volatile vapors. Aerosol was collected onto the filters using a mass flow controlled TSP high-volume sampler (TE-5170-D, Tisch Environmental) from 2:00 P.M local time on January 13 2012 to 10:00 A.M on January 16 2012. Flow was not actively monitored during the experiment, but the sampler product specifications constrain sampling flow to 39-60 CFM. Filters were weighed before and after sampling allowing estimation of total aerosol mass of approx. 16 μg m⁻³ over the sampling period. After sampling, 1 cm squares of both the active filter and blank were placed into vials and extracted with 100 μL of 50:50 water/ACN with 0.1%

formic acid. Samples were stored in a refrigerator until analysis. For analysis, samples were diluted with an additional 70 μL of solvent and then centrifuged at 14,700 RPM for 40 min. Approximately 20 μL of the supernatant was used for analysis via HR-ESI-MS on the Orbitrap instrument in positive-ion mode.

2.2.5 High-resolution Mass Analysis

The samples were analyzed via the Orbitrap mass spectrometer (LTQ Orbitrap Velos, Thermo Scientific) with an ESI source. The solution was directly infused at 2 $\mu\text{L min}^{-1}$ flow into the ESI interface with a 30 μm i.d. SilicaTipTM (PicoTip[®] Emitters). The needle voltage was set +1.8 KV. The mass resolving power was 30,000 and mass accuracy <5 ppm. The instrument was calibrated in positive-ion mode. Positive-ion mass spectra were collected using full scan analysis ($100 < m/z < 1000$). Here we consider only $[\text{M} + \text{H}^+]$ ions.

2.2.6 Assigning Molecular Formulas

After analysis, the text files containing peak heights and m/z values was imported into the *Molecular Formula Finder* software developed by the National High Magnetic Field Laboratory available for download at <http://magnet.fsu.edu/~midas/download.html>. For the squalene analysis, only the most abundant isotopes of C, H, and O were considered and a mass accuracy window of 15 ppm was employed in the formula search. Molecular formulas returned were used to generate the 3D plots presented in the manuscript. For the ambient aerosol sample, only the most abundant isotopes of C, H, O, N, S were considered. A mass accuracy window of 2 ppm was used in the formula search for this analysis. It should be noted that the peak height observed and reported may not accurately describe the concentration of each component owing to differences in ionization efficiencies and recovery. Also, many peaks observed in the mass spectrum could not be assigned by this approach. After molecular formulas have been assigned, the calculation of molecular weight and heteroatom mass (all elements except C, H) is straightforward. Computing double bond equivalents (DBE) was accomplished through:

$$DBE = 1 + C - \left(\frac{H}{2}\right) + \left(\frac{N}{2}\right) \quad (9)$$

Where the element symbols correspond to the number of atoms of each element in the molecular formula. The presence of S or O does not affect DBE.

2.3 Results and discussion

2.3.1 Advantages of The Approach

Perhaps the most substantial advantage of the 3D graphical framework presented is it can easily account for any chemical element present in the aerosol. This is necessary given the recent evidence that nitrogen containing compounds and sulfate esters are present in organic aerosol in the atmosphere and may be responsible for a non-negligible fraction of organic aerosol mass. The graphical approach is flexible and can be coupled to reactions occurring in gas, particle, or liquid phases. Since the 3D approach described here maintains a molecular basis, it can also easily be coupled directly to chemically speciated VOC emissions inventories. Another key advantage is the ease with which trends in data can be analyzed. For instance, a homologous series of alcohols, acids, amines or ethers (e.g. alkyl chain increase or decrease) can be found by simply locating the proper heteroatom mass, and DBE planes, and searching for repeating $-\text{CH}_2-$ units separated by 14.01565 mass units in the molecular weight dimension. Also, chemical change can be linked to quantized mass changes and alteration in DBE which leads to specific reaction trajectories in the 3D space for any/all mechanisms of reaction. For instance, hydrogenation/dehydrogenation reactions do not involve a change in heteroatom mass and therefore occur within a fixed plane of constant heteroatom mass. These reactions do involve loss or gain of 2 H atoms and one DBE so occur along a slope of approx.-2 a.m.u. per D.B.E. within any given heteroatom mass plane. Addition of CH_2O groups yields no change in D.B.E. from the original molecule, but shifts the heteroatom mass by 15.9949146 for ^{16}O and the overall mass by 30.0105646 amu. The specific mass changes associated with chemical modifications (regardless of what they are) define the angular trajectory in the 3D space. The slope of the trajectories can easily be predicted

intuitively based upon expected change in heteroatom mass, DBE, and total molecular mass.

To demonstrate further, Figure 2.2 illustrates the mechanistic route of a possible reaction sequence proposed by Perri et al.¹⁰³ for organosulfate formation from glycoaldehyde (in yellow). Figure 2.2 also includes several compounds proposed to occur along the methylglyoxal self-oligomerization pathway (green points),^{104, 105} and a route which produces nitrogen containing oligomers from glyoxal via aqueous phase chemistry (brown points).¹⁰⁶ Considering the figure we can see oligomerization for the N containing oligomers (brown points) proceeds via $\Delta\text{DBE} = 1$, a change in heteroatom mass equal to N+O, and a change in molecular weight corresponding to the $-\text{C}_3\text{H}_5\text{NO}$ monomeric unit. Alternatively, the oligomerization of a lignin like compound reported by Chang and Thompson (2010)¹⁰⁷ and observed in cloud water¹⁰⁸ (gray points) proceed via $\Delta\text{DBE} = 4$, a heteroatom mass change consistent with addition of 2 O atoms, and a molecular weight change consistent with a guaiacolic base unit. Fragmentation and /or functionalization reactions can also easily be tracked. Figure 2.2 includes such reactions for toluene reported in previous literature (see black points).¹⁰⁹ Therefore, any and all reaction types for aerosol components, whether functionalization, oligomerization, or fragmentation can easily be considered. Another interesting demonstration of the unique utility of the approach can be found by following the trace from point A (toluene) in Figure 2.2. Initial fragmentation reactions can produce methylglyoxal, and subsequently methylglyoxal can undergo oligomerization reactions in the aqueous phase. The molecularity of the materials must be maintained to adequately describe the fragmentation reaction into the methylglyoxal coordinate, and reactions out of this coordinate depend on specific functional groups present in the molecule. Simple ratios of O: C or information about volatility would be insufficient to capture the potential for the oligomerization chemistry to occur.

2.3.2 Prediction of Physical & Chemical Properties

A substance's location in the 3D space might yield insights into its physical behavior and phase partitioning in the atmosphere. Two important variables in this

regards include vapor pressure and Henry's law constant. Vapor pressure describes gas-aerosol phase partitioning,¹¹⁰⁻¹¹² while Henry's law constants describe the tendency of materials to partition into aqueous phases (e.g. cloud water or fogs).^{113, 114} To examine whether a compound's location correlates with physical properties we present Figure 2.3A and B. These figures illustrate trends in vapor pressure and Henry's law constant for compounds' location in the 3D coordinate system. Each of the $\approx 31,000$ data points in the figures represents an individual organic compound. Vapor pressures and Henry's law constants for each compound have been estimated using the U.S. Environmental Protection Agency's EPI Suite Software (US EPA, 2012). The trends of Figure 2.3A and B are easily identifiable. Highly volatile compounds tend to occupy the space near the origin. In addition, aqueous solubility increases with chemical functionalization (increase in heteroatom mass) as the molecules tend to become more polar. Such information is very useful to track or model phase partitioning of organic components in the atmosphere. The correlation between location in the 3D space and vapor pressure has allowed us to develop a multi-linear least squares parameterization based on molecular weight, heteroatom mass and DBE.

QSPR predictions (EPA Software) of vapor pressure for the compounds in the test data set were broken up into several groups based on elemental composition of the parent compound. The data sets were compounds containing: only CH, only CHO, only CHS, only CHSO, only CHN, and only CHNO. For each group, multi-linear least squares analysis was performed using M.W., heteroatom mass, and D.B.E. as input parameters (x-variables) and the log of the QSPR predicted vapor pressure as the y- (dependent) variable. This analysis was completed in Microsoft Excel using the regression plug-in, according to a formula of the form:

$$y = m_{M.W.} \times (M.W.) + m_{Heteromass} \times (Hetero Mass) + m_{D.B.E.} \times (D.B.E.) + b \quad (10)$$

The analysis yields the eqn. of a best fit line with a slope corresponding to each variable (m terms) and an intercept (b). The resulting eqns. can then be used to predict vapor

pressure based on elemental composition. The best-fit parameters obtained in this analysis are presented in Appendix A.

2.3.3 Prediction of Chemical Reactivity

A complete model for organic aerosols must also describe atmospheric chemical processing. For any point in the 3D space, knowledge of reaction rates both into and out of a coordinate is required to treat the chemical evolution of material in time. This is a complex task since an organic compound may exist in either gas, aqueous, or particle phase. Another potential advantage of the molecular-based approach advocated here is the ability to utilize databases of experimental reaction rate constants¹¹⁵⁻¹¹⁸ or use quantitative structure property relationships (QSPR) for estimating VOC reaction rate constants with oxidants for both the gas or aqueous phase.¹¹⁹⁻¹²⁸ Addition of the DBE descriptor in this 3D framework effectively accounts for the possibility of addition of OH to π -bonds or ozonolysis. This could allow modeling reaction rates for materials assigned to particular coordinate addresses.

When QSPR predicted rate constants for gas-phase proton abstraction via OH (k_{OH}) and ozonolysis rate constant (k_{O_3}) are plotted for 31,020 and 4680 test compounds in the 3D space, no simple trend in the data is observed. This makes developing a simple and accurate parameterization based solely on M.W., heteroatom mass, and DBE challenging. As observed in Figure 2.4, the predicted k_{OH} and k_{O_3} values often decrease by 1-3 orders of magnitude for highly functionalized organics indicating a slower reactive removal process (on average) as heteroatom mass increases. However, data points of vastly different kinetic constants (color) from surrounding data points do appear in the plot. These compounds contain chemical functionalities that make them react at different rates from adjacent compounds. These “outliers” make it difficult to model kinetics using only the three quantitative descriptors we employ.

2.3.4 Comparison of 3D Approach to Alternate Schemes

To a large extent, all classification schemes for organic aerosol are attempts at dimensionality reduction. The various schemes attempt to describe a complex physical

reality by as few variables as possible. We liken this to a tax assessor levying property tax on homes by using an address. The tax collector does not tour each home to assess its value, but can use an address to determine approximate worth by past record of sales etc... Knowledge of only the town the home is present in, or even the zipcode may be insufficient to accurately determine worth due to heterogeneity of property values. However, a variable of sufficient resolution (in this example the property's address) can be used to simplify the situation and accurately describe a properties worth regardless of the specific amenities of the location. As previously mentioned, descriptors such as mean C oxidation state, #C atoms, O: C ratio and saturation vapor pressure have been used as descriptors in alternate classification schemes. In the 3D approach discussed here, we use molecular weight, heteroatom mass, and double bond equivalents. We justify this approach as an improvement by virtue of the comparison of the 3D approach with alternate classification schemes made in Table 2.1. The top three groups of data are compounds which would be located at identical coordinates of mean carbon oxidation state and #C atoms.⁸⁰ The range of values for vapor pressure, k_{OH} , and Henry's law constant can differ by several orders of magnitude, despite these compounds being located at identical coordinates. This results from lack of chemical speciation. For instance, a double bond equivalent can be substituted for an O atom in a molecule yielding identical oxidation states (see pentene and pentanol). Sulfur can substitute for oxygen, etc... The bottom group of data represents compounds that would be grouped together in a classification system that employs vapor pressure and O: C ratio.^{14, 82} None of these compounds have O atoms, but all have vapor pressure between 1 and 10 mmHg. This scheme forces the vapor pressure of grouped compounds to be similar through design, but we can again see that k_{OH} and Henry's constants can differ by several orders of magnitude for an identical bin/coordinate. Furthermore, this system has no mechanism for explicitly treating inclusion of heteroatoms other than O. So substances that can be protonated in aqueous solution (such as amines) cannot be adequately treated. Also, oligomerization of small molecules such as glyoxal cannot be treated easily. This has significant implications for vapor/particle partitioning since reactions such as these in an aqueous phase will change volatility by many orders of magnitude. The 3D coordinate

system described within can resolve every compound listed in Table 2.1 without overlap. Since it is chemical in nature, effects like protonation (or other reactions) can be considered. However, the 3D approach cannot resolve structural isomers and this remains a significant limitation. In general, using O:C ratio with saturation vapor pressure is an excellent way to track VOC oxidation and reversible phase partitioning. However, the approach cannot consider all compounds (only CHO) and is not intimately linked to chemistry or molecular structure. In turn, this creates difficulty in modeling how molecular processes impact the distribution of organic material in the 2D space. Using average oxidation state and #C atoms offers an improvement as it is more inclusive of additional chemical elements. However, multiple functional group arrangements can lead to identical mean oxidation states. This can confound tracking the movement of materials throughout the space, since molecules assigned to a bin may react or behave very differently. By providing a higher resolution coordinate system, prediction of chemical and physical properties can be improved.

2.3.5 Properties of Chamber & Ambient Organic Aerosol

A significant remaining question to address is where does typical organic aerosol tend to lie within the 3D space? Here, we address this question by combining new experimental results with others previously published in the literature. First, we describe the secondary products of isoprene¹²⁹ and limonene¹³⁰ ozonolysis as previously reported in the literature by Nizkorodov's group, and a squalene ozonolysis experiment conducted in our laboratory. All data has been collected using HR-ESI-MS. A compilation of this chamber data is presented in Figure 2.5. Interestingly, the lab generated secondary aerosol generally occupies the same region in the 3D space, regardless of whether it was generated from a small VOC such as isoprene (C₅H₈) or a long-chain polyunsaturated hydrocarbon such as squalene (C₃₀H₅₀). This region is bounded by < 10 D.B.E., < 1000 M.W. and < 400 heteroatom mass. Only limonene SOA has significant quantity of compounds with M.W. > 600, but the most intense peak in the mass spectrum occurred below m/z = 200. In addition, and approximate 1:2.5 mass ratio between heteroatom mass and total mass is noted. This corresponds to roughly a 0.5-0.6 mole ratio of O:C.

In addition to the chamber experiments, we also have explored the location of ambient aerosols within the 3D coordinate system. Figure 2.6 illustrates the results of this analysis for a biomass burning plume (blue),³⁵ a sample of fog from Fresno, CA (red),⁹⁷ a rainwater sample from New Jersey (green),⁹⁸ and a sample obtained at our location in Lubbock, TX (black). Some differences between the ambient samples were observed. This is particularly true of the biomass burning plume (blue points) which appears to be less functionalized than the other samples considered. Alternatively, the rainwater sample featured many peaks well above the 1:2.5 mass ratio line previously described. This suggests a substantial degree of functionalization of the organics in rainwater. In general, ambient organic aerosol occupies the region < 10 D.B.E., < 500 M.W. and < 200 heteroatom mass. This is a similar region to that occupied by the products of isoprene and squalene ozonolysis. However, while the 1:2.5 mass ratio (and corresponding 0.5-0.6 O:C mole ratio) line does seem to split the ambient data, the scatter of individual points is clearly more significant. Nonetheless, the ambient and the chamber aerosol bulk properties appear to be somewhat similar as both seem to occupy common regions of the 3D space.

Element filters can also be applied to the data to track the locations of different chemical elements in the 3D space. The top left side of Figure 2.6 illustrates such plots. In these plots only compounds containing O and S are plotted. Such a treatment of the data may aid in source apportionment efforts or provide clues of chemical aerosol processing. In addition, since ESI-MS preserves molecular information, the presence of mass spectral peaks for specific chemical tracers such as levoglucosan, hentriacontane, or cholesterol can indicate influence of specific aerosol primary sources such as biomass burning or cooking.

The bottom left portion of Figure 2.6 illustrates how the molecular-based graphical approach is potentially useful for tracking reactions in the atmosphere. For any substance located as a point in the 3D space, an analyst can quickly assess whether a particular reaction pathway from/to that substance is viable based on observed data. To demonstrate, we have randomly chosen a point corresponding to $C_{12}H_{22}O_4$ (DBE = 2).

From this starting point, we compute the expected coordinates for hydrogenation/dehydrogenation reactions (black), addition or loss of CH₂O and H₂O fragments (gray and blue, respectively), and an esterification sequence (C₃H₄O₂) as previously described by Mazzoleni et al.⁹⁷ Interestingly, for the combination of this starting point and available observational data the compounds predicted are present at all projected coordinates. The process of predicting products requires initial assumptions about what atoms will be added or lost via the reactions and we do wish to point out that there is no assurance that the specific reaction sequence proposed (hydrogenation, CH₂O addition etc...) must have occurred to produce a “hit” at the correct coordinate in space. The presence of match with the same formula could result from simple coincidence.

2.3.6 General Trends: Similarity between Aerosol Types

While the exact chemical of the ambient and chamber aerosol is clearly not identical, the general coincidence between locations of the laboratory generated and ambient aerosols should not be considered accidental. We argue several reasons for this phenomenon. First, there are strong chemical biases against observing aerosol materials near the heteroatom = 0 plane. Many substances occupying space near the heteroatom mass = 0 plane will simply be too volatile to partition readily into the particle phase. In addition, the results presented in Figure 2.4 predict many VOC's near the heteroatom mass = 0 plane will be functionalized or fragmented via chemical reaction within minutes – hours in the atmosphere when [O₃] ≈ 40 ppbv, and [OH] ≈ 2 × 10⁶ molecules cm⁻³. Taken together, the vapor pressure effect and rapid reaction out of the coordinates biases against observing aerosol organic material very near the heteroatom mass = 0 plane. Instead, unfunctionalized VOCs rapidly react and move toward higher heteroatom masses. As this occurs, the reaction products become more stable (somewhat slower gas-phase reaction with OH and O₃) and less volatile. These materials are more likely to be associated with condensed-phase aerosol particles. As previously mentioned, recent results have suggested viscous or solid aerosol phases may inhibit the rate of functionalization, fragmentation, or mineralization reaction leading to additional chemical stability.^{18, 112, 131} Heteroatom mass clearly cannot exceed MW. Therefore, a

plane of exclusion located at heteroatom mass = molecular weight formally constrains the rear of the 3D space. However, the space very near the plane of exclusion features substances that are simply not chemically realistic based on the fundamentals of chemical bonding (e.g. CHO_{12} is not a realistic formula for a stable organic molecule). Based on the rainwater sample of Figure 2.6 and C:O atom ratios presented in the literature, it appears heteroatom mass rarely exceeds 70-80% of total molecular weight for organics in the atmospheric aerosol. This represents a practical limit for the rear of the allowed 3D space.

The space available at both higher M.W. and higher heteroatom mass does not appear to be populated with organic matter to a large degree. This is likely a consequence of two phenomena. First, a significant fraction of both anthropogenic and biogenic primary VOC emission have molecular weights $< 200 \text{ g mol}^{-1}$.¹³² Significant functionalization or oligomerization of this material would need to occur to reach molecular weights $> 500\text{-}600 \text{ g mol}^{-1}$, and it appears as if these reactions do not occur to sufficient extent in the organic aerosols considered here. Second, recent manuscripts considering laboratory aerosols have suggested that fragmentation reactions may dominated aerosol chemical aging at higher O:C atom ratios.^{133, 134} These results have special significance since this tendency provides a constraint on the degree of functionalization chemically allowed. Higher O:C ratio compounds would tend to fragment into the general region of the 3D space we observe its presence within. Taken together, these results suggest organic aerosol exists in the space between the previously stated limits of M.W., heteroatom mass, and DBE as it is a suitable marriage of sufficient molecular lifetime and low volatility.

2.3.7 Current Limitations & Future Directions

There are several improvements to the analytical method that should be addressed in the future. Development of a direct sampling interface to the mass spectrometer to avoid extended sample collection times is recommended. This should reduce sampling artifacts, decrease the possibility of alteration of the sample during collection, and shorten analysis times to allow for on-line monitoring. In addition, a significant drawback is the

non-quantitative nature of the measurement. A quantitative measurement would transform our ability to draw conclusions based on the data. In addition, a large number of peaks are observed in the mass spectrum. Pattern recognition algorithms should be developed to better constrain reaction pathways, and project bulk physical properties.

2.4 Acknowledgments

The authors are grateful to Prof. Yehia Mechref for helpful discussions and collecting the mass spectrometer data. The authors are also very grateful to the authors of several manuscripts previously appearing in the literature in which peaks for the high resolution mass spectra have been reported. These data are a valuable resource to the community.

Table 2.1 Properties of compounds that are located at identical coordinates of alternate classification schemes. See Donahue et al., 2012 and Kroll et al., 2011^{80, 82} for details of the alternate schemes. Every compound on this list can be resolved in the 3D coordinate system presented in this work.

Compound	Formula	Mean C _{ox} state	# C atoms	Vapor pressure (mm Hg)	k _{OH} (cm ³ molecule- sec) × 10 ⁻¹¹	Henry's law constant (atm-m ³ mol ⁻¹)
<i>C oxidation state approach</i>						
Pentene	C ₅ H ₁₀	-2	5	635	2.87	0.38
Pentanol	C ₅ H ₁₂ O	-2	5	2.2	0.83	1.30 × 10 ⁻⁵
Pentanethiol	C ₅ H ₁₂ S	-2	5	21.4	5.4	8.10 × 10 ⁻³
Pentylamine	C ₅ H ₁₃ N	-2	5	30	3.58	2.45 × 10 ⁻⁵
Leucic acid	C ₆ H ₁₂ O ₃	-1	6	0.002	1.1	2.65 × 10 ⁻⁷
Benzene	C ₆ H ₆	-1	6	87.2	0.194	5.30 × 10 ⁻³
Hexane-2,5-dione	C ₆ H ₁₀ O ₂	-1	6	0.688	0.566	7.40 × 10 ⁻⁹
2,5-Dimethylfuran	C ₆ H ₈ O	-1	6	49.4	13	6.55 × 10 ⁻³
5-Hexenenitrile	C ₆ H ₉ N	-1	6	2.15	2.78	3.40 × 10 ⁻⁵
Dimethylthiophene	C ₆ H ₈ S	-1	6	5.91	3.07	3.60 × 10 ⁻³
Butanediol	C ₄ H ₁₀ O ₂	-1.5	4	0.0748	1.59	1.86 × 10 ⁻¹⁰
Butadiene	C ₄ H ₆	-1.5	4	2110	6.6	0.0736
3-buten-1-amine	C ₄ H ₉ N	-1.5	4	68.3	5.91	5.5 × 10 ⁻⁶
Tetrahydrofuran	C ₄ H ₈ O	-1.5	4	173	1.41	0.0001
Tetrahydrothiophene	C ₄ H ₈ S	-1.5	4	15	1.5	0.00024
Putrescine	C ₄ H ₁₂ N ₂	-1.5	4	2.33	6.62	3.50 × 10 ⁻¹⁰
<i>Volatility basis set approach</i>						
Cadaverine	C ₅ H ₁₄ N ₂	-1.6	5	1.01	6.76	4.90 × 10 ⁻¹⁰
Decane	C ₁₀ H ₂₂	-2.2	10	1	1.15	6.74
m-xylene	C ₈ H ₁₀	-1.25	8	7	2.45	0.006
Thiophenol	C ₆ H ₆ S	-0.667	6	1.4	1.1	0.000338
Dichlorobenzene	C ₆ H ₄ Cl ₂	-0.33	6	1.74	0.04	0.00388
Decatriene	C ₁₀ H ₁₆	-1.6	10	1.58	14.7	0.102

-Values are from AOP-WIN predictions – may be subject to uncertainty/error

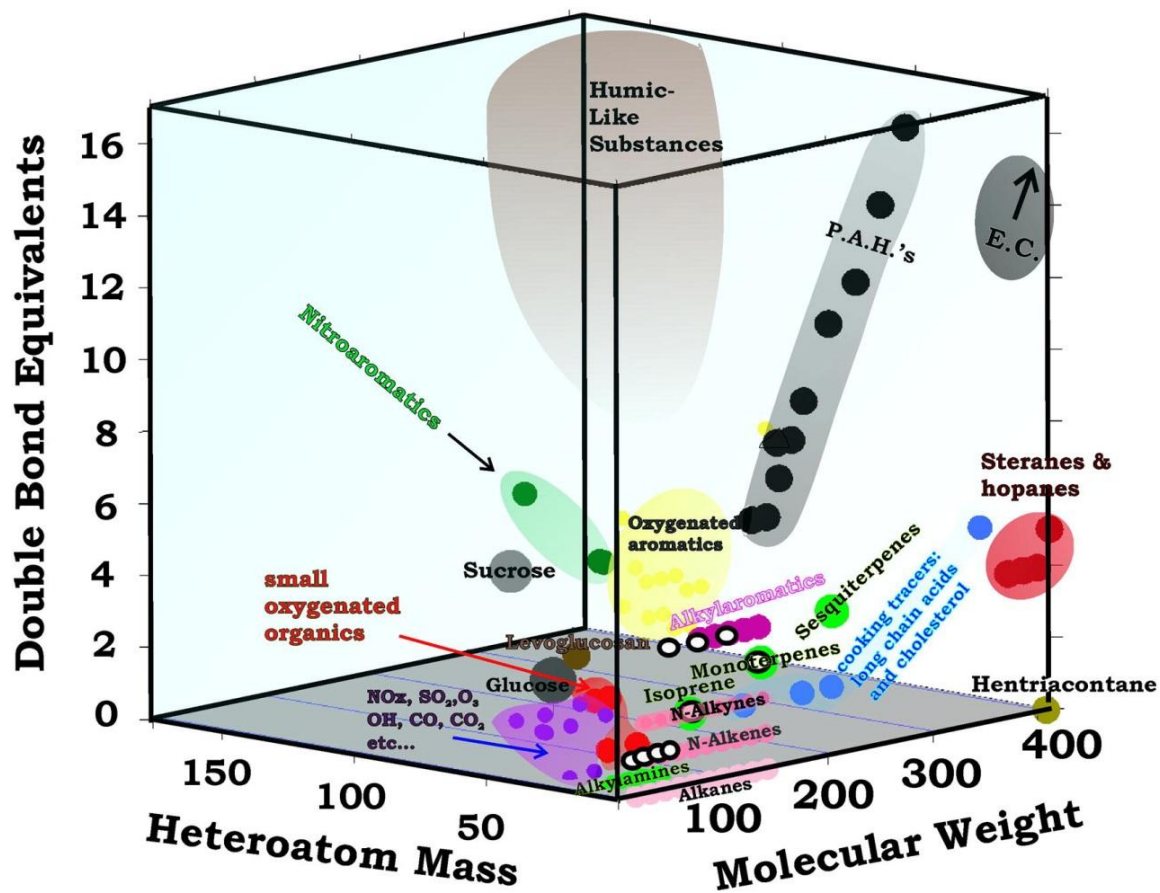


Figure 2.1 Distribution of common organic components of atmospheric aerosol in the 3D space. The dimensions were chosen to effectively sort organic matter in aerosol by volatility, polarity, water solubility, and reactivity. In turn, these chemical and physical properties affect atmospheric lifetimes via chemical attack and wet or dry deposition rates. Use of exact heteroatom mass to describe functionalization maintains chemical information and allows rapid determination of the exact heteroatoms present. The open circles in the plot are a few of the most common VOCs as reported by Zheng et al. (2009). The molecular-based approach allows building a coupled vapor/aerosol phase model.

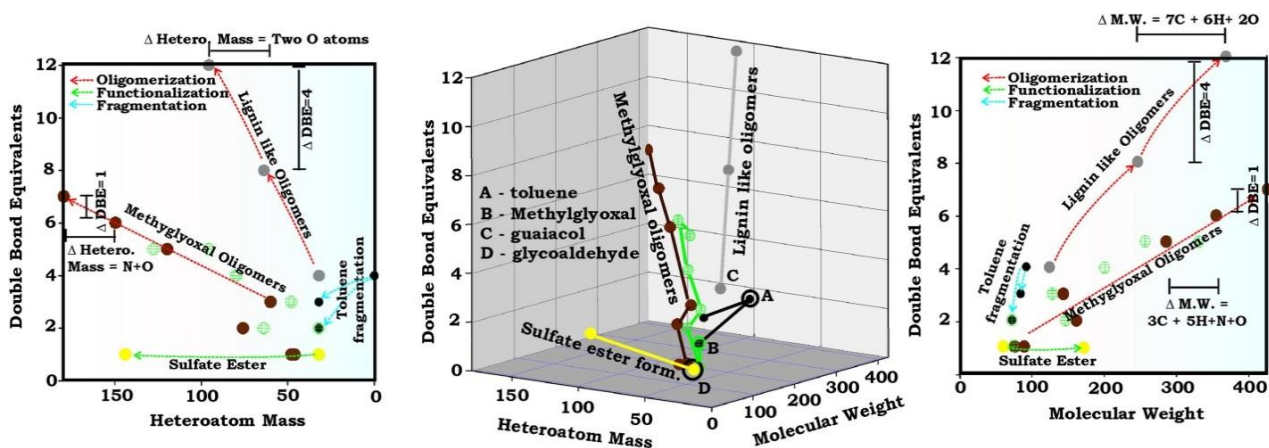


Figure 2.2 Reaction trajectories in the 3D space. Light blue arrows – fragmentation; red arrows – oligomerization; green arrows – functionalization (addition of O, N, S etc...). Knowledge of an expected or proposed reaction mechanism allows prediction of the reaction trajectory in the 3D space. The presence of reactants or products for any hypothetical reaction can be assessed from data as in Figure 2.6.

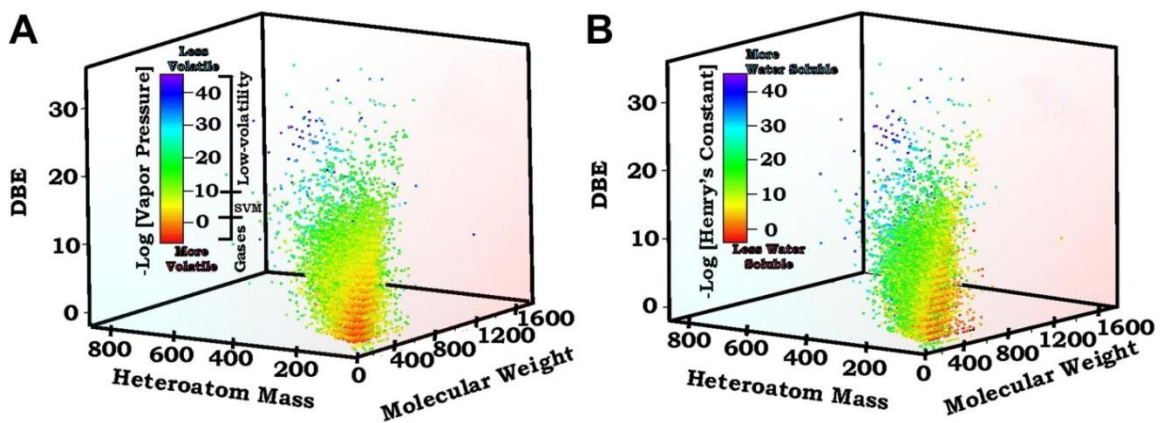


Figure 2.3 Physical and chemical properties of organic compounds can be correlated to coordinates in the 3D space. Plots for vapor pressure (A), and Henry's law constant (B). SVM is semi-volatile material.

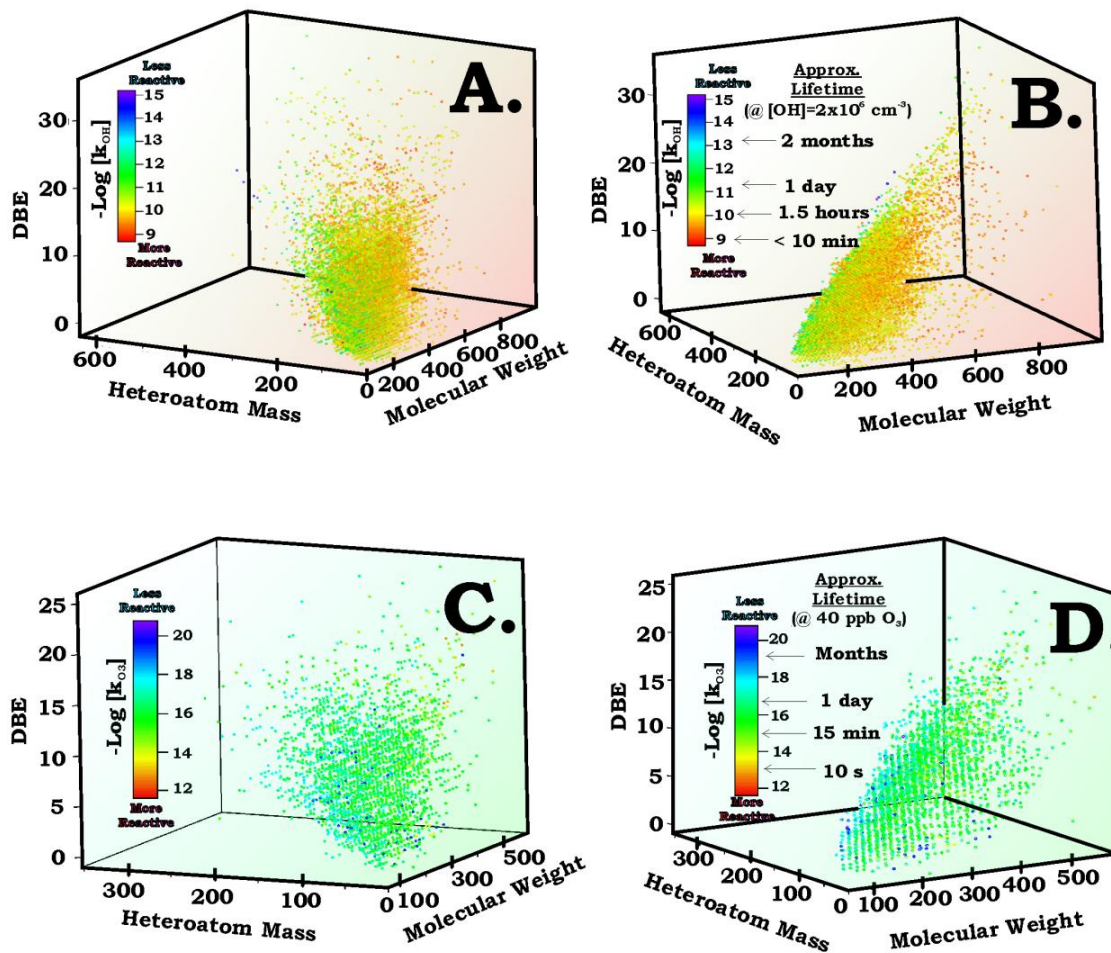


Figure 2.4 Plots of QSPR predicted rate constants for reaction with hydroxyl radical (OH) (A,B), and ozonolysis rate constant (C,D) for test compounds considered in this study. The plots in A-D appear from differing aspect ratios for clarity.

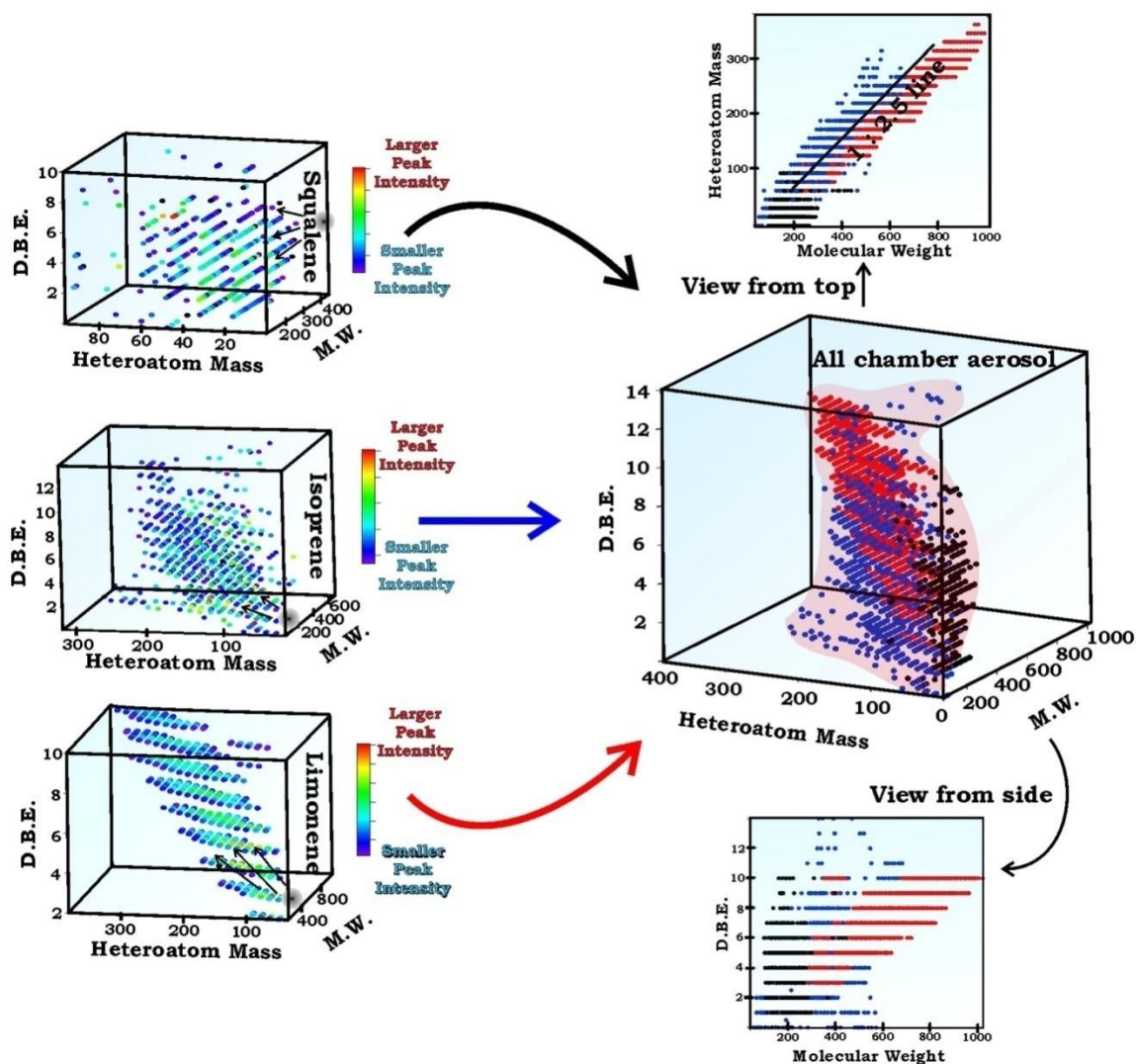


Figure 2.5 Distribution of squalene (black), isoprene (blue) and limonene (red) secondary organic aerosol (SOA) in the 3D space. The gray spheres in figures on the left describe the position of the starting VOC. Each colored sphere represents an organic compound detected through HR-ESI-MS. As observed on the right, the lab generated secondary aerosol is often confined to the region between <10 D.B.E., <1000 M.W. and <400 heteroatom mass. An approximate 1:2.5 ratio between heteroatom mass and total mass is noted. The isoprene and limonene data is from Nguyen et al. (2010)¹²⁹ and Bateman et al. (2009).¹³⁰

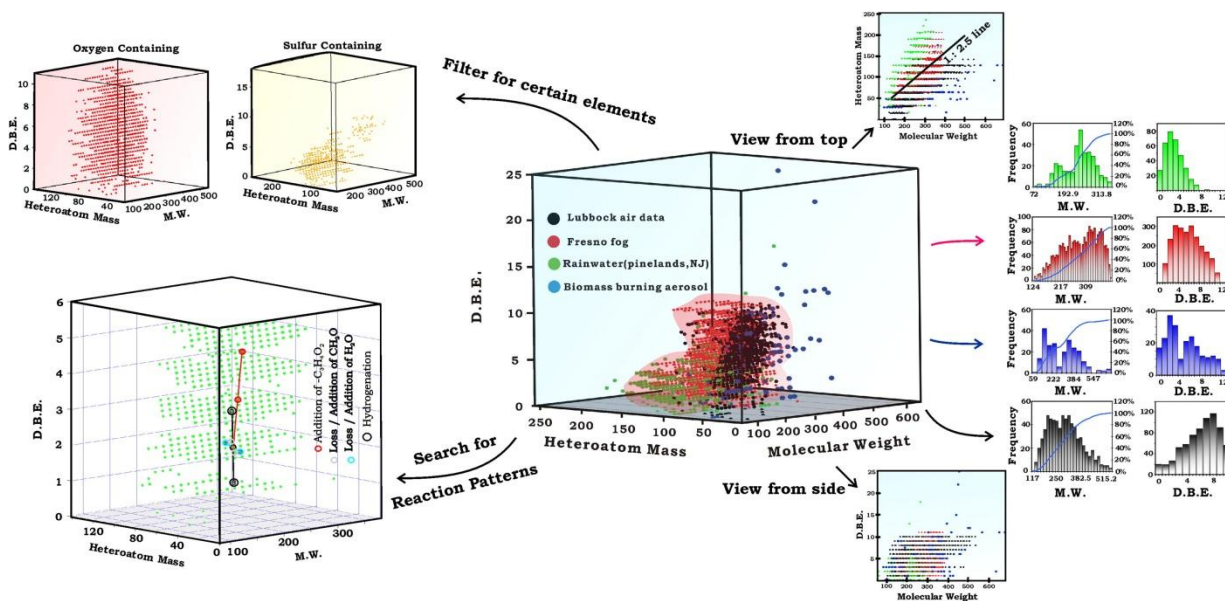


Figure 2.6 Center – Distribution of organic matter observed for ambient aerosols in the 3D coordinate system. Right – Histograms of molecular weight and DBE distributions for the samples. Biomass data, Fresno fog data, and rainwater data are from Laskin et al. (2009),³⁵ Mazzoleni et al. (2010),⁹⁷ and Altieri et al. (2009).⁹⁸ As observed, ambient organic aerosol often occupies the region <10 D.B.E., <500 M.W., and <200 heteroatom mass in the 3D space. Left – The figures on the top left illustrate the distribution of all observed peaks from the combined data set through element specific filters. A point appears only if the specified element is present in the molecular structure. The figure on the bottom left illustrates reaction trajectories from a randomly chosen starting point. In this case, substances consistent with formulas for all proposed reaction paths are observed.

CHAPTER III**LIGHT SCATTERING AND EXTINCTION MEASUREMENTS COMBINED
WITH LASER-INDUCED INCANDESCENCE FOR THE REAL-TIME
DETERMINATION OF SOOT MASS ABSORPTION CROSS SECTION***Analytical Chemistry* **2013**, 85, 9181-9188**3.1 Introduction**

The highly refractory and strongly light absorbing carbonaceous material known as black carbon (BC) is ubiquitous in our environment. BC encompasses a variety of materials including (but not limited to) char, biochar, charcoal, elemental carbon (EC), and soot. Therefore, the exact molecular or atomic composition of BC is often unknown or uncharacterized. Rather, BC is usually described by its refractory and light absorbing nature. The subset of BC, commonly referred to as soot, is produced during combustion when unburned carbon-containing materials condense from the vapor phase. Soot frequently is composed of grape-like aggregates of carbon nanospheres with diameters < 100 nm. This type or fraction of BC has recently been termed nanosphere soot (ns-soot) by Buseck et al.¹³⁵ In this manuscript we consider the black material, commonly called soot or black carbon, derived from a kerosene flame. Using transmission electron microscopy (TEM) we determined that the black material produced exhibits the characteristics of ns-soot, and in turn, adopt this terminology. An alternative name for the material we quantitate via laser-induced incandescence is refractory black carbon (rBC) as advocated by Petzold et al.⁵¹ For the purposes of this manuscript we use rBC and ns-soot as synonyms, although this may not be the case for all samples. Freshly produced ns-soot often forms fractal, chain aggregates. These aggregates are believed to become more compact during atmospheric processing when ns-soot can become embedded or immersed within other materials.¹³⁶⁻¹³⁸

Atmospheric BC (here intentionally all-inclusive) is believed to play significant roles in Earth's carbon cycle and climate. For instance, Bond *et al.* recently suggested that black carbon exerts a radiative forcing in excess of $+1 \text{ W} / \text{m}^2$ on Earth's energy balance.⁴⁷ If accurate, this warming effect is second only to carbon dioxide's greenhouse

warming. BC is believed to exert its warming influence through a variety of mechanisms including direct absorption of sunlight in the atmosphere, alteration of cloud optical properties and lifetimes, and deposition on snow and ice packs,¹³⁹ causing increased melt in polar regions. In addition, BC often contains polycyclic aromatic hydrocarbons (PAHs) that are known to be mutagenic and carcinogenic.¹⁴⁰⁻¹⁴² Methods of quantifying soot in air include a thermo-optical procedure that comprises the NIOSH 5040 standard,^{52, 143} use of filter-based instruments such as aethalometers,¹⁴⁴⁻¹⁴⁶ particle-soot-absorption-photometers (PSAP),⁵⁴ photoacoustic spectroscopy⁵⁵ and laser-induced incandescence (LII).^{147, 148}

The LII technique employs a high-peak-power laser to rapidly heat the sample to $>3000^{\circ}\text{C}$. The sample reaches such high temperatures that it incandesces and produces broadband visible emission for a few μsec after the laser pulse. The intensity of incandescence can be related to soot volume fraction or mass concentration through calibration. As an analytical technique, LII offers similar advantages to laser-induced fluorescence – the ability to measure against a dark background and saturation of signal at high laser power. Both advantages lead to favorable figures of merit for sensitivity and precision. An LII instrument that can measure incandescence of single particles in the low femtogram range has recently been commercialized by Droplet Measurement Technologies.¹⁴⁹ The Single Particle Soot Photometer (SP2) probes incandescence of particles within a Nd:YAG laser resonator allowing laser fluences of approx. $3 \text{ MW}/\text{cm}^2$. The SP2 has been used in the recent HIPPO campaign to map atmospheric concentrations of soot over wide swaths of the globe.^{59, 150}

Because of the success of LII measurements for tracking soot mass concentrations, we became interested in combining the aerosol albedometer recently developed in our laboratory with LII measurements. The albedometer simultaneously measures light scattering, extinction, and absorption (by difference) on dispersed aerosol particles. In principle, combining the optical property measurements with an independent assessment of soot mass concentration through LII can provide direct determination of soot mass absorption cross section (M.A.C, m^2 / g). M.A.C. is an important parameter that

describes the degree of light absorption per-unit-mass concentration of soot (e.g. BC) as outlined in the following equation:

$$b_{abs} = M.A.C. \times [BC] \quad (10)$$

where the absorption coefficient is b_{abs} (m^{-1}) and $[BC]$ is the mass concentration in g / m^3 . The M.A.C. value can be used to directly link mass emission estimates with optical absorption and climatological effects of soot. Light-scattering theory and select laboratory measurements suggest that when soot becomes coated with non-volatile or semi-volatile materials the M.A.C. can increase by a factor of 1.5 – 4 through optical lensing.¹⁵¹⁻¹⁵⁸ However, companion measurements on dried, atmospheric aerosols have not yet detected a large absorption enhancement.^{159, 160} Understanding the magnitude of such an enhancement is crucial for modeling radiative transport in Earth's atmosphere and for delineating the climate effects of soot aerosol. The hybrid LII / albedometer instrument described within allows the direct measurement of soot mass absorption cross section in nearly real-time, and at atmospherically relevant concentrations (low $\mu g / m^3$). Therefore, the device is a significant addition to the toolbox of analytical methods for the analysis of soot aerosols.

3.2 Methods

3.2.1 Description of Optical Measurements Using the Aerosol Albedometer with Laser-induced Incandescence.

A schematic of the optical setup used is shown in Figure 3.1. In the experiment, cavity ring-down spectroscopy (CRDS) is conducted on a dispersed aerosol sample placed within a transparent glass tube that is essentially a flow-through optical cell with the laser beam propagating along its central axis. The CRDS experiment provides a measurement of the aerosol extinction coefficient (b_{ext} , Mm^{-1}) by measuring the time constant (τ) of the exponential decay of light intensity as it circulates in the optical cell. An integrating sphere is constructed around the CRDS optical cell to measure scattering coefficient. The aerosol scattering coefficient (b_{scat} , Mm^{-1}) is measured by ratioing the

scatter channel signal to the CRDS channel signal and calibrating this ratio to those observed for gases of known optical loss.^{76, 77, 161, 162}

The LII measurement is carried out immediately after the CRDS cell. The aerosol is routed into a 15 cm diameter stainless steel sphere. The optical axis of the sphere contains two 0.635 cm diameter holes to allow laser beam passage. The cell is sealed by two long-pass optical filters with cut wavelengths in the 780 – 850 nm range. These filters act like windows for the NIR laser light, but block visible light from entering the sphere thereby creating a dark background against which to make incandescence measurements. The interior surface of the sphere is coated with a highly reflective paint. A port for a photomultiplier tube and housing (Newport 70680) is affixed at a random location on the sphere. The photomultiplier tube (PMT) used for LII signal detection was biased at -1124 V using a DC power supply (SRS-PS310). Current produced by the PMT is passed through a 50 Ω load and digitized with an 8-bit, 100 MHz, 1 Gs / sec oscilloscope (Tektronix 1012B) set to trigger off the laser Q-switch line. The peak-peak measurement function of the scope is employed to measure and log the LII signal response with signal averaging (N=128 averages). For the 20 Hz laser repetition rate used, this corresponds to an LII averaging time just over 6 sec. A delay time of > 1 μ s after the laser pulse was used. After the LII measurement, the aerosol was routed into a 3λ particle-soot-absorption photometer (PSAP, Radiance Research) for a companion absorption measurement. The PSAP was also used to quantify ns-soot mass concentration. The PSAP instrument collects particles onto a filter while simultaneously measuring the optical transmittance of the particle-laden filter compared to a reference filter. For all experiments, only light absorption for the green channel (530 nm) was considered. Indicated light absorption coefficients were used to estimate ns-soot mass concentration (μ g / m³) using a mass absorption cross-section of 13.1 m² / g advocated by Subramanian *et al.* for the green PSAP channel.¹⁶³ Volumetric flow rate through the entire optical setup was 2.4 – 3.6 LPM. A clean air mirror purge flow of 0.2 - 0.25 LPM was used to prevent particle deposition onto the CRDS mirrors. A significant concern to quantitation is that the LII process will induce changes to the observed PSAP signal or mass absorption

efficiency causing systematic biases in the calibration. However, cycling the LII laser on and off was found to not influence the PSAP signal for uncoated kerosene soot. This result likely occurs because the LII probe beam occupies <0.01% of the LII sphere volume. Most soot in the sample may never enter the LII probe beam and simply passes to the PASP unaltered.

3.2.2 Scanning Mobility Particle Sizing (SMPS) and Particle Size Selection.

A SMPS system was used to obtain aerosol particle size distributions as measured through equivalent electrical mobility diameters. The SMPS was assembled from a TSI 3080 electrostatic classifier, a TSI 3081L differential mobility analyzer (DMA), and a TSI 3772 condensation particle counter (CPC). N-Butanol was used as the fill fluid in the CPC, and a sample-to-sheath flow rate ratio of 1:10 was maintained in the experiments. A sample flow rate of 0.6 LPM was commonly employed for size distribution measurements. The SMPS was run under computer control using software provided by the manufacturer. For the experiments in which ns-soot was coated with ammonium nitrate, we used the classifier to size select 300 nm diameter particles prior to analysis. Again, the 1:10 ratio was maintained to achieve a narrow bandwidth of particle sizes.

3.2.3 Transmission Electron Microscopy (TEM) Analysis.

Fresh kerosene ns-soot was collected on Lacey Formvar/Carbon 200 mesh copper TEM grids (Ted Pella, 01881-F) by passing a gentle flow of a soot-laden air stream through a glass Pasteur pipet containing the grid. Sampling times were ≤ 20 min. The TEM analysis was conducted by the research group of Peter Buseck at the LeRoy Eyring Center for Solid State Science at Arizona State University. Images were obtained on a FEI Tecnai electron microscope at an accelerating voltage of 200 kV and recorded using a Gatan Orius CCD camera. To make the analysis statistically meaningful, 10 to 12 regions of interest (ROIs) for each sample grid were imaged at both low- and high-magnifications (up to 195 kX). Images were obtained for each ROI in order of increasing magnification with a broad electron beam to be confident that the electron radiation had no noticeable influence on the morphology and structure of the ns-soot particles.

3.2.4 Generation & Characteristics of Soot and Ambient Sampling.

Kerosene ns-soot was generated by combustion of kerosene (Coleman Fuel) in a fabric-wicked camping lantern (Walmart). The lamp was operated within a fume hood for venting of fumes. A ¼ inch diameter polyethylene tube approx. 30 m in length was used to direct the ns-soot to the LII optical chamber where it was diluted substantially prior to analysis with zero air controlled with a mass flow meter. The quantity of ns-soot reaching the optical cell was controlled through carefully actuating the clean-air flow-controller valve. The ns-soot generated by the kerosene lamp is uncoated, and largely void of residual organics as supported by thermo-gravimetric (TGA) data reported in Figure B.1 of Appendix B which illustrates very little mass loss until approx. 550° C, a temperature at which ns-soot has been shown to oxidize.

Kerosene ns-soot was also collected from the inside of the kerosene lamp housing. This material was dispersed in deionized water (reverse osmosis) by sonication and atomized into micron-sized droplets by using a TSI 9302 atomizer. When appropriate, glycerol (0.015 mL / mL), ammonium nitrate (1 mg / mL), or ammonium sulfate (2.5 mg / mL) was added to the solution placed in the atomizer to generate internally mixed aerosol in which the ns-soot is embedded within the inorganic salt or coated with glycerol. After generation in the atomizer, the sample was dried in a diffusion dryer (TSI 3095) and passed into a mixing tee for dilution with clean, dry air. The relative humidity of the resulting atomized samples was low, typically < 20%. For the results presented in Table 3.1, the resulting dry aerosol was then introduced into the thermal denuder / optical cell without size selection. However, for the experiments in which the coated aerosol was humidified (see Figure 3.5B) we used the electrostatic classifier to size select 300 nm particles for analysis after the initial drying. The size-selected aerosol was then routed into a large mixing chamber where dry or humid air could be added to control the relative humidity of the sample considered.

Ambient sampling occurred through a PM 2.5 cyclone (BGI Inc.) at a third story window in the Chemistry building at Lubbock TX. The airstream was passed directly into the thermal denuder / optical system through 1.27 cm or 0.95 cm diameter tubing.

Sampling occurred at various times between May 9 and 27, 2013. Conditions during sampling varied, but sampling was avoided during the mineral dust episodes that are common to the region.

3.2.5 Thermal Denuding.

For select experiments we employed a thermal denuder at the inlet of the optical cell that heats the aerosol to evaporate semi-volatile materials. The heated section of the denuder was constructed from a 30-cm length of 1.25 cm diameter stainless steel tubing. Heating was achieved through use of a heating tape, and temperatures were monitored with an IR thermometer accurate to 2°C. Temperatures between 120 – 250 °C were used. After the heated section, the aerosol was passed into a tube that contained charcoal adsorbent to remove condensable vapors. The sample was then introduced to the aerosol albedometer / LII apparatus.

3.3 Results and Discussion

3.3.1 LII Response Function and Effect of Coating/Mixing State.

LII signal responses were always non-linear and a third-order polynomial was used to relate observed LII signal and ns-soot mass concentration (see Figure B.2 in Appendix B). Since atmospheric BC particles are commonly coated or embedded within sulfates, nitrates or organics,^{51, 136, 137} systematic errors will result if the LII response of the particles are affected by mixing state. Previous investigators found LII response is largely independent of particle mixing state and ns-soot morphology.¹⁶⁴ To determine the extent to which mixing state affects our LII experiments we pass the aerosols through a thermal denuder that can be heated to > 120 °C in order to evaporate semi-volatile materials prior to analysis. The heater can be turned on and off, allowing removal of condensable materials from the sample in a controlled manner. Alternatively, we have altered the relative humidity of the sample during the analysis (Figure 3.2D). Raising the relative humidity causes deliquescence of hygroscopic aerosol, resulting in an aqueous phase mixed with the ns-soot.

Particles used in the analysis were generated by atomizing aqueous suspensions of ns-soot with a small amount of glycerol (0.015 mL / mL soln.), or ammonium nitrate (1 mg / mL) added to the solution. The droplets are dried and diluted with filtered air prior to analysis. The BC cores of the particles were polydisperse with a mass equivalent diameter near 200 nm (see Appendix B Figure B.4). The data in Figure 3.2A is for an experiment in which ammonium nitrate was added to the atomizer with the ns-soot collected from the kerosene lamp. About 23 minutes into the experiment the denuder was turned on, and a large drop in single scatter albedo (SSA) and scattering / extinction occurred as the non-light-absorbing ammonium nitrate was removed from the aerosol phase although, the indicated BC mass concentration sensed through the LII approach was unaffected by the dramatic change in mixing state.

Figure 3.2B illustrates results of an experiment in which glycerol was used as the coating material and the thermal denuder was turned on at approx. 47 minutes after beginning of the experiment. A clear and obvious drop in the observed SSA was observed after the denuder reached temperature. This decrease resulted from evaporation of the non-absorbing glycerol from the aerosol phase (also see drop in scatter coefficient). However, the soot concentration measured through LII was unaffected by the denuding.

In Figure 3.2C, an identical experiment was carried out on ambient aerosol present in the atmosphere of Lubbock, TX on May 23 2013. Heating the aerosol reduced the measured extinction and scatter by approx. 50%. However, the observed LII response was again largely unaffected by the thermal treatment. Here, the SSA did not change appreciably since the concentration of BC was very low in this sample (only 0.2– 0.3 $\mu\text{g} / \text{m}^3$).

In Figure 3.2D, we raised the relative humidity of the coated ammonium nitrate + ns-soot sample beyond the deliquescence point of ammonium nitrate. As observed, as the relative humidity (RH) rose, the aerosol accumulated a significant amount of water in an aqueous phase. However, the soot mass concentration sensed by the LII detector did not indicate a dramatic shift in signal intensity upon deliquescence. We should note that

similar humidification experiments conducted on ammonium sulfate coated ns-soot aerosol did exhibit a signal decrease of 10-20% upon deliquescence when the laser pulse energy was 20 mJ. This decrease in signal could be eliminated when the laser pulse energy was increased to 28 mJ.

All of the results of Figure 3.2 suggest that the LII response we measure is unaffected by mixing state / coatings and therefore in good agreement with previous work.¹⁶⁴ This also makes sense physically to a large degree since a “back of the envelope” calculation based on our best estimates yields an expected energy density added to a single 150 nm soot particle in excess of $> 9000 \text{ J / g}$ ($\sigma_{\text{abs}} = 2.4 \times 10^{-10} \text{ cm}^2$, $D_p = 150 \text{ nm}$ soot, 130 mJ / cm^2 laser fluence). Since the heat capacity of such a particle is expected to be in the $10^{-14} - 10^{-15} \text{ J / K}$ range (this is an uncertain value – do not cite) – one could expect a temperature increase $> 4000 \text{ K}$. This calculation is in relatively good agreement with LII theory, but is clearly not exact (ignores latent heat due to phase changes and alteration of specific heat with temperature). It is however useful to realize the energy density available for vaporization of coatings and subsequent LII signal generation. Such realization helps justify the experimental result that coatings do not appear to affect the LII signal response.

3.3.2 Consequences of the LII Measurement: ns-Soot Morphology Changes

The rapid LII heating of soot particles to between 2500 – 4000 K within 100 ns of the laser pulse may produce significant changes to the particles. We investigated the effect of 532 and 1064 nm laser light on the size distributions and morphology of kerosene lamp ns-soot. The size distributions were obtained using an electrostatic classifier with a condensation particle counter (Figure 3.3A), and morphology was studied with transmission electron microscopy (TEM). When illuminated with $< 14 \text{ mJ / cm}^2$, the most probable electrical mobility diameter of the soot aggregate particles was between 100 and 200 nm. As laser power increased (combined 532 and 1064 nm beam), a large shift in number concentration towards particles with small diameters ($D_p < 50 \text{ nm}$) occurred, but not when only 532 nm light was used with the CRDS mirrors in the beam path. Many small particles were produced due to lasing with the 1064 nm beam, as

confirmed by the TEM analysis (Figure 3.3B) which illustrates new soot fragment particles present on the TEM grid (some of which are circled in the figure). New particle formation was reported and characterized extensively by Michelson et al.¹⁶⁵ The small particles produced via lasing with 1064 nm light exhibit large differences in microstructure (Figure 3.3C). In some cases, the nanoparticles have hollow cores with surrounding onion-like layers, and in other cases, ribbon-like structures occur. This structural reorganization was also observed by Michelson et al.¹⁶⁵ and Vander Wal et al.¹⁶⁶ and suggests the ns-soot aggregate chains do not simply disassemble into primary particles, but rather undergo a dramatic reorganization consistent with vaporization and condensation.

Regardless of the mechanism of such transformation, the scanning mobility particle sizer (SMPS) results of Figure 3.3A suggest this process begins to occur for the kerosene soot sample when the laser fluence was approximately 30 - 40 mJ / cm². This fluence is significantly lower than what other investigators have reported for the threshold. For instance, Michelson *et al.* report fluences of 120 mJ / cm² and 220 mJ / cm² are required for new particle generation using 532 and 1064 nm, respectively.¹⁶⁵ Kruger *et al.* have reported observing a change in soot size distribution by virtue of laser irradiation at 532 nm when irradiance was 120 mJ / cm².¹⁶⁷ However Stipe et al. reported particle production at far lower fluence (70 mJ / cm²) when using UV photons of 193 nm.¹⁶⁸ The exact cause of the discrepancy in required laser fluence is not immediately clear, but the onset of new particle formation occurred at laser fluences far below those typically used for LII analysis. Therefore, our results support the idea that it is not possible to perform LII measurements without inducing significant morphological changes in the soot sample. Because of the change in soot morphology, light scattering / extinction measurements and LII measurements should occur either sequentially in time (with CRDS / nephelometry first) or in parallel after spitting the sample and LII should be considered a destructive detector.

3.3.3 Effect of Coating/Mixing State on ns-Soot M.A.C.

Figure 3.4 illustrates a time course plot of an experiment in which a sample containing ns-soot and glycerol was atomized, dried, diluted, and passed through the thermal denuder prior to optical analysis. Initially the thermo-denuder was at room temperature, but at approx. 20 minutes the heating device was turned on. As observed in the figure, single scatter albedo (SSA) dropped from about 0.7 to 0.4, indicating that non-absorbing components including glycerol were evaporated. The observed M.A.C. value dropped from about 7 to 5 m² / g during the same period of time during this trial. At about 45 minutes, the heating was turned off. Both SSA and M.A.C. quickly rose to levels originally encountered. A second heating cycle was then applied beginning at about t = 75 minutes with nearly identical results. Clearly, both SSA and M.A.C. change dramatically as a result of heating for glycerol-coated soot. As expected, the SSA drops during heating. This is consistent with non-absorbing material being removed from the aerosol phase. The corresponding drop in observed M.A.C. suggests the glycerol coating has enhanced the light absorption by soot present in the sample. This enhancement was always observed for glycerol-coated ns-soot. Table 3.1 lists the results of multiple trials for glycerol coatings as well as for atomized soot coated with dry ammonium sulfate and dry ammonium nitrate. Although the absolute values for M.A.C. measured during these experiments varied considerably between soot samples, the average absorption enhancement (M.A.C. coated / M.A.C. thermal denuded) for glycerol coated soot was 1.41 ± 0.06 . The observed absorption enhancements for soot embedded within solid materials was clearly smaller than that which was observed for glycerol. For instance, the average enhancement for ammonium nitrate coated soot was 1.06 ± 0.09 and for ammonium sulfate the M.A.C. enhancement was 1.10 ± 0.07 . These enhancements are likely the result of core-shell type lensing that has been discussed previously.¹⁵¹⁻¹⁵⁸ It is interesting to note that enhanced absorption with glycerol (liquid) coating was always large and quite easy to detect. However, the solid sulfate and nitrate coatings produced a much smaller average enhancement. This may indicate that soot can fully immerse within the liquid droplets of glycerol, and M.A.C. enhancement via core-shell lensing is fully realized in this spherically symmetric sample. Again, the large variation in M.A.C.

values between trials is believed to result from actual differences between soot samples used in the analysis and/or in calibration.

Figure 3.5 illustrates the results of experiments in which samples of fresh kerosene ns-soot (Figure 3.5A) and ammonium nitrate coated ns-soot (Figure 3.5B) were humidified. For this plot, measured M.A.C. values were normalized to the mean of values observed for the dry case ($RH < 40\%$) for each trial. The polydisperse and hydrophobic fresh ns-soot exhibited no change in M.A.C. as the humidity was increased. Soot is known to adsorb a few statistical monolayers of water at high relative humidity, but apparently this was not enough to cause observable alteration of M.A.C. Alternatively, for the ns-soot coated with ammonium nitrate (generated with the atomizer and size selected to $D_p = 300$ nm), a clear and large increase in measured M.A.C. resulted when the sample humidity was increased above about 60%. The ammonium nitrate coating made the ns-soot more hydrophilic, allowing an aqueous phase to develop on the particle surface at high humidity (similar results were also observed for ammonium sulfate coatings). The resulting increase in observed M.A.C. is very reminiscent of what was observed for liquid glycerol coatings (Figure 3.4). Since the particle accumulates water, its diameter would be expected to grow. The inset to Figure 3.5B shows the measured optical particle diameter (measured from observed scatter cross-section) as well as the modeled diameter using the AIM model II¹⁶⁹ and assuming a 150 nm soot core. These data suggest the particle would be expected to grow from the original 300 nm dry diameter to approximately 500 nm. This knowledge allows us to account for truncation effects for the nephelometer via the approach of Qian et al.¹⁷⁰ This procedure results in a scattering coefficient correction of 3-5%, and the data in the figure has been corrected (this process reduces observed M.A.C.). Even after correction, the observed M.A.C. clearly increases during the formation of a liquid aqueous drop containing the ns-soot. The results illustrated in Figure 3.5 are very similar to data reported by Mikhailov et al¹⁵⁵ for experiments carried out at higher concentrations of particles present within an extinction cell.

3.3.4 M.A.C. Values for Dispersed Kerosene ns-Soot and Ambient Aerosol

We have also measured mass absorption cross sections (M.A.C) for dispersed kerosene ns-soot (uncoated, direct from lamp) and for ambient aerosols. As a quality control measure for the ambient measurements, we have used data points only when BC mass concentration exceeded $0.25 \mu\text{g} / \text{m}^3$ in an effort to reduce relative uncertainty. Data were collected at limited times during May 2013 at Lubbock, TX and no attempts were made to characterize the mixing state of the BC detected. Table 3.1 reports average M.A.C. values and standard deviations (s) for the uncoated kerosene ns-soot and ambient soot aerosol. Figure B.3 (a)-(e) in Appendix B report histograms of observed optical properties and BC concentrations during the ambient monitoring. As observed in Table 3.1, kerosene soot had an M.A.C. of $9.3 \text{ m}^2 / \text{g}$ while ambient soot had an average M.A.C. of $8.4 \text{ m}^2 / \text{g}$. Given the large standard deviation of both measurements (2.7 and $5.9 \text{ m}^2 / \text{g}$) no statistical difference between these two samples is suggested. However, use of a consistent calibration standard coupled with direct probing of the soot mixing state may allow improved analysis in the future. Nonetheless, the soot mass absorption cross sections are in relatively good agreement with those advocated by Bond and Bergstrom,¹⁵² Fuller et al¹⁵⁴ and Khalizov et al.¹⁷¹

3.4 Conclusions

Coupling the aerosol albedometer with laser-induced incandescence (LII) allows direct measurement of soot mass absorption cross sections with one minute time resolution. The LII signal provides a convenient and sensitive measurement of soot mass concentration and is independent of soot mixing state. Lab-generated, polydisperse ns-soot particles coated with glycerol, ammonium nitrate, ammonium sulfate, and an aqueous solution all demonstrated increases in M.A.C. relative to the uncoated case. The largest increase in M.A.C. was for the liquid coatings. The LII process alters the physical properties of soot, and therefore should be regarded as a destructive technique. The M.A.C. values for dispersed kerosene ns-soot aerosol are in good agreement with literature values. Ambient BC exhibited mass absorption cross-sections very similar to that of fresh kerosene ns-soot. However, we constrained our analysis to samples

containing $> 0.25 \mu\text{g} / \text{m}^3$ soot concentration which may bias measurements towards plumes that are fresher, less dilute, and less atmospherically processed. This premise is further supported by the fact most measurements in which $\text{BC} > 0.25 \mu\text{g} / \text{m}^3$ were transient plumes, lasting only a few minutes in duration.

The combination of the aerosol albedometer with LII measurements of soot concentration provides a powerful method for the real-time determination of the M.A.C. However, accuracy requires that BC is responsible for the light absorption by the aerosol. Samples influenced by significant mineral dust or “brown-carbon” (both potential light absorbing substances) may result in falsely large values of M.A.C. The influence of these absorbers on the signal can be discovered by tracking increases in the observed Angstrom exponent (AE) with a multiwavelength instrument (soot $\text{AE} = 1$; others have AE of > 2). Both mineral dust and “brown carbon” exhibit increased absorption at shorter wavelengths. Optical measurements made at 532 nm may dramatically reduce the effects of these absorbers as compared to measurements at blue or violet wavelengths, but the interference may not be eliminated for all samples in which non-BC absorptive loading are high (e.g. dust events, biomass smoke plumes). A technical improvement would be expected if the measurement wavelength was shifted toward red wavelengths where both mineral dust and brown carbon absorb negligibly. Nonetheless, the measurement technique presented is valuable to help unravel soot’s effect on Earth’s climate. The technique is particularly useful for continued investigation into whether coating and/or internally mixing soot enhances light absorption by atmospheric aerosols.

3.5 Acknowledgments

Funding for this research was provided by Texas Tech University / the State of Texas and the National Science Foundation under grant 1004114. The statements and opinions expressed within this manuscript may not reflect those of the National Science Foundation or the State of Texas. Peter Buseck and Jun Wu conducted the TEM analysis and provided the images with support from NSF grant AGS-1032312. L. Ma collected samples for the TEM analysis and performed the particle size distribution experiments.

Q. Zhang, T. Cao, Y. Wei and J. Thompson performed remaining experiments and analyzed resultant data.

Table 3.1 Observed enhancement in soot mass absorption cross-section (m^2 / g) as a function of mixing state and coating material. Experiments were conducted on polydisperse, sub-micron aerosol. The large variability in M.A.C. observed between trials is believed to result from differences in soot samples used for analysis or for calibration.

Experiment	M.A.C. (coated/denuded) (m^2/g)	Mean SSA (coated/denuded)	M.A.C. enhancement (coated/denuded)
Atomized Glycerol and Soot	11.9 / 8.0	0.79 / 0.42	1.49
Atomized Glycerol and Soot	14.3 / 10.3	0.78 / 0.39	1.39
Atomized Glycerol and Soot	6.96 / 5.0	0.73 / 0.46	1.38
Atomized Glycerol and Soot	6.6 / 4.8	0.70 / 0.44	1.36
Mean enhancement observed			1.41 \pm 0.06
Atomized ammonium nitrate and soot	8.9 / 8.3	0.55 / 0.41	1.07
Atomized ammonium nitrate and soot	8.9 / 9.1	0.91 / 0.39	0.98
Atomized ammonium nitrate and soot	9.0 / 7.8	0.86 / 0.42	1.15
Mean enhancement observed			1.06 \pm 0.09
Atomized ammonium sulfate and soot	9.12 / 7.93	0.65 / 0.45	1.15
Atomized ammonium sulfate and soot	9.38 / 7.92	0.64 / 0.48	1.18
Atomized ammonium sulfate and soot	13.9 / 13.3	0.63 / 0.48	1.04
Atomized ammonium sulfate and soot	6.3 / 6.0	0.65 / 0.56	1.05
Mean enhancement observed			1.10 \pm 0.07
Sample	Mean M.A.C. \pm 1s (m^2/g)	Mean SSA	M.A.C. enhancement
Fresh kerosene ns-soot	9.3 \pm 2.7	0.27	N/A
Dry ambient aerosol	8.4 \pm 5.8	0.97	N/A

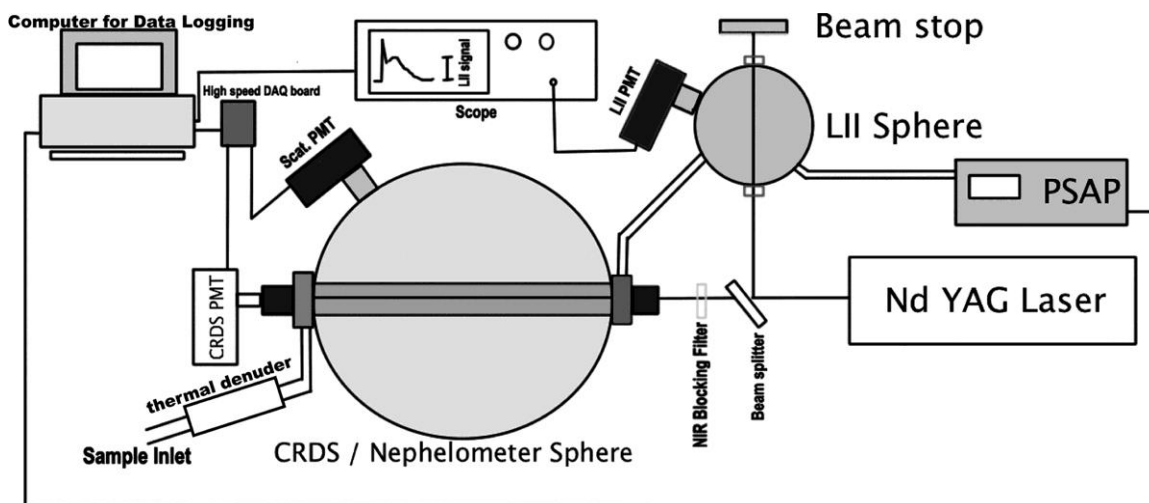


Figure 3.1 Experimental apparatus. A beam splitter directs a portion of the laser beam into an integrating sphere for LII. The beam transmitted through the beam splitter is used for cavity ring-down spectroscopy (CRDS) / nephelometry after removal of the near-infrared (NIR) light. The NIR blocking filter protects the HR mirrors from possible laser damage and prevents alteration of the soot during CRDS measurements.

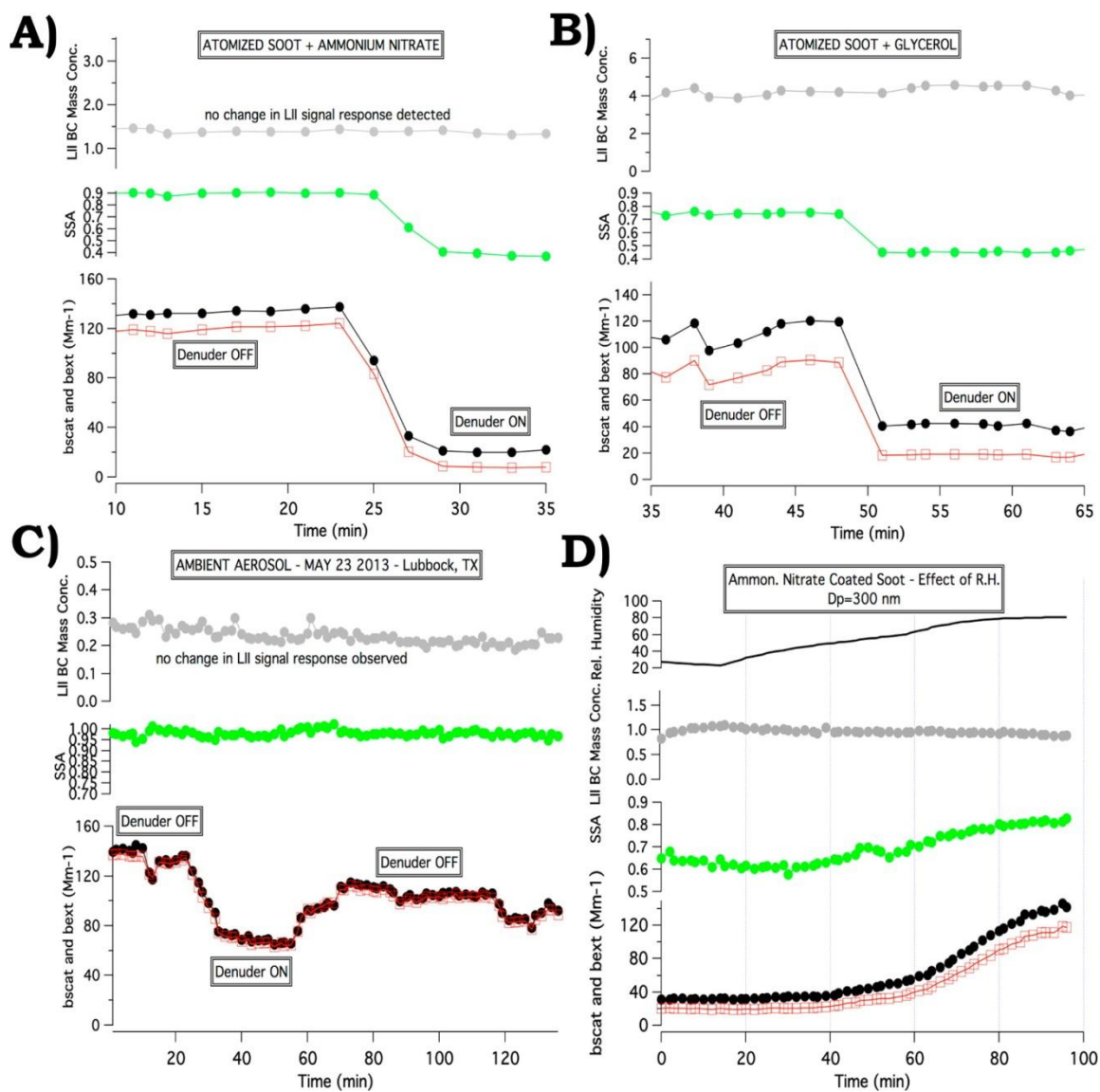


Figure 3.2 Observed LII response as a function of coating state for (A) ammonium nitrate coated soot at low humidity, (B) glycerol-coated soot, (C) ambient aerosol, and (D) ammonium nitrate coated soot at various relative humidities. For all samples the LII response was unaffected by the presence of coatings. Evaporation of semivolatile material in the thermal denuder is confirmed via the dramatic dip in single scatter albedo (SSA) in panels A and B. Absorption of water in panel D is confirmed by the rise in SSA. Laser fluence was 160 mJ/cm². Here, BC and ns-soot are synonyms.

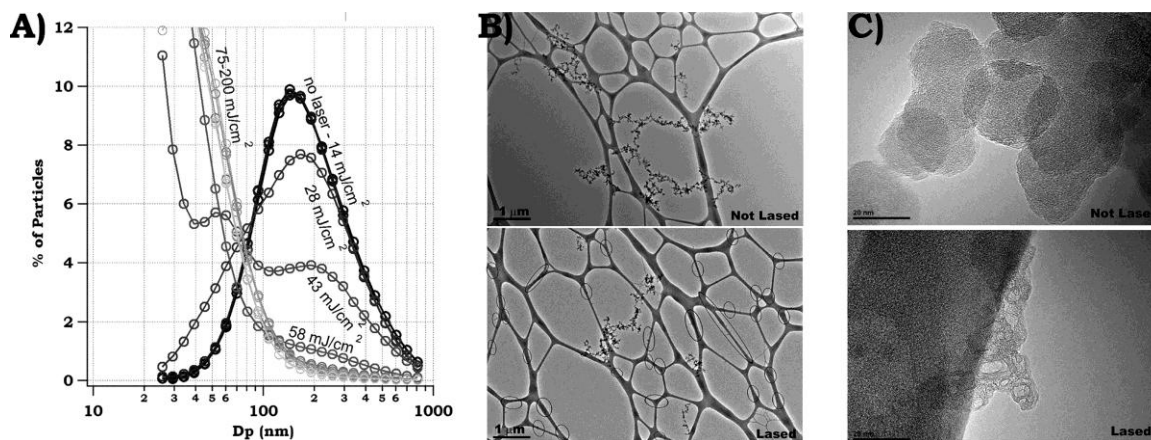


Figure 3.3 (A) Observed size distributions of fresh kerosene ns-soot at various laser fluences. At laser fluences $>28 \text{ mJ/cm}^2$, a significant shift in particle size distribution was observed. (B) TEM images of lased and unlased kerosene ns-soot. A large number of very small fragment particles (some circled) are observed in the lased samples. The TEM grid appears like a spider web in the image. (C) High-resolution TEM images of fresh ns-soot that has been lased and nonlased ns-soot. Lased soot exhibits vastly different morphology on the nanoscale, including formation of graphitic layers with hollow particle cores. In panel C the scale bar is 20 nm.

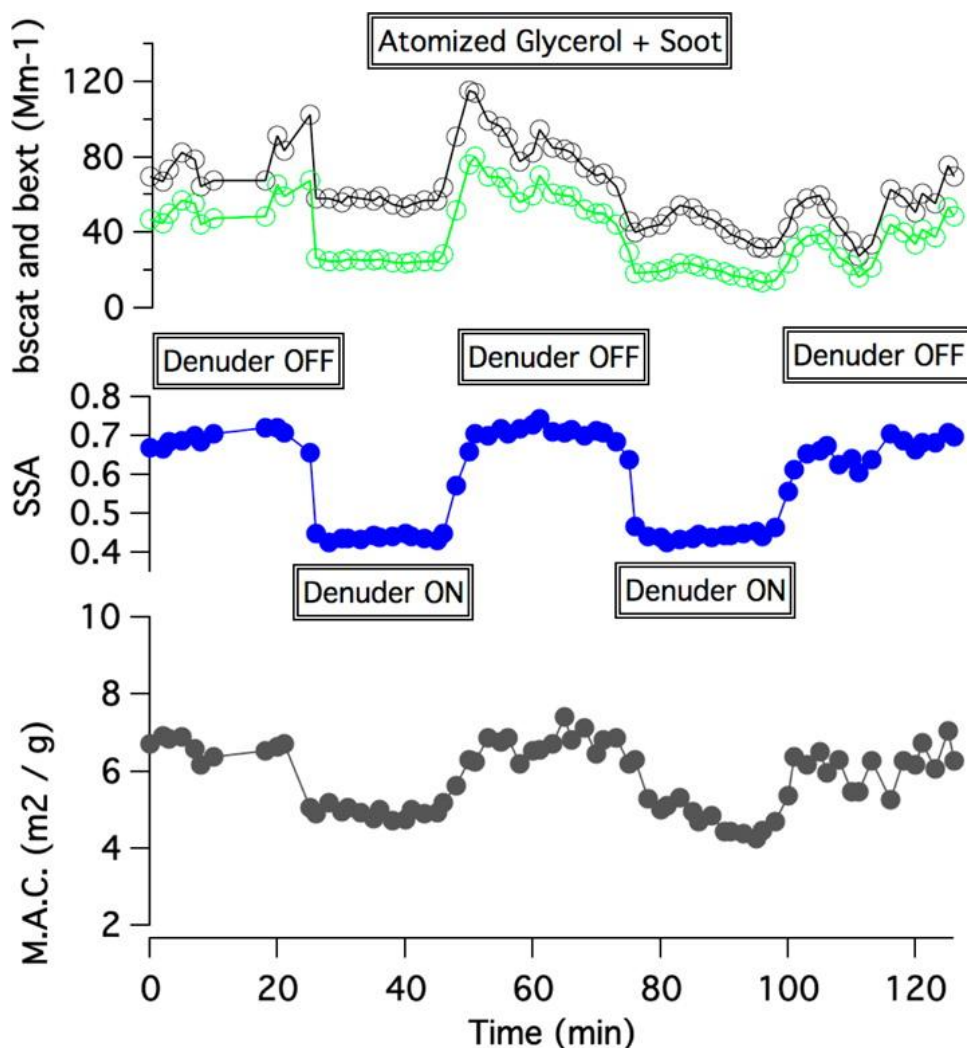


Figure 3.4 Plot of experimental data in time for atomized glycerol plus ns-soot. At approximately 23 min, the thermal denuder was turned on. At approximately 50 min the denuder was turned off. The cycle was repeated at approximately 75 and 100 min. As observed, the SSA dropped dramatically when the thermal denuder evaporated soot coatings. The indicated M.A.C. also dropped when the coated soot was denuded indicating the glycerol coating caused an absorption enhancement. In the top trace the green data is scatter coefficient. Laser fluence was 160 mJ/cm^2 .

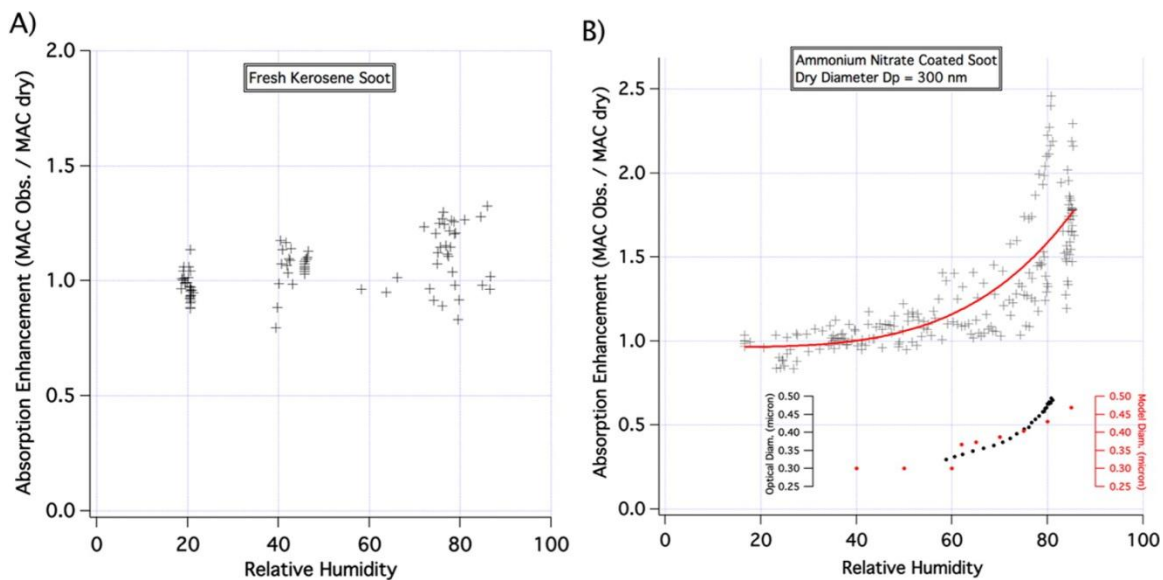


Figure 3.5 Effect of relative humidity on M.A.C. value for (A) fresh kerosene ns-soot and (B) atomized BC internally mixed with ammonium nitrate. The ammonium nitrate makes the particle more hygroscopic, and as the particles deliquesce the optical absorption is enhanced. The inset to panel B plots the observed optical diameter and modeled particle diameter as a function of relative humidity. The particles in panel B were size-selected to 300 nm dry diameter using an electrostatic classifier prior to humidification. Laser fluence was 160 mJ/cm^2

CHAPTER IV

ATMOSPHERIC BLACK CARBON CAN EXHIBIT ENHANCED LIGHT ABSORPTION AT HIGH RELATIVE HUMIDITY

Atmospheric Chemistry and Physics Discussion **2013**, 13, 29413-29445

4.1 Introduction

Black carbon (BC; a.k.a. soot) aerosol present in earth's atmosphere is believed to exert a positive direct radiative forcing (DRF) on Earth's climate between +0.08 – 1.27 Wm^{-2} due to its efficient light absorbing nature⁴⁷. This estimate suggests BC is the second most important climate-forcing agent behind long-lived greenhouse gases. However, the degree to which BC warms the Earth-atmosphere system is intimately linked to the efficiency with which soot absorbs sunlight. The mass absorption cross section (MAC, m^2g^{-1}) is commonly used to relate absorption of light to BC mass loading. The MAC is defined here as the ratio between the aerosol absorption coefficient (b_{abs} , Mm^{-1}) and the BC mass concentration ($\mu\text{g m}^{-3}$).

$$M. A. C. = \frac{b_{\text{abs}}}{[BC]} \quad (11)$$

One uncertainty in constraining DRF by BC is assigning accurate MAC values. A review of theory and literature has led Bond and Bergstrom¹⁵² to report an MAC for fresh BC between 4-8 m^2g^{-1} . However, it is well known that BC quickly becomes internally mixed (embedded or coated) within other materials including hygroscopic sulfates, nitrates, and organics once released into the atmosphere.^{58, 64, 136-138, 172-180} Internal mixing of soot increases its ability to uptake water at high humidity (fresh uncoated soot is not hygroscopic) and both light scattering theory and laboratory measurement suggest the MAC value increases when BC become coated during atmospheric processing.^{49, 50, 152, 155, 158, 171, 181-187} Bond et al.¹⁵⁷ and Fuller et al.¹⁵⁴ have postulated absorption enhancement factors of 2-5 fold were reasonable for thickly coated BC, however, attempts to measure absorption enhancement for dried atmospheric aerosols sampled in California found very modest enhancements.^{159, 160} More recent data collected in Europe has suggested higher absorption enhancements (roughly 40%) for coated atmospheric BC.¹⁸⁸ These results

suggest significant differences may exist between locations as has been suggested by Jacobson.¹⁸⁹ At present, it is believed the discrepancy between expected results and ambient samples results from BC core in the dried, authentic samples not exhibiting a core-shell geometry necessary to observe large absorption enhancements. However, formation of an aqueous phase at high relative humidity (RH) may allow the light absorbing inclusions to be located at random locations within a spherical droplet, thereby allowing enhanced absorption to occur. Since water vapor is by far the most abundant, easily condensed species in Earth's atmosphere it is reasonable to explicitly study the absorption enhancement phenomenon as a function of relative humidity. The condensation of water into a BC containing particle would provide sufficient mass to grow thick coatings required for largest absorption enhancement. Increased absorption by coated soot at high RH may help explain recent observations for China of increased solar heating rates aloft when BC was mixed with sulfate aerosol¹⁹⁰ or allow additional understanding of enhanced absorption within clouds.¹⁹¹ Therefore, results presented within this manuscript have significant impact on modeling both direct and indirect mechanisms of climate forcing. Yet, future measurements at additional times and locations are required to build a more comprehensive data set.

4.2 Experimental methods.

A schematic of the experimental setup for ambient aerosol measurement is shown in Figure 4.1.

4.2.1 Sampling conditions

Aerosol sampling occurred in an urban area within Houston TX (Lat: 29.685741, Long: -95.295668) from 19-24 July 2013. The location was 4-5 km NNW of William P. Hobby airport and was located at a Texas Commission on Environmental Quality (TCEQ) monitoring site (CAMS 416). During sampling outdoor temperatures ranged from 23.9-33.3°C with a relative humidity range of 45-90%. Winds were generally < 16 kmh⁻¹ and frequently from the south or southeast. Aerosol was sampled at 3-4 LPM into a 3 m long length of 1.25 cm inner diameter copper tube without size selection and passed through a window into a climate-controlled building where the measurement devices were located.

The tubing inlet was approximate 4 m a.g.l. Temperature within the building was $23.6 \pm 3^\circ\text{C}$, and the drop in temperature was used to promote high values of relative humidity for the sample. Flow through the copper tube was split at a $\frac{1}{2}$ " Swagelok tee ("first tee" in Figure 4.1). One arm of the tee was routed to a diffusion dryer (TSI 3062 with silica gel/ Drierite desiccant) to lower the sample humidity and then to an electronic 3-way ball valve (Assured Automation, EV1S1V1) that was actuated under computer control. The second line from the mixing tee (e.g. wet-air-line) was routed directly to the electronic valve with a 1 m length of 0.93 cm diameter conductive rubber tubing (TSI Inc.). The common port of the electronic valve was connected to the albedometer with a 2.5 m length of 0.93 cm diameter conductive rubber tubing. Cycling the electronic valve every 15-30 min under computer control allowed sequential probing of wet and dried ambient aerosol.

4.2.2 Measurements

Measurements of aerosol scattering, extinction and absorption coefficients (b_{scat} , b_{ext} , b_{abs} ; Mm^{-1}) were carried out using the aerosol albedometer as described in previous literature.^{76, 77, 161, 192} Scattering calibration occurred against R-134a¹⁹³ as typical for the experiment. Sample relative humidity was measured at the outlet of the albedometer optical cell within a Vaisala HMP 60 sensor. Uncertainty in this RH sensor is specified to be +5%. While the aerosol albedometer offers improved truncation performance for nephelometry, size dependent corrections to b_{scat} on the order of a few percent are often necessary. To correct the optical data at high RH, a hygroscopic growth model must be used to estimated aerosol diameters and truncation effects considered. Qian et al¹⁷⁰ developed a correction scheme for the albedometer b_{scat} measurements based on particle size parameter that we have employed to correct data. The hygroscopic growth model used was developed from a combination of observational data from the literature, and the AIM thermodynamic model (http:// www.aim.env.uea.ac.uk/aim/aim.php). Growth factors as a function of relative humidity are illustrated in Figure 4.2. The model used (red data points) seeks the median of observational data at RH values below 90%. Since observational data was not frequently available at $\text{RH} > 90\%$, we assumed hygroscopic

growth consistent with ammonium sulfate at very high RH. Assuming the aerosol behaves as such may overestimate hygroscopic growth above 90% RH. Overestimating hygroscopic growth via this model would lead to smaller values of absorption and consequently smaller M.A.C. This encourages a conservative estimated of MAC increase at high RH.

The SP2-D Single Particle Soot Photometer was also plumbed into the setup immediately after the albedometer to monitor rBC mass concentration and mixing states. The SP2 purge flow was filtered dry air. During field measurement, the SP2 was configured to save data for between 1 of 5 and 1 of 20 particles observed. The instrument was also periodically configured to collect/save data only 1 of 5 min. Both of these conditions were used to save hard drive space on the instrument (accumulates GB of data daily), but assuming random sampling this should not affect results. After the field campaign, the SP2 was calibrated in the laboratory against atomized, and size selected fullerene soot (Alfa Aesar) and SP2 indicated diameters agreed well with electrostatic selection diameters as shown in Figure C.1 of the Appendix C. The Probe Analysis Package for Igor (PAPI) provided by DMT was used for data analysis of SP2 data. The dry-air sampling line also included a sampling port for a Droplet Measurement Technologies (PAX) Photoacoustic Extinctionmeter (also measures b_{abs} and b_{scat}) that sampled the dry aerosol at 1 LPM.

4.3 Results and Discussion

4.3.1 BC Mixing State Analysis

Incandescence lag time analysis was used to probe BC mixing state from raw SP2 data. The approach we used was highly influenced by previous literature.^{58, 163, 177, 180} For the current analysis an incandescence lag time delay of $1\ \mu\text{s}$ was used as a criteria to determine whether a BC containing particle was uncoated or coated. Here, lag time delay is defined as the difference between peak incandescence signal and peak elastic scatter signal indicated by the SP2. The lag time delay is believed to result from time required to evaporate non-refractory materials from the BC containing particles as it heats in the

laser beam. To justify the choice of a 1 μs delay, we present the results of Figure 4.3. This figure illustrates plots of scatter – to – incandescence peak ratio vs. lag time for a variety of laboratory generated test aerosols of known mixing state. The panel on the bottom left is for dry, uncoated kerosene soot. Virtually all particles (denoted by data points) exhibited lag time $< 1 \mu\text{s}$. However, when kerosene soot was collected and atomized from suspensions containing either ammonium sulfate, ammonium nitrate or glycerol the observed lag time increased – generally to $> 1 \mu\text{s}$. The increase in scatter / incandescence peak ratio observed is also consistent with the particles being coated. Clearly, the data reflects 1 μs lag time is a good threshold to describe BC coat state. Thus, individual particles measured in Houston were assigned to either being “coated” or “not coated” based on observed lag time – no distinction was made as to the thickness of coating present. Therefore, the coating fraction is defined as the fraction of particles exhibiting a lag time of $> 1 \mu\text{s}$.

4.3.2 BC Size and Mass Concentration

As observed in Figure 4.4A, the daily modes of the mass-equivalent diameter distributions of BC cores sensed by the SP2 were consistently near $D_p = 120 \text{ nm}$. Figure 4.4B illustrates time series plots of rBC mass concentration and coating fraction as well as histograms of observed results. The mass concentration of rBC was between 33 and 5340 ngm^{-3} during the sampling period with an average of 682 ngm^{-3} . The coating fraction varied between approx. 0.2-0.9 with a mean of 0.68. The coating fraction often dropped when concentrated plumes of rBC passed the sampling site. Both results are consistent with local sources being responsible for fresh emissions within very concentrated plumes.

4.3.3 Optical Measurement Results

The mean aerosol absorption, scatter, and extinction coefficients observed on dry aerosol ($< 60\% \text{ RH}$) sampled at the Houston site are summarized in Table 4.1. As reported in the table, mean absorption and scattering coefficients were fairly low compared to measurements from other urban environments. However, the mean $\text{PM}_{2.5}$ mass concentration reflected in the TEOM data, and presented in Table 4.1 agreed

closely with measurements from July 2010-2012 (13.24, 10.71, 14.46 μgm^{-3} , respectively) suggesting we may have experienced similar aerosol mass loadings despite the limited sampling period.

Figure 4.5 illustrates a plot of mass scatter coefficient ($b_{\text{scat}}/\text{PM}_{2.5}$ mass concentration; m^2g^{-1}) vs. sample relative humidity for the Houston data set. Each data point on the graph was a five minute average obtained by dividing the optical measurement by the associated mass concentration. $\text{PM}_{2.5}$ mass concentration was determined via an automated TEOM instrument located within 100 m of the sampling site (operated by TCEQ). As observed in Figure 4.5, the mass scatter coefficient was found to increase a well-known phenomenon.¹⁹⁴⁻¹⁹⁸

We also report measurements of soot MAC (m^2g^{-1}) for aerosol sampled at Houston, TX that exhibit significant absorption enhancement was, on average, affected by the mixing / coating fraction of the BC. Figure 4.6 illustrates data showing the effect of relative humidity on aerosol optics. Again, aerosol was sampled through an inlet that cycled between low and high relative humidity (RH). Water vapor condensed into hygroscopic materials at high RH causing deliquescence of particles and formation of internally mixed aerosol consisting of an aqueous phase and BC of ≈ 120 nm mass equivalent diameter. As illustrated in the figure, cycles of high humidity yielded clear increases in aerosol scattering coefficient (b_{scat}). Indicted aerosol absorption coefficient (b_{abs}) also often increased during cycles of high RH despite mass concentration of BC remaining relatively constant. This is easiest observed within the middle portion of Figure 4.6A. Figure 4.6B illustrates data collected during the morning hours of 24 July. Prior to 450 ks BC aerosol was fairly diluted and was highly coated. During this first period, cycling of MAC in phase with RH was observed. As local traffic/ activities increased during the morning commute (beginning at approx.450 ks), additional fresh BC was added to the local atmosphere and the fraction of BC coated was observed to drop. Simultaneously, it became difficult to detect a large MAC increase a high humidity. This result may be expected since uncoated BC is generally not hygroscopic. However, the differences in MAC enhancement observed between panels Figure 4.6A and B suggest

that the chemical composition, phase, viscosity or other property of the BC coating likely affects MAC alteration at high RH.

The image plot depicted in Figure 4.7 illustrates observed MAC values as a function of RH and coating fraction for all data collected during the sampling period 19-24 July 2013. MAC values in excess of $20 \text{ m}^2\text{g}^{-1}$ were indicated at high RH when a large fraction of BC was coated. Also illustrated within inset B. of Figure 4.7 are median MAC values plotted against RH for low (<0.5), medium ($0.5-0.75$), and high coat (> 0.75) state conditions. The error bars in the graph represent 25-75% tiles. As observed, median MAC increased from approx. 4 to $15 \text{ m}^2\text{g}^{-1}$ as humidity increased from 50-95% for BC samples exhibiting coating fractions of > 0.75 . Such a dramatic increase in MAC was not observed when BC coating fraction was < 0.5 , although medians still exhibited a $\approx 50\%$ increase – even in this case. We attribute this increase to the minority coated BC fraction present. Inset A of Figure 4.7 presents a plot of observed MAC as a function of coating fraction when sample RH was $< 60\%$. Interestingly, the median MAC values increased only marginally from 3.8 to $4.4 \text{ m}^2\text{g}^{-1}$ as median BC coating fraction increased from 0.47-0.78. This small increase (c.a. 15%) could be the result of optical lensing by non-absorbing coatings, but the magnitude of increase in MAC for dried aerosol coatings appears to be small compared to that encountered through RH effects. This result is largely consistent with the marginal absorption enhancement recently reported by Cappa et al.¹⁵⁹ and Thompson et al.¹⁶⁰ for dried aerosol sampled in California. The increased MAC values at high humidity observed in Figure 4.7 are also consistent with modeled projection of 2-5 fold absorption enhancement advocated by Bond et al.¹⁵⁷ and Fuller et al.¹⁵⁴ for light absorbing BC inclusions located randomly within non-absorbing shells. The 3- 4 fold enhancement in MAC observed at high RH also agrees very well with the laboratory work of Mikhailov et al,¹⁵⁵ who observed an absorption enhancement for laboratory generated hydrophilic soot aerosols of 3- 4 fold. In addition, results are similar to the enhancement observed by Wei et al.⁴⁹ for lab generated soot particles internally mixed with sulfate. The highest measurements of MAC observed corresponded to time periods in which the concentration of BC and b_{abs} was low, and RH was high. If any

positive offset bias (incorrect zero measurement) exists in the measurements, it would lead to falsely high MAC values, particularly at low concentrations of BC. In addition, the periods of low BC concentration and low b_{abs} will be prone to the highest relative uncertainty in MAC. Figure C.4 in Appendix C reports propagated absolute uncertainty in MAC using absolute uncertainties of 2 Mm^{-1} for absorption and 50 ngm^{-3} for [BC]. As observed, uncertainty was not constant through the rBC coat fraction and RH space defined in Figure 4.7. This is because high coat fraction tended to be observed for very dilute, aged BC plumes. This uncertainty should be considered a caveat of the data set. However, an analysis conducted using only data when $[\text{BC}] > 0.5 \text{ } \mu\text{gm}^{-3}$ also yielded a 3-4 fold increase of MAC. Also, significant increases in indicated aerosol absorption were also evident in the time – series data upon cycling to high RH without recalibrating step, so positive offset error is likely not to blame for all results. Finally, plots of indicated absorption vs. mass concentration of BC for low RH and high RH subdivisions of the data set yielded different slopes for best-fit lines (slope is MAC). Therefore, we can be confident the MAC enhancement truly exists. However, setting specific quantitative bounds on the enhancement factor remains challenging.

4.3.3.1 Mechanism of Enhanced Absorption

Organic compounds present in the certain aerosol samples can also absorb visible light.^{107, 199, 200} To evaluate whether such compounds were present and could influence results, we collected particles onto a filter and extracted the material with a 20:80 v/v mix of methanol and water. The extracts were filtered through a syringe filter to remove insoluble materials and measured using a standard UV-VIS spectrophotometer and a 1 cm path length cell. Figure C.2 of the Appendix C displays several spectra of the extracts (colored traces) from different dates/times. In addition, a spectroscopic blank taken at the conclusion of analysis is shown in black. The filter extracts exhibited substantial absorption in the near UV between 300-400 nm, but very little or no light absorption in the visible spectral region. Also, back trajectory analysis (Figure C.3 in Appendix C) indicates the sampled air masses originated from over the Gulf of Mexico during the sampling period, a region not heavily influenced by biomass combustion. We conclude

brown-colored carbon containing compounds are not responsible for increases in MAC at high RH observed at 532 nm.

Alternatively, light absorption by BC can be enhanced when BC is fully immersed within an aqueous droplet (here called “core-shell model”) or when BC is present on the droplet’s surface (here called the “sphere-on-sphere model”). Figure 4.8a illustrates the electric field within and near a 2 micro diameter water droplet (normalized to incident field = 1) as modeled with the ADDA discrete dipole code. As observed the internal electric field within the droplet can exceed the incident field (approx. double at many locations). In addition, the largest enhancement occurs within a small volume directly adjacent to the particle on the “shaded side” (e.g. in the optical near-field of the particle). Field enhancements > 10 fold can be encountered in this region, and soot MAC values > 100 m²g⁻¹ are modeled when a soot particle resides within this volume. However, we would expect a soot particle to randomly occupy all volume elements on the surface of the droplet for the sphere-on-sphere model, and orientation averaging is required to describe the enhancement for this non-symmetrical case. The result of Figure 4.8B report modeled MAC values for the core-shell and sphere-on-sphere models using ADDA. As observed, orientation averaging reduces the average absorption enhancement predicted for the sphere-on-sphere case. In fact, after orientation averaging, the mean enhancement expected for the sphere on sphere model is less than the core-shell case. MAC values in the range of 15-20 m²g⁻¹ can only be modeled via the core-shell approach. Therefore, the measurement results presented in Figure 4.7 agree best with the core-shell model. However, we feel the exact physical mechanism by which the absorption enhancement is achieved is still open to further investigation. Given the uncertainty reported in Figure C.4, we cannot completely discount the sphere-on-sphere model (or an alternate model) is producing the enhancement. Attempts to immerse soot within aqueous phases in our laboratory have largely been unsuccessful despite considerable efforts to chemically modify the soot particle surface (e.g. make surface more hydrophilic) by treatment with ozone, nitric acid vapor, natural surfactants, inorganic salts, and combinations of these. Experiments aimed at imaging soot mixed with aerosolized droplets are needed to

confirm the “core-shell” morphology. In addition, more measurements of absorption enhancement at high RH for a variety of locations globally are definitely needed to bring this issue to scientific closure. The chemical composition of soot coatings should simultaneously be tracked to better understand why soot exhibits large MAC enhancements at high RH during certain periods of time, and very little enhancements during others (as in Figure 4.6).

4.4 Significance and Conclusion

The measurement results described within provide evidence for significant absorption enhancement by coated BC aerosol at high humidity. Since BC becomes coated in the atmosphere within 3-5 h of release, this experimental result suggests climate models should include parameterizations that account for increased absorption by soot aerosol at high relative humidity as advocated by Jacobson.²⁰¹ If parameterizations are not included, the actual radiative forcing by soot aerosol may be > 100% more positive. While Figure 4.7 may provide some initial quantitative guidance, we recognize multiple caveats to our experiment. Given the uncertainties associated with our measurements, we are unable to assess whether core-shell or sphere-on-sphere morphologies are most representative of reality. In addition, the “correct” model may depend on the composition of coating of soot surface chemistry. Data shows the magnitude of increase in MAC observed at high humidity clearly varied in time. For some sampling periods, almost no enhancement at high RH was observed, while during others MAC values increased by > 4-fold. This suggests the chemical composition of coatings or the soot source may be important factors to model absorption enhancement at high RH. A more comprehensive characterization of the composition of soot coating material is required to gain additional insight on absorption enhancement at high RH.

4.5 Acknowledgement

Development of albedometer was historically funded by the National Science Foundation. We thank P. Beltz, City of Houston Environmental Health for hosting us during measurements. We are also grateful to G. McMeeking and Droplet Measurement

Technologies for providing a SP2-D for measurements. We are also grateful to Fernando Mercado of TCEQ for providing high time resolution $PM_{2.5}$ data for the site.

Table 4.1 Mean aerosol optical values observed at Houston, TX for dried aerosol (RH < 60%) during 19-24 July 2013

Parameter	Mean	25th %tile	75th %tile
Absorption, b_{abs}	2.9 Mm^{-1}	0.62	3.5
Scattering, b_{scat}	26.0 Mm^{-1}	22	31.7
Extinction, b_{ext}	28.9 Mm^{-1}	23.8	34.6
Albedo, SSA	0.91 Mm^{-1}	0.86	0.97
$\text{PM}_{2.5}$	13.0 μgm^{-3}	8.4	17.7

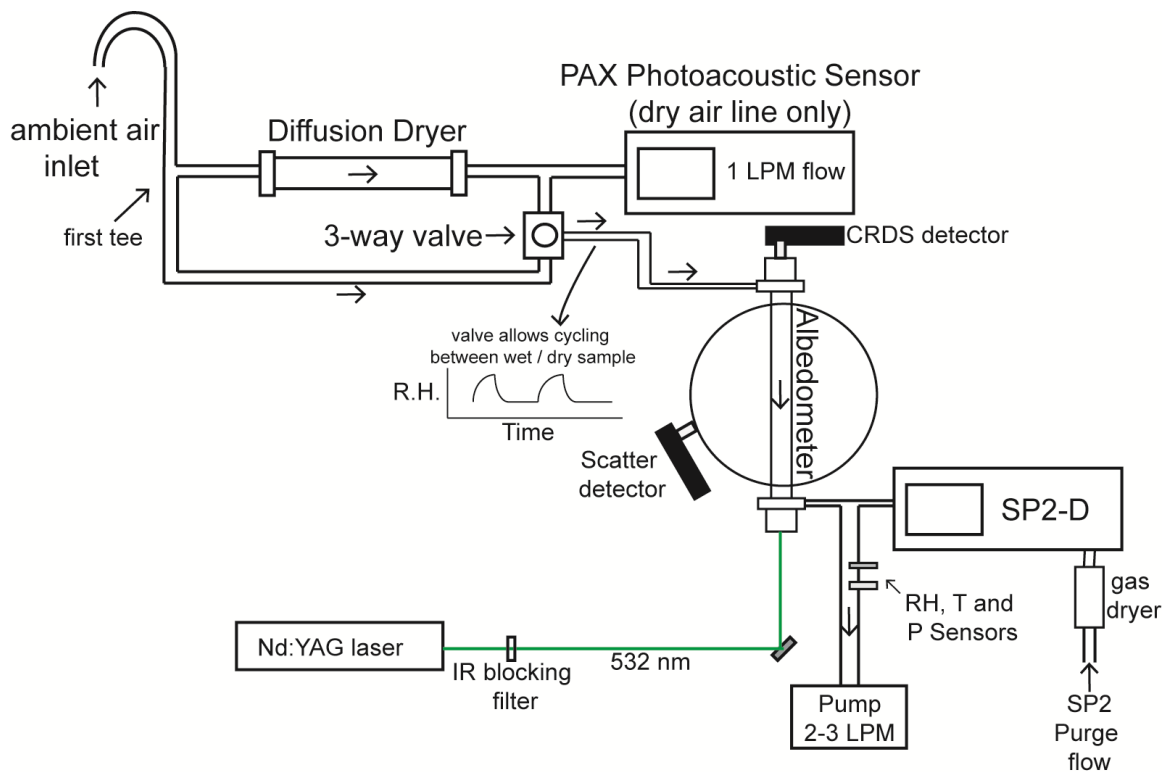


Figure 4.1 Experimental setup for field measurements at Houston, TX.

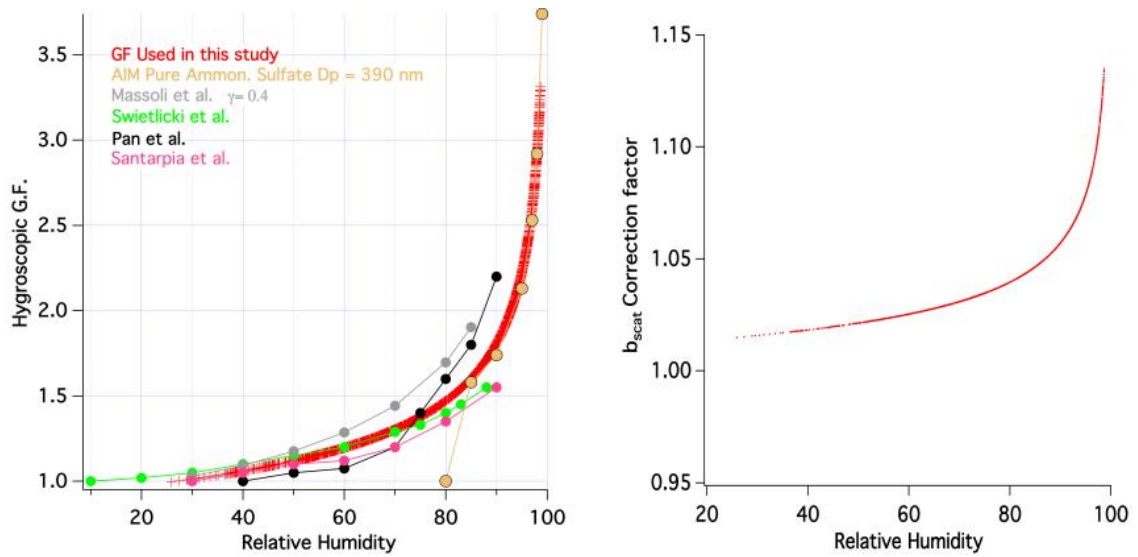


Figure 4.2 Left – Hygroscopic growth factor (G.F) model employed in this study (red) compared to select observational data from the literature²⁰²⁻²⁰⁵ and predicted behavior for pure ammonium sulfate ($D_p = 390$ nm). Right – Correction factor for integrating sphere nephelometer derived from hygroscopic growth model and Qian et al.¹⁷⁰ Scattering coefficients observed were corrected by this multiplier to account for angular truncation effects. Such a correction reduces observed absorption and MAC values compared to the uncorrected case.

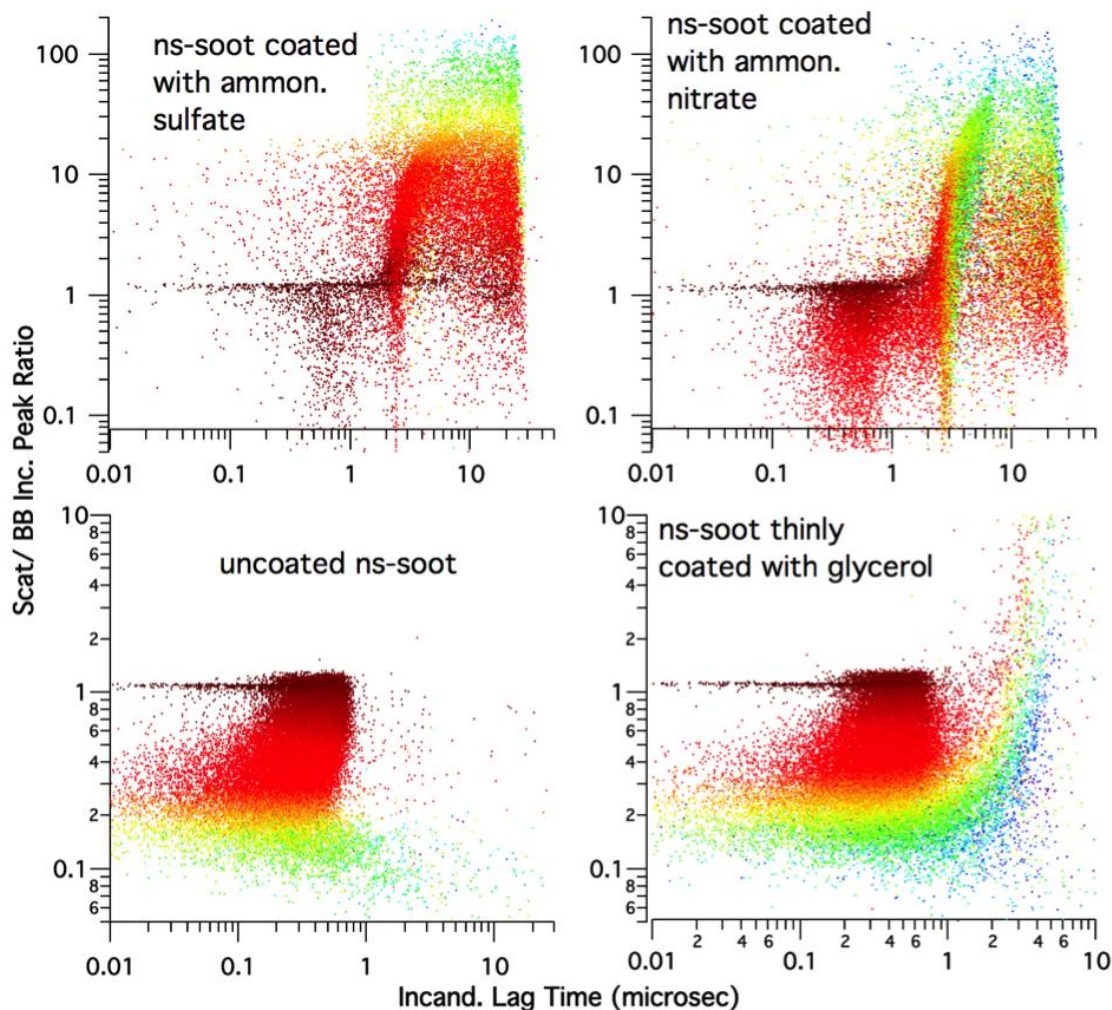


Figure 4.3 Laboratory validation of lag time analysis to assess rBC mixing state. Data is for fresh, uncoated kerosene lamp soot and atomized kerosene lamp soot coated with ammonium sulfate, ammonium nitrate, and glycerol. For fresh, uncoated nanosphere soot (ns-soot) produced by a kerosene lamp the observed SP-2 lag time was $< 1 \mu\text{s}$ for nearly all particles. However, lag time increased to $> 1 \mu\text{s}$ when soot from the lamp was collected, and atomized from aqueous dispersions containing either glycerol, ammonium sulfate or ammonium nitrate. Thus, we have employed a $1 \mu\text{s}$ lag time delay as a criterion for assessing soot mixing state. Color scale indicates rBC particle indicated mass based on incandescence peak area.

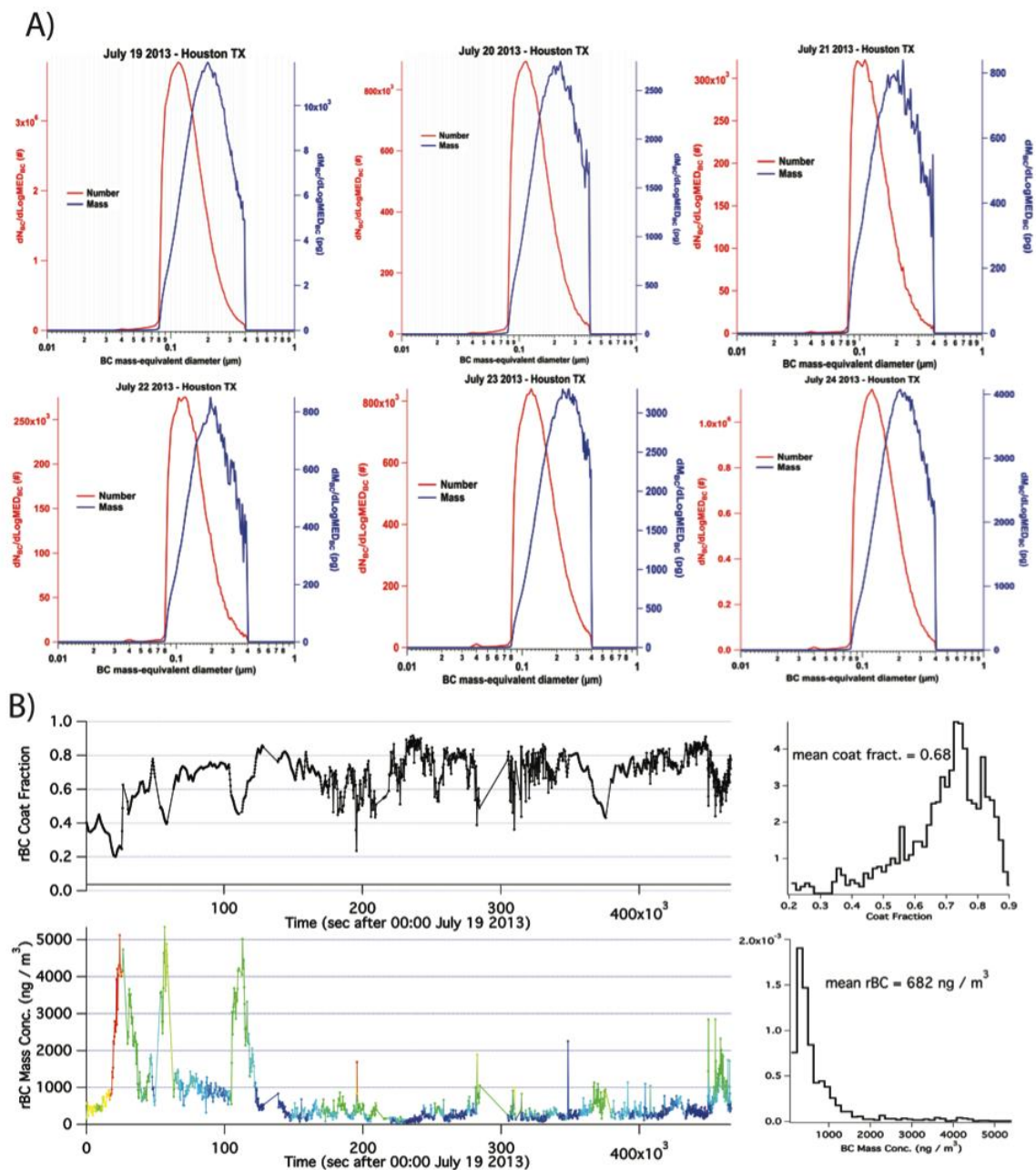


Figure 4.4 (A) Daily average size distributions of rBC cores sampled at Houston, TX as reported by the SP2. Distributions were consistent from day-to-day with modes often near $D_p = 120$ nm. (B) Time series plot of BC coat fraction and mass concentration with histograms summarizing the data. The color scale corresponds to the BC coat fraction data. As observed, periods of high concentration of rBC often exhibited low coat fraction. Mean [BC] = 682 ng m^{-3} for the sampling period.

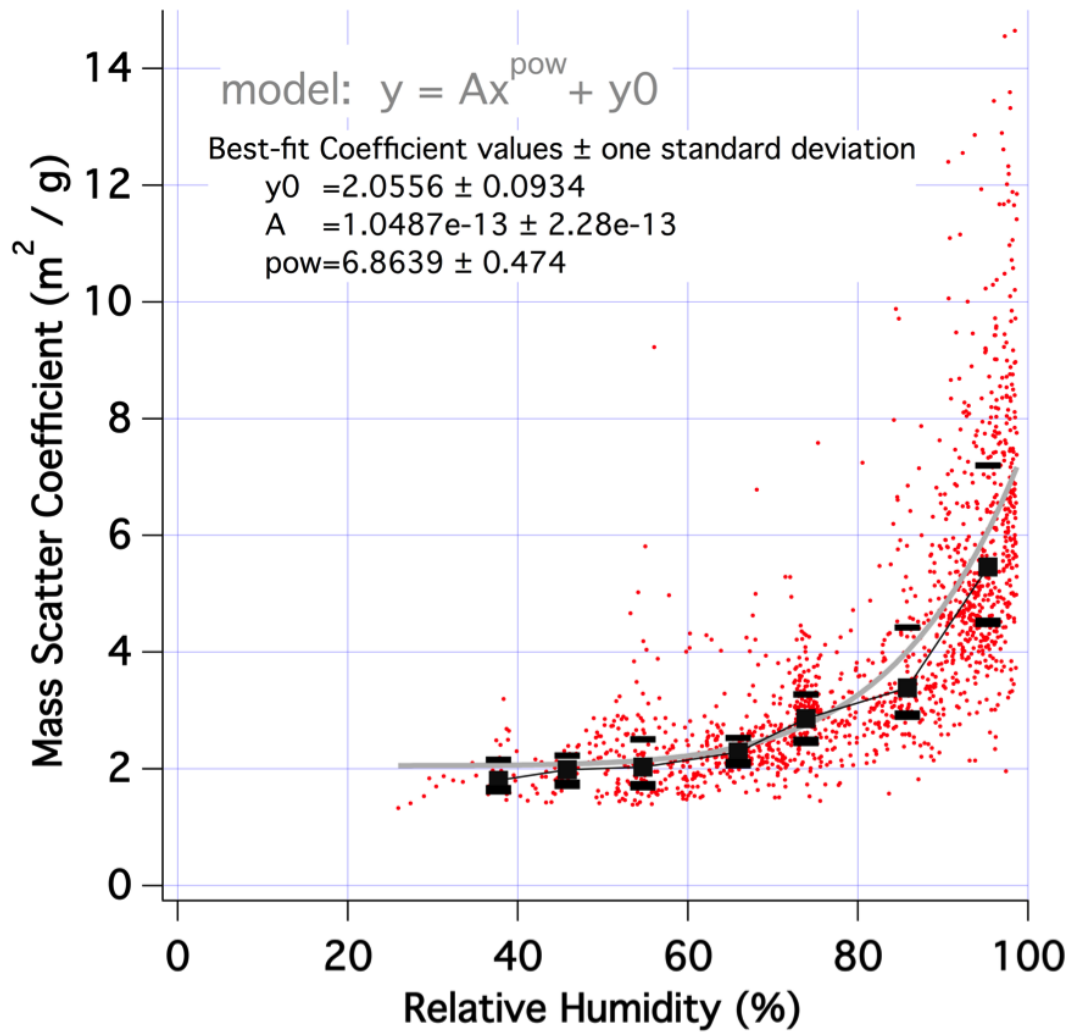


Figure 4.5 Plot of observed mass scattering coefficient vs. relative humidity for aerosol sampled in Houston, TX during 19–24 July 2013. On average, scatter increases approx. 3-fold at high RH. The grey trace illustrates a best-fit to the power law relationship indicated. The black points represent the medians and 25–75th % tiles of measurements for data sorted into 10 % wide RH bins.

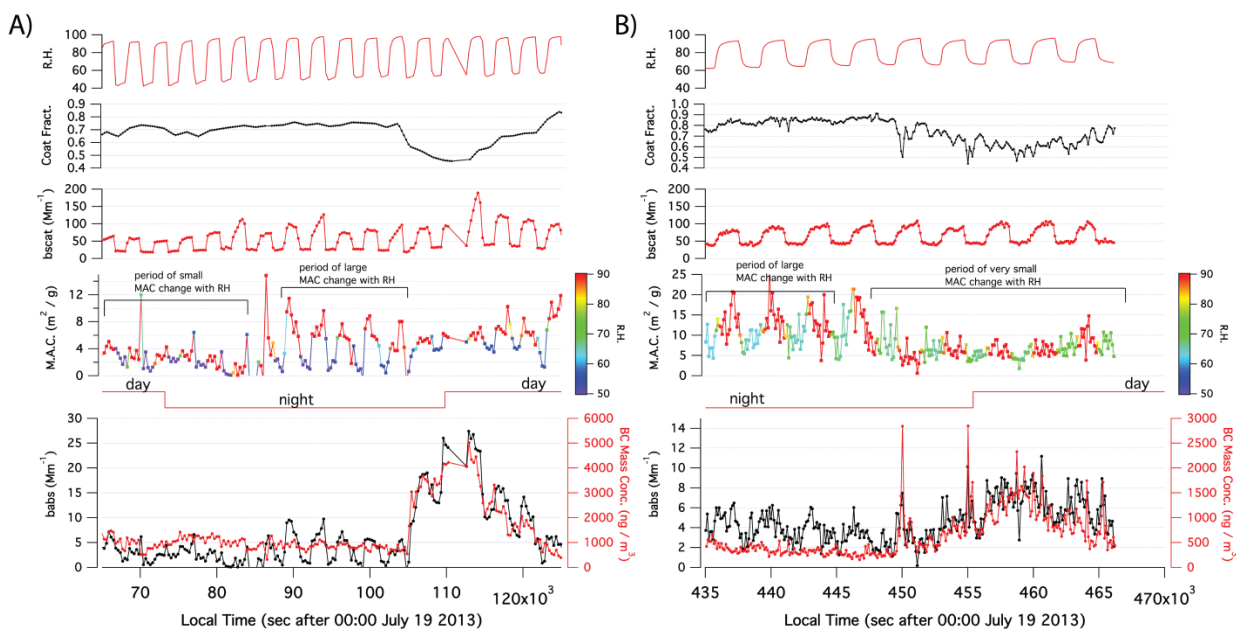


Figure 4.6 Data collected during 19–24 July 2013 at Houston TX that exhibit rapid changes in observed absorption enhancement due to RH. In (A), the initial 20 000 s exhibited small enhancement of MAC during periods of high RH – despite a large BC coat fraction. However, between approx. 85–105 ks a very abrupt change in behavior was noted. Similar changes are observed in 6B at approx. 447 ks into the sampling period. In 4b the period of abrupt change corresponds with a drop in BC coat fraction. However, such a large drop in coat fraction was not observed in (A). Results suggest the MAC of atmospheric soot and the enhancement at high RH is variable, and chemical composition of coatings may play significant role in the absorption enhancement process.

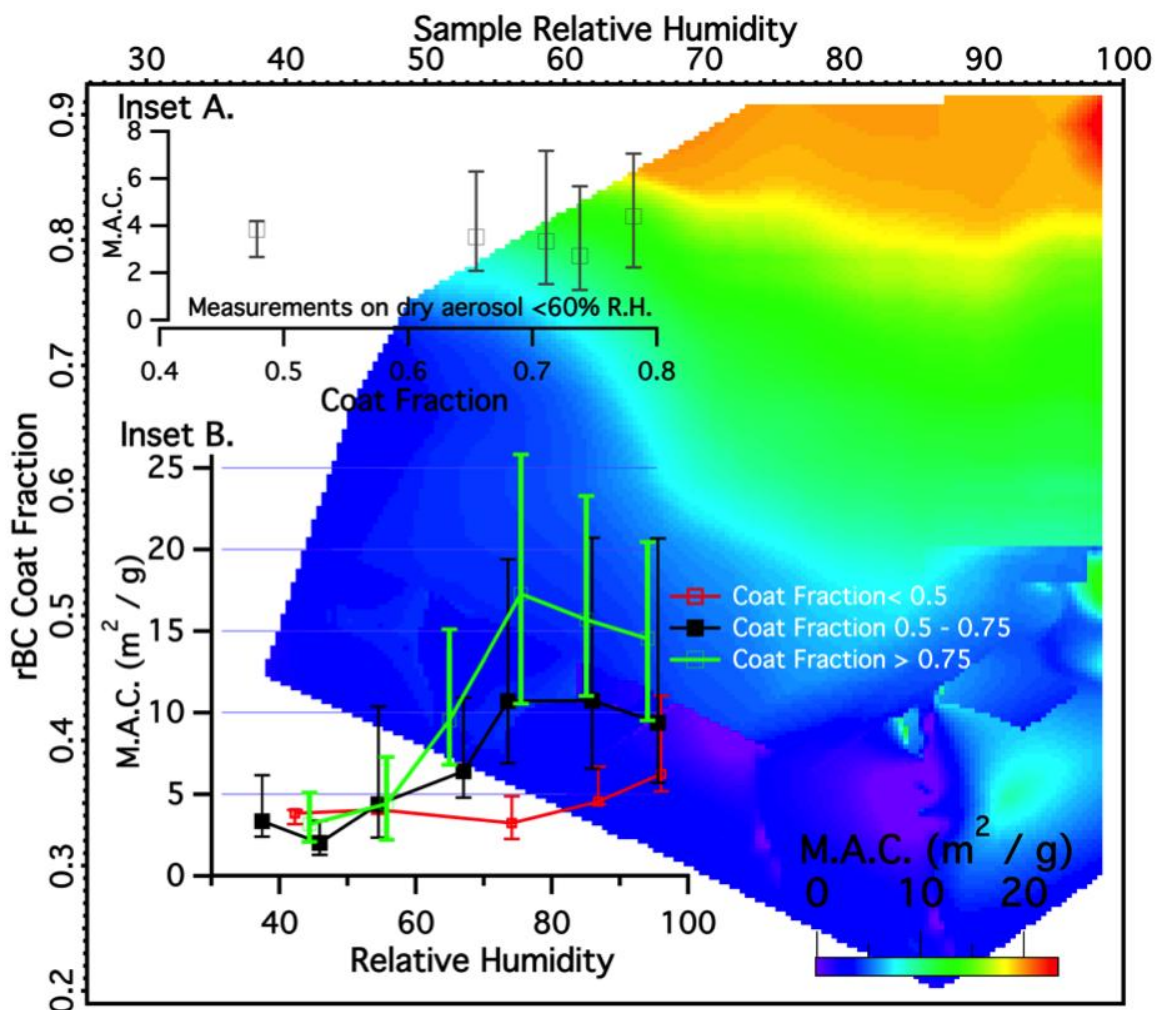


Figure 4.7 Observed soot MAC at $\lambda = 532 \text{ nm}$ vs. RH and coating state for all data. The square data points in the plots represent medians of pooled points and error bars are the quartiles. Inset A plots observed M.A.C. values vs. coating state for dried aerosol ($\text{RH} < 60\%$). A slight increase in median from 3.8–4.4 m^2g^{-1} was observed as coating fraction increased. Inset B illustrates the dramatic increase in MAC when RH was $> 60\%$. The increase in M.A.C. was largest when the rBC coating fraction was high, suggesting additional coating materials increase hygroscopicity and lead to enhanced absorption by BC. Image plot was median filtered at 60 pixels. An uncertainty analysis is presented in Appendix C Figure C.4

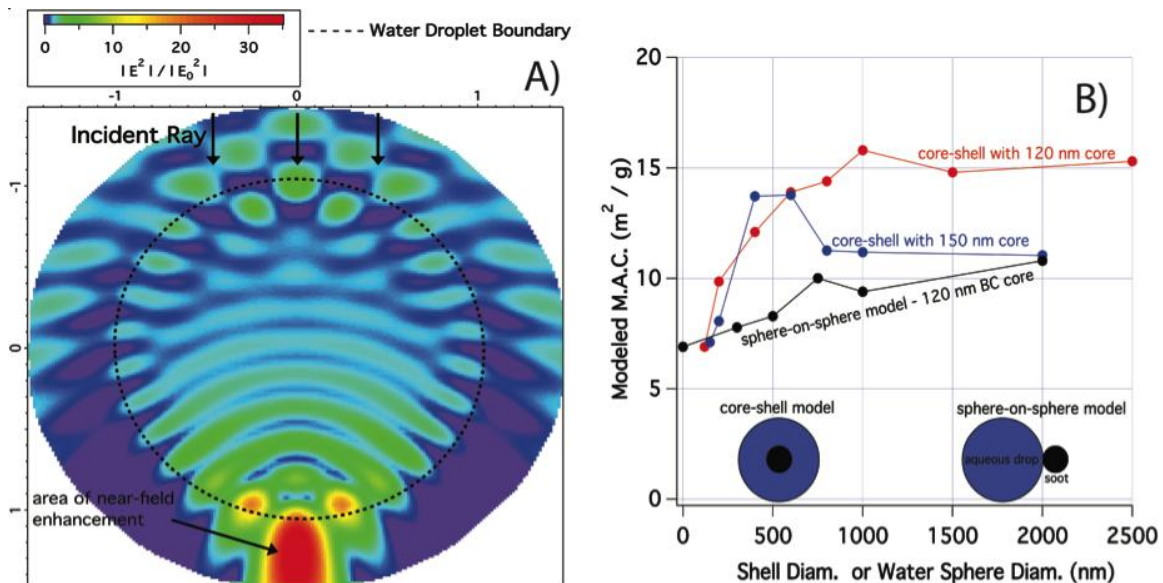


Figure 4.8 (A) Modeled electric field within and near a 2 micron water droplet. The dashed line is the droplets boundary and x, y-axis are in micrometers. As observed, field enhancements are possible both within and immediately outside of the droplet. (B) Plot of modeled soot MAC vs. the shell diameter or water sphere diameter for the core-shell and sphere-on-sphere models. For the sphere-on-sphere model the BC core was always 120 nm. While the sphere-on-sphere model did produce an absorption enhancement, MAC values of $15 m^2 g^{-1}$ were only possible for the core-shell model. Orientation averaging was employed for the sphere-on-sphere case.

CHAPTER V

CONCLUSION AND FUTURE WORK

Organic aerosol and black carbon are main component of aerosol in the atmosphere, which affect both climate and health. Therefore analytical methods have been developed in this dissertation to characterize both of them.

Unlike the well-constrained processes which result in formation of nitrate or sulfate aerosol, the oxidation of volatile organics in the atmosphere can lead to thousands of stale compounds in the aerosol phase. Development of a tractable framework to consider the chemical and physical evolution of the organic aerosol is crucial for modeling its effect on global climate. Therefore a 3-dimensional coordinate system, defined by molecular descriptors of molecular weight, heteroatom mass, and double bond equivalents (D.B.E.) was created. In this approach, each compound has a corresponding coordinate in the 3D space, which contains all information, such as the mass, physical and chemical properties. Based on reactions, routes can be written for the chemical out of the coordinate and track its movement (e.g. evolution process). Therefore, the reaction trajectories, physical behavior and chemical reactivity can be predicted. This approach acts as the air quality model, which yields important insight into all classes of analytes. On the other hand, both the lab generated secondary organic aerosol and ambient aerosol tend to occupy the similar region in the 3D space, which is the result of the reaction evolution. Future work of this approach can aim to develop an analytical method to populate a 2D space built on volatility and polarity of organic aerosol, so that aerosol behaviors can be described. The volatility will be assessed by gas chromatography (GC), while the polarity can be assessed through multi-solvent extraction.

To better understand the absorption behavior of black carbon, a method that coupling the aerosol albedometer with laser-induced incandescence (LII) was developed to direct measure mass absorption cross section (M.A.C.) with 1 min time resolution. The 532 nm beam laser was used to perform cavity ring-down spectroscopy (CRDS), with simultaneous measurements of scattering coefficient made through use of a reciprocal sphere nephelometer. The 1064 nm beam was selected and directed into a second

integrating sphere and used for LII of light-absorbing kerosene lamp soot. This method detected increase in M.A.C. values as well as the optical properties when lab-generated soot was coated with glycerol, ammonium sulfate and ammonium nitrate, indicating an enhanced light absorption. In addition, the M.A.C. value doubled at high relative humidity (RH) condition when soot was coated with other materials. However, the fresh soot exhibited no increase in M.A.C. at high RH. Therefore in this work, we believe the coating type and relative humidity are very important parameters to affect the light absorption efficiency of black carbon. Future direction of this work can aim to try other coating materials, and compare their light absorption effect under different humidity.

Besides the lab – generate soot, the ambient aerosol is also worth to analyze. In the last project, the hygroscopic growth of aerosol particles sampled at Houston, TX was measured. The relative humidity was controlled by a 3-way electronic valve, and cycled between dry and wet condition. In addition, aerosol albedometer was used to measure the optical properties, while the single particle soot photometer (SP2) was utilized to measure the BC mass concentration and mixing state of particle. Measurement showed that this hygroscopic growth resulted in an enhancement in both scattering and absorption. The light absorption increased roughly 3-4 fold at high ambient RH for coated soot particle, and high coating fraction particles enhanced the light absorption the most. However, for dried aerosol coating particles, almost no M.A.C increase was observed. Furthermore, the chemical composition of the coating and source of black carbon also play important roles in constraining MAC enhancement at high humidity. Future work can aim to measure the light absorption enhancement as a function of relative humidity in different locations and then compare the results. Evidences show the composition of coatings, as well as the sources of black carbon is differed by locations, and the magnitude of increase in M.A.C. also varied in time and location. Moreover, a “correct” model, core-shell model or sphere-on-sphere model, needs to be point out in order to better illustrate the enhancement of light absorption for coated aerosol sample.

In addition, we can study the way that immerse black carbon into aqueous droplets in the future. According to the Houston results, the core-shell model would

better illustrate the M.A.C. enhancement under high humidity, leading to the core-shell type lensing effect. However, black carbon will tend to surround at the surface of water droplet, which reduce the light absorption ability. Therefore coming up a way to immerse the black carbon into the droplet becomes essential. It is known that black carbon is hydrophobic, so one method to make it hydrophilic is to modify its surface. Thus many surfactants can be used in order to realize this idea, such as palmitic acid, sodium lauryl sulfate and even detergents. These surfactants will lower the surface tension between water droplet and black carbon, which help the immersion process.

Moreover, we can also study the property of black carbon when it is coated with two or more non-absorbing materials, or even organic materials. Previous studies show the deliquescence point of mixed inorganic material, such as ammonium sulfate and ammonium nitrate, is different from that of single material; therefore the water uptake property of black carbon will be affected, causing increase or decrease of light absorption efficiency. On the other hand, complex reactions would occur in the atmosphere, and produce tons of secondary organic aerosols, as this occurs, these organic materials will also coat on the black carbon, leading to the change of optical properties. All these factors will result in the variation of light absorption efficiency.

Furthermore, the optical properties of aerosol will also differ from burning sources, so we can test different types of burning aerosols, such as the biomass burning sample, cooking aerosol, aircraft aerosol and aerosols burned from other transportations. After collecting these samples, it is possible for us to study the optical properties, water uptake ability, size distribution and light absorbing efficiency in order to better master the overall information about these aerosol behaviors.

APPENDICES

A. SUPPLEMENTARY INFORMATION FOR CHAPTER II

Table A.1 Best-fit parameters for prediction of vapor pressure.

Compound Class	Intercept	m_{M.W.}	m_{Heteromass}	m_{D.B.E.}	Fit R²
All compounds	1.987	-0.01775	-0.0135	-0.3482	0.68
CH	4.17	-0.0233	0	-0.32959	0.96
CHO	4.74	-0.01867	-0.0805	-0.1682	0.72
CHS	2.70	-0.0208	0.0046	-0.3209	0.70
CHSO	4.04	-0.0128	-0.0496	-0.4151	0.71
CHN	3.03	-0.02785	-0.04257	-0.12572	0.71
CHNO	1.71	-0.01611	-0.05108	-0.06425	0.40

Figure A.1 and A.2 below report performance characteristics of the 3 parameter fit. Figure A.1 shows comparisons between the QSPR predicted value and the 3 parameter fit. The histograms of Figure A.2 represent the frequency distributions of differences between QSPR vapor pressure and the vapor pressure predicted by the 3 parameter model.

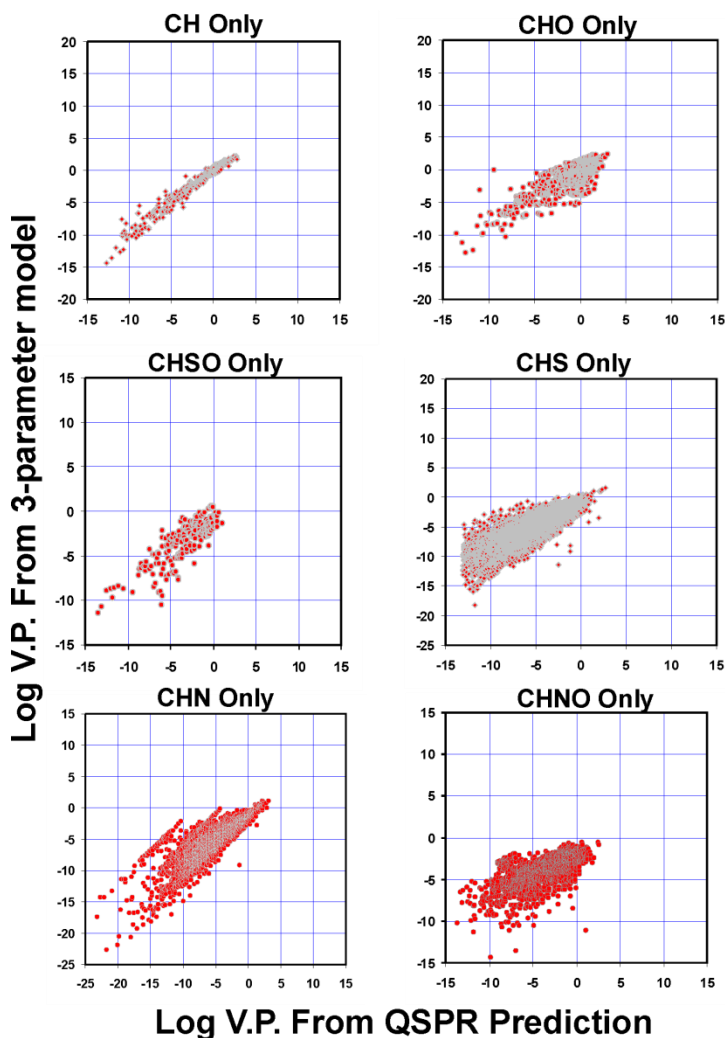


Figure A.1 Plots of the vapor pressure predicted by the 3 parameter fit vs. the QSPR predicted values for the training set data. The 3 parameter fit can handle hydrocarbons easily, but when heteroatoms are present, the quality of the fit degrades. This may be due to structural differences in the compounds that cannot be accounted for by the three parameter model.

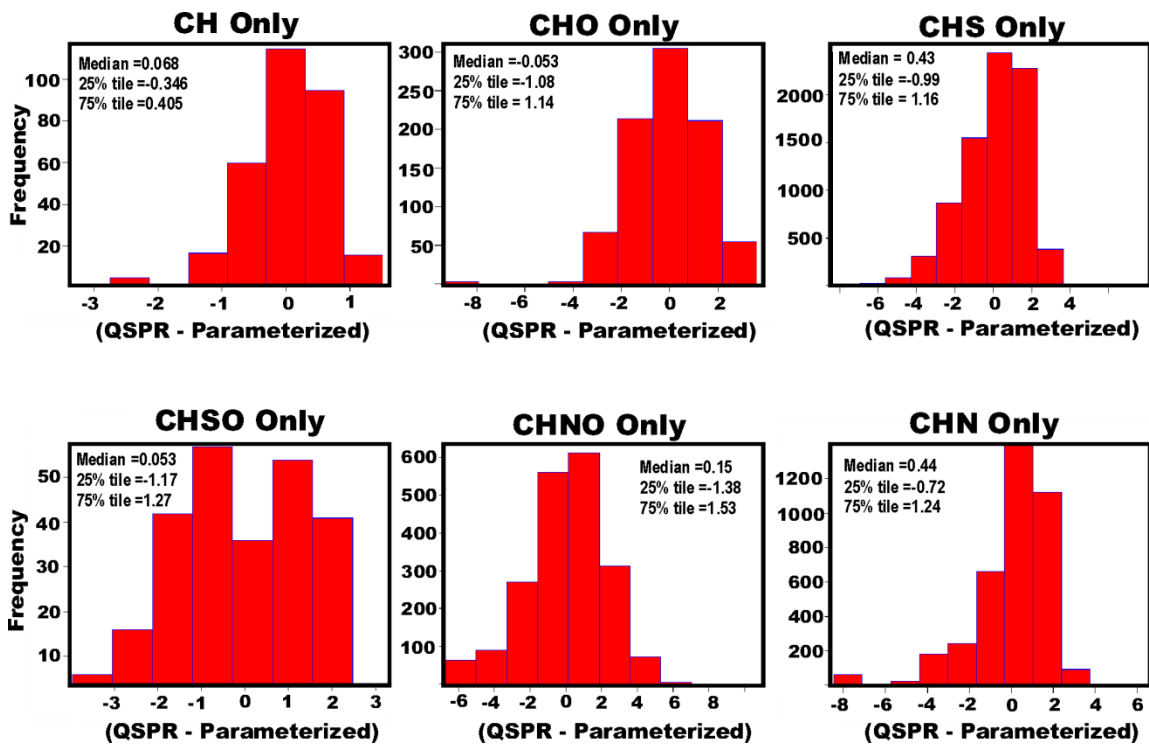


Figure A.2 Histograms of the difference between QSPR predicted and parameterized prediction of the logarithm of vapor pressure for the various subsets of data. Medians are often near zero and the central 50% of data often lies between -1 and 1 log unit.

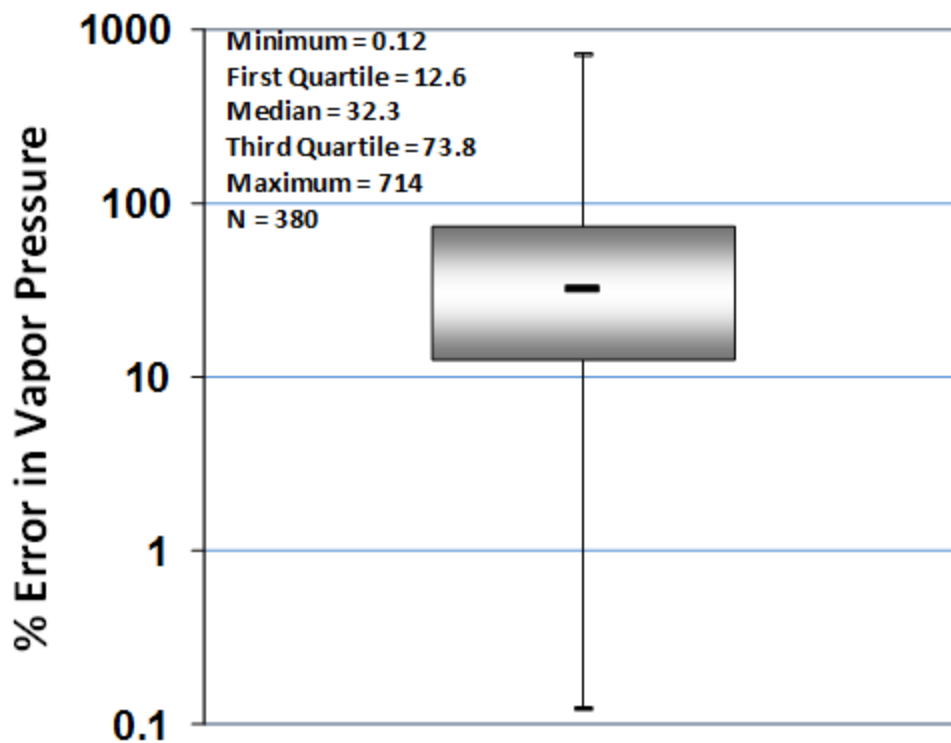


Figure A.3 Box plot of results for error in vapor pressure predictions for 380 test compounds containing C,H,and O. The median error was 32.3%. The grey box represents the 25 – 75% tile and the error bars the min. – max. range. To evaluate the accuracy of the parameterization based on M.W., heteroatom mass, and DBE we used equation (10) to predict vapor pressures for a test set of 380 compounds containing C, H, and O. The *Yaw's Handbook of Vapor Pressure*²⁰⁶ was used to determine accepted values for vapor pressures for the test compounds. We then computed % *Error* between the 3 parameter prediction and the handbook value for all compounds.

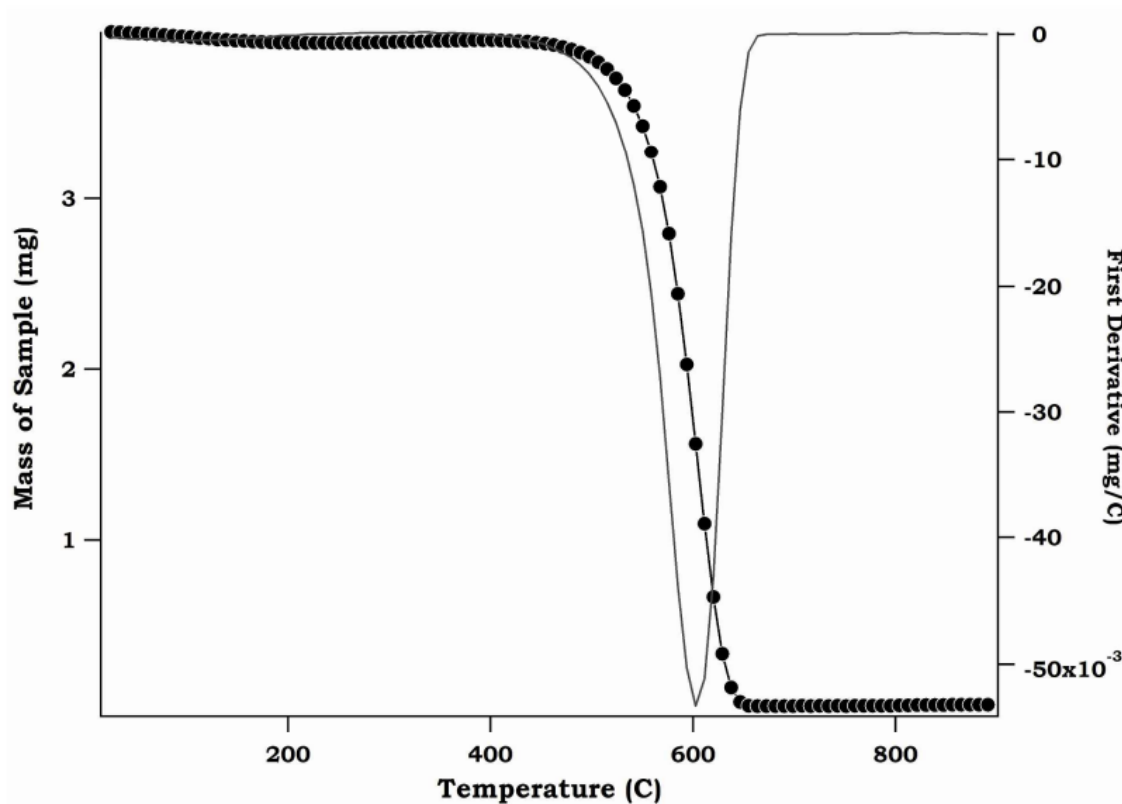
B. SUPPLEMENTARY FIGURES FOR CHAPTER III

Figure B.1 Thermogravimetric analysis (TGA) of fresh kerosene ns-soot used in this study. The TGA purge gas was air for this experiment. As observed, significant mass loss did not occur until approx. 550 °C. This suggests a large mass of volatile organic molecules was not present in the fresh kerosene ns-soot sample. Therefore, optical results are representative of fresh kerosene ns-soot.

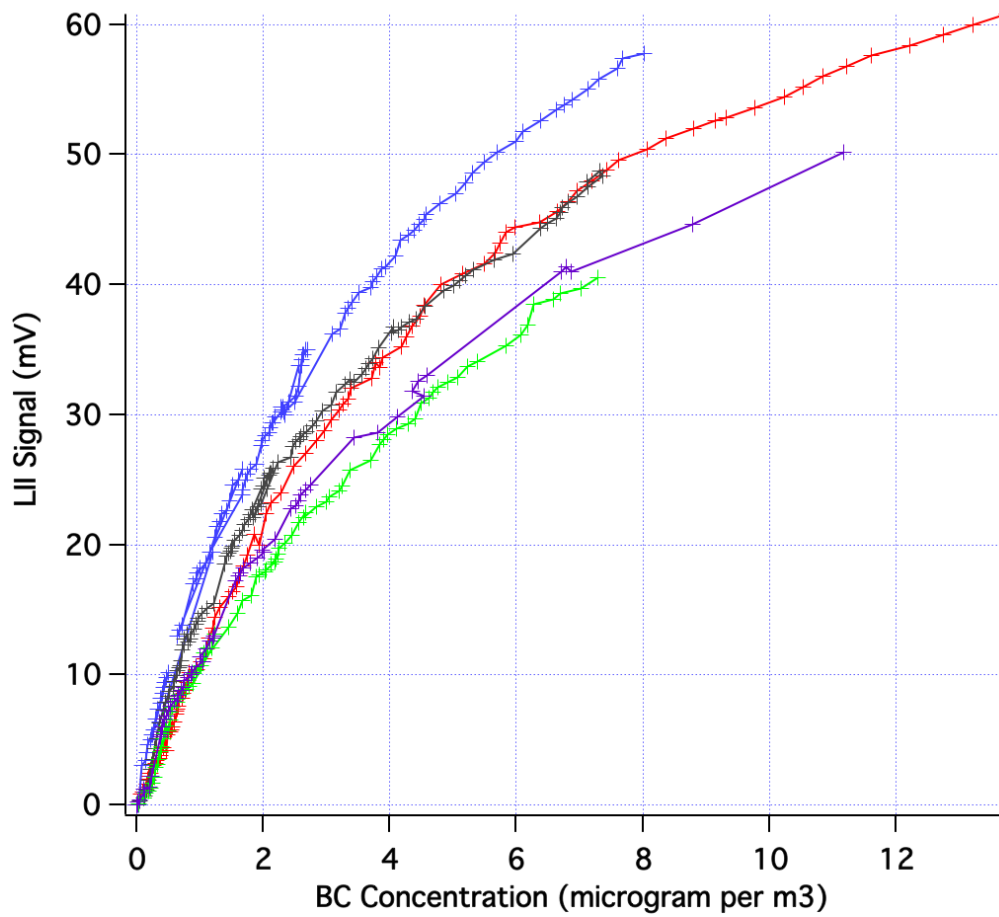
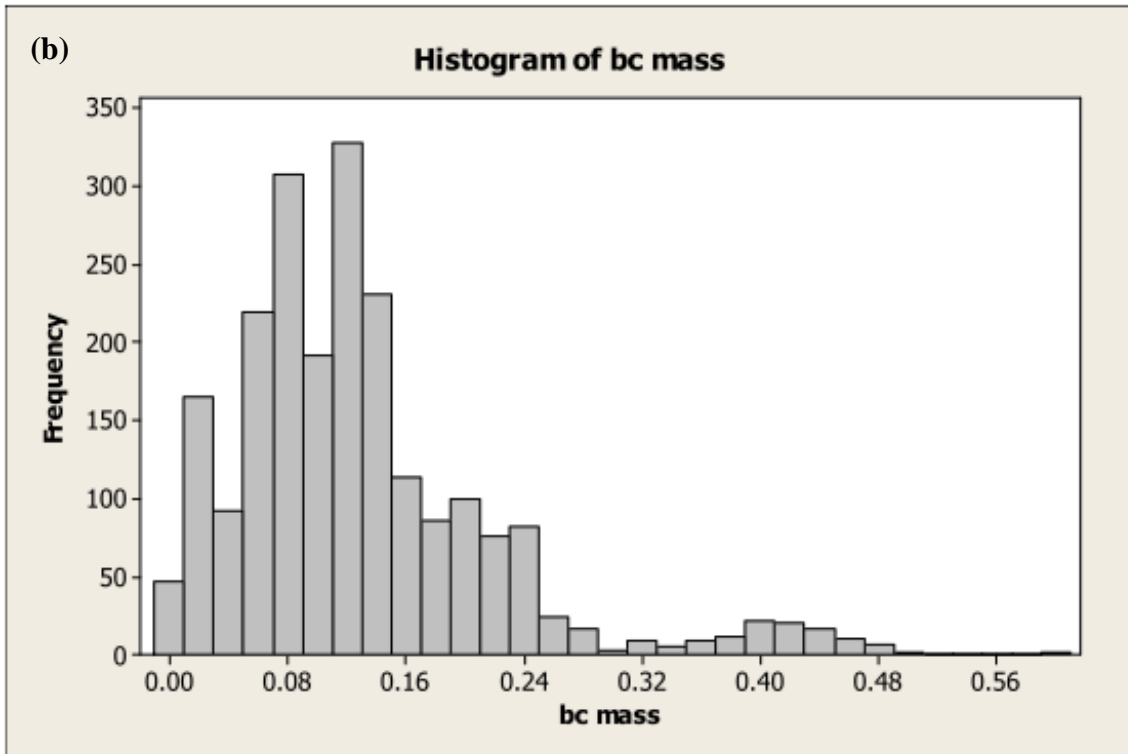
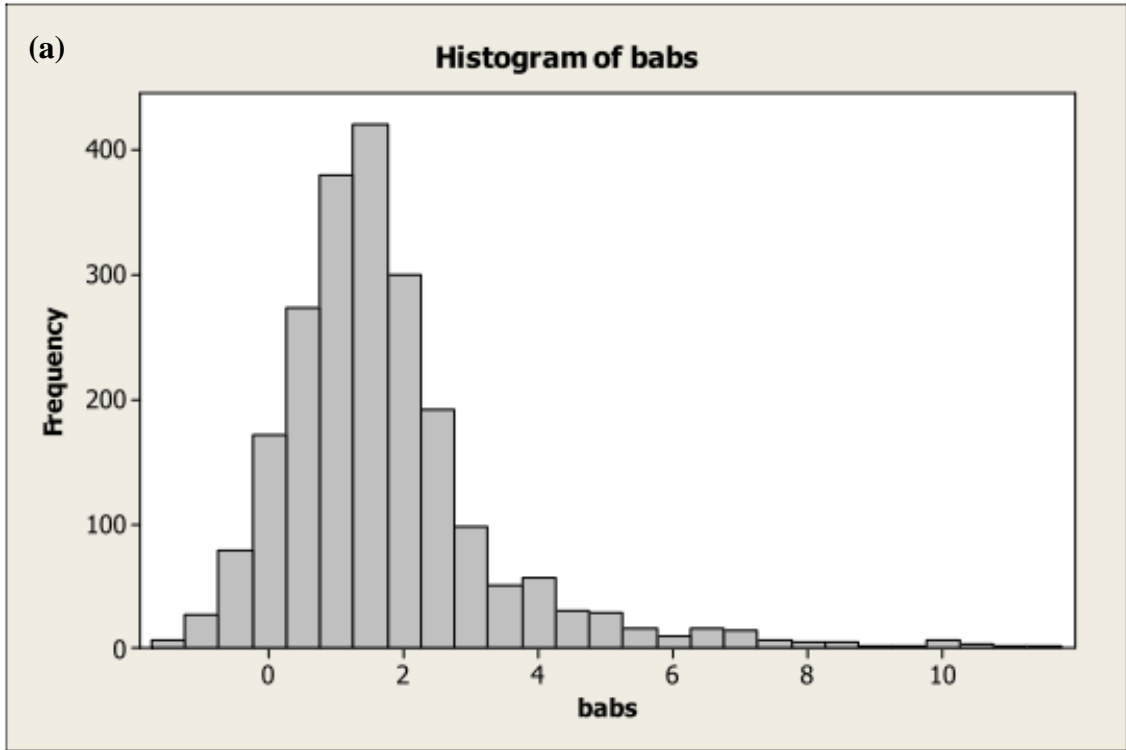
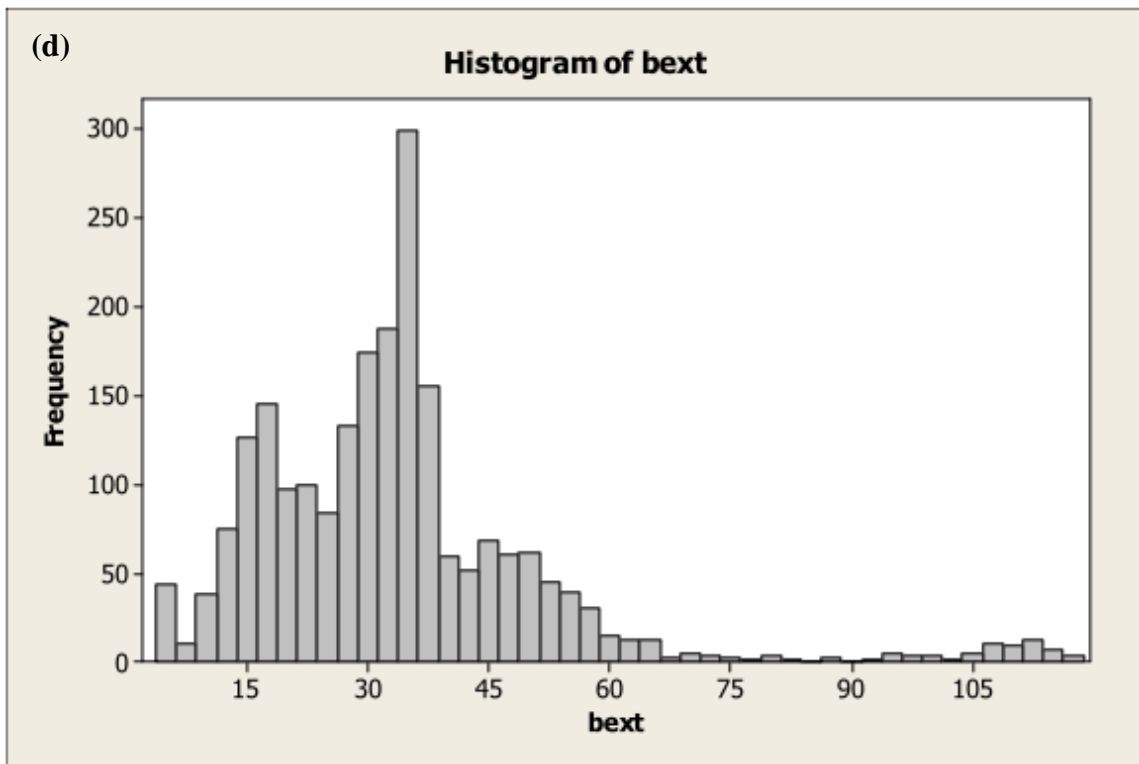
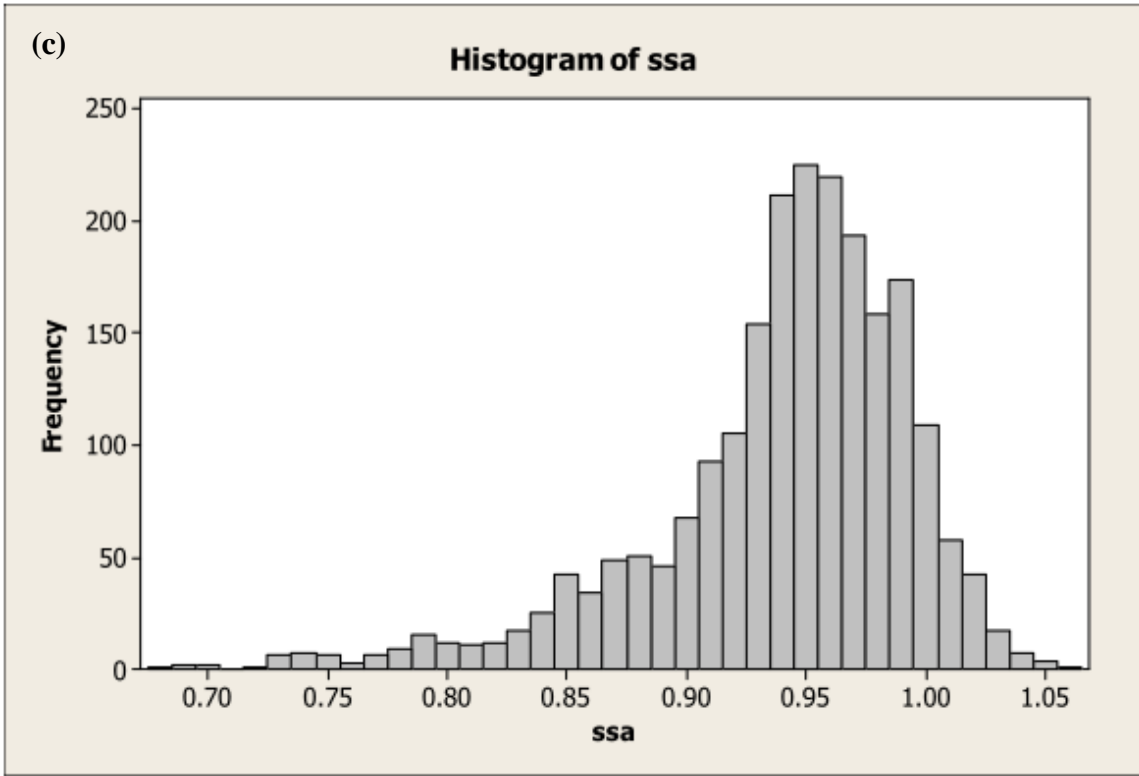


Figure B.2 Observed LII responses vs. indicated BC concentration as measured using the PSAP. Here, BC and ns-soot are synonyms. The different data series were collected at different times / during different calibrations. Fluctuations in laser power or optical alignment is not believed to account for the differences observed. Rather, it is believed slight differences in the ns-soot samples leads to the variability. Laser fluence was $160 \text{ mJ} / \text{cm}^2$.





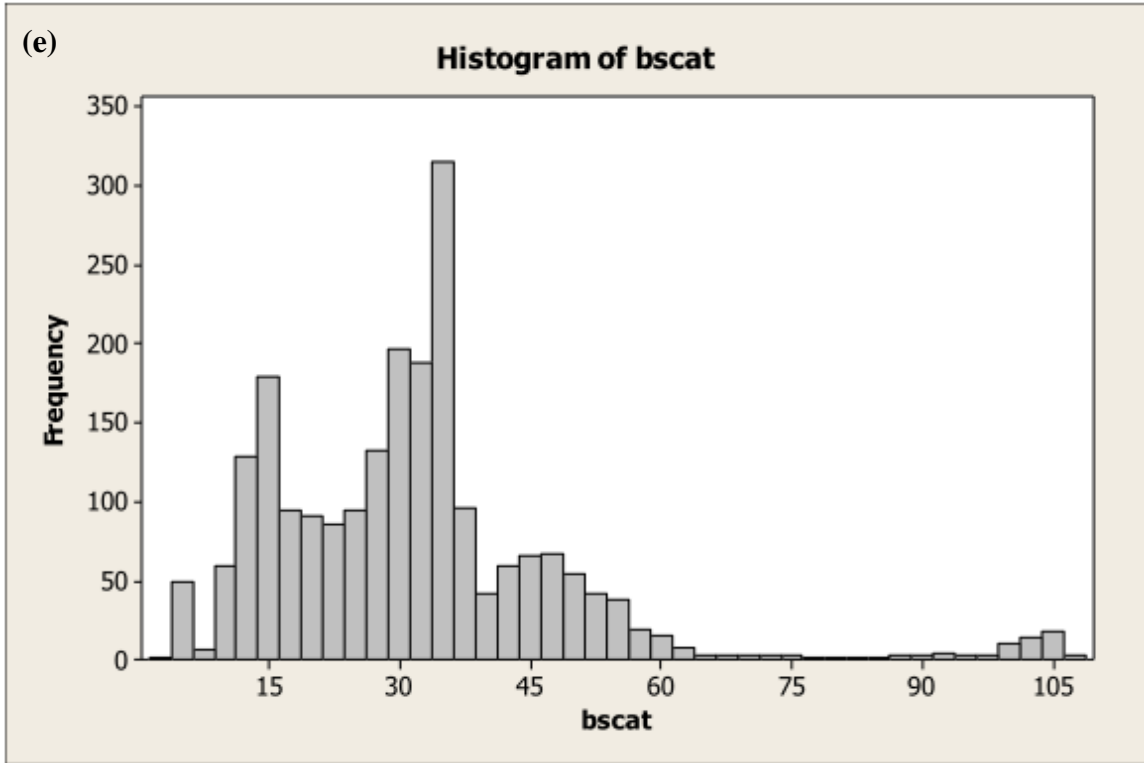


Figure B.3 (a) Histogram of observed aerosol absorption coefficient (b_{abs} , Mm^{-1}) during the ambient monitoring at Lubbock, TX during May 2013. Data set mean was 1.7 Mm^{-1} . (b) Histogram of observed BC mass concentrations ($\mu\text{g}/\text{m}^3$) during the ambient monitoring at Lubbock, TX during May 2013. Data set mean was $0.13 \mu\text{g}/\text{m}^3$. (c) Histogram of observed SSA during the ambient monitoring at Lubbock, TX during May 2013. Data set mean was 0.973. Data was not collected during dust events that are common in our region. (d) Histogram of observed aerosol extinction coefficient (b_{ext} , Mm^{-1}) during the ambient monitoring at Lubbock, TX during May 2013. Data set mean was 32.3 Mm^{-1} . (e) Histogram of observed aerosol scatter coefficient (b_{scat} , Mm^{-1}) during the ambient monitoring at Lubbock, TX during May 2013. Data set mean was 31.7 Mm^{-1} .

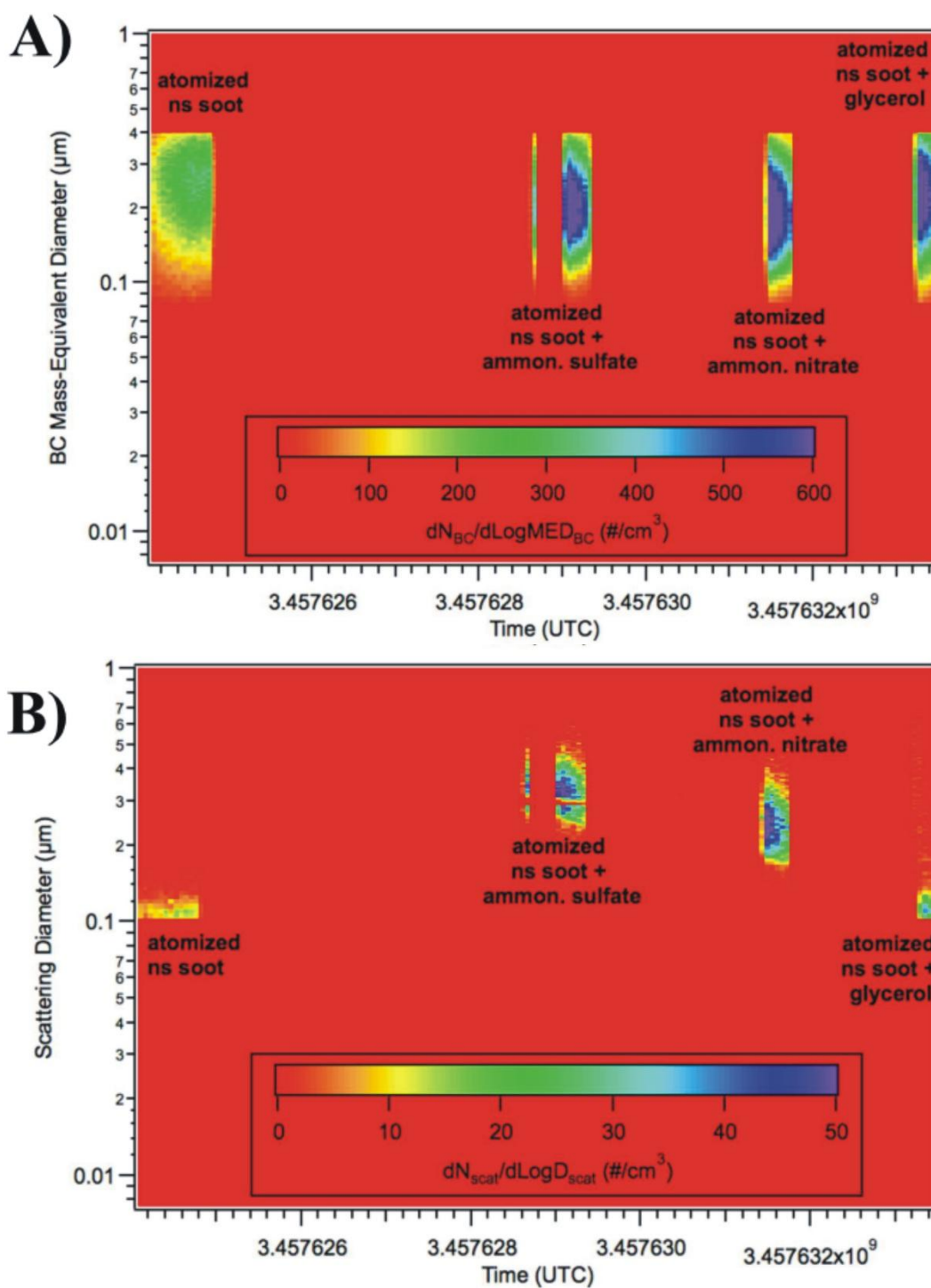


Figure B.4 (A) Indicated size distribution of BC cores for atomized kerosene soot suspensions used in this study. (B) Size distribution of scattering particles for the same atomized kerosene soot suspensions. Measurements conducted using Droplet Measurement Technology SP-2 as calibrated against size-selected fullerene soot.

C. SUPPLEMENTARY FIGURES FOR CHAPTER IV

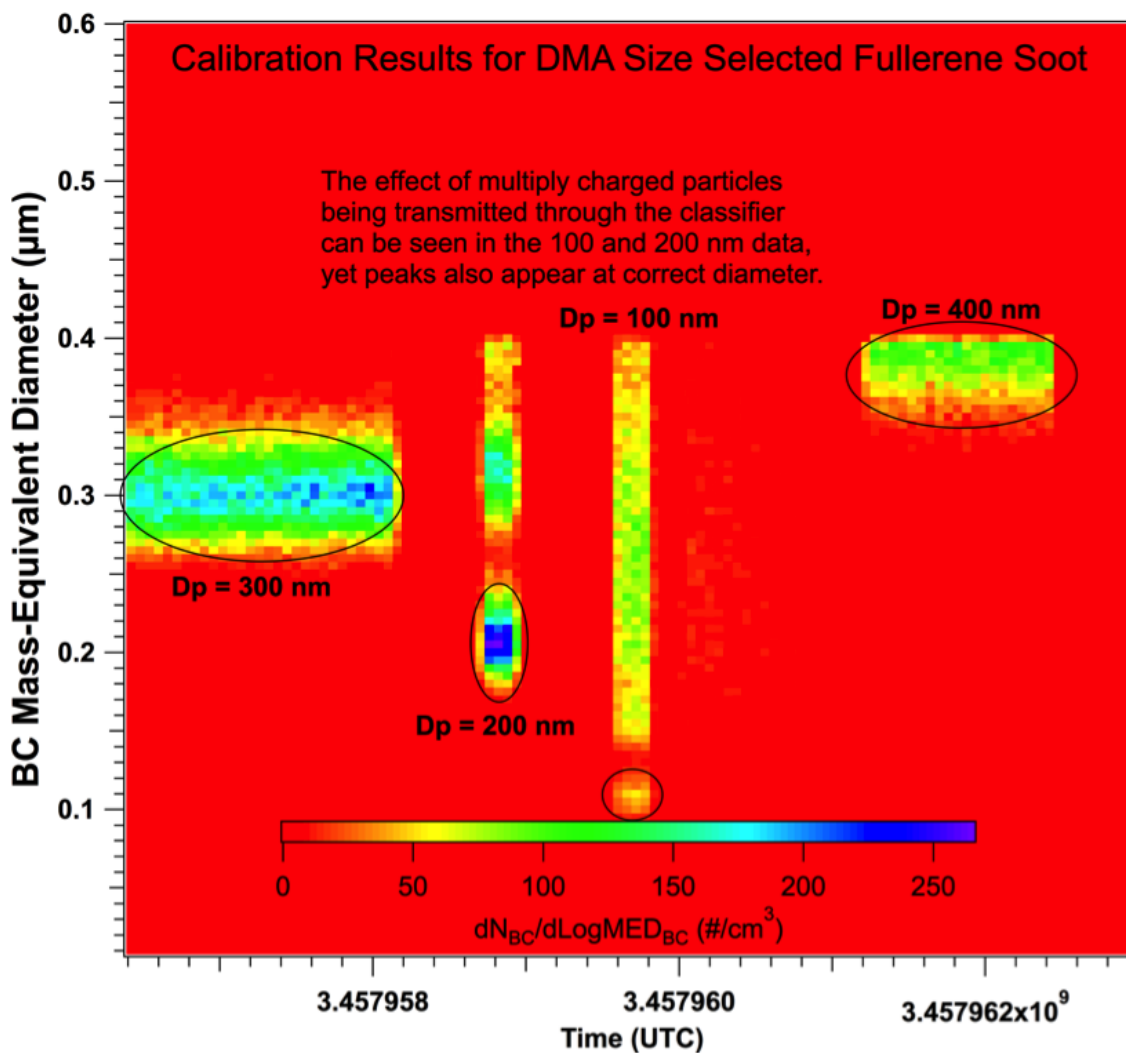


Figure C.1 Laboratory calibration of SP2 after the field campaign. Fullerene soot was atomized from an aqueous suspension and size selected to $D_p = 100, 200, 300$ or 400 nm with an electrostatic classifier. After calibration, the SP2 produced BC mass equivalent diameters identical to those expected and this calibration was applied to the Houston data. The effects of multiply charged particles being transmitted through the classifier are seen for the $D_p = 100 \text{ nm}$ and $D_p = 200 \text{ nm}$ cases, yet a peak in the distribution is still clearly visible at the desired diameter.

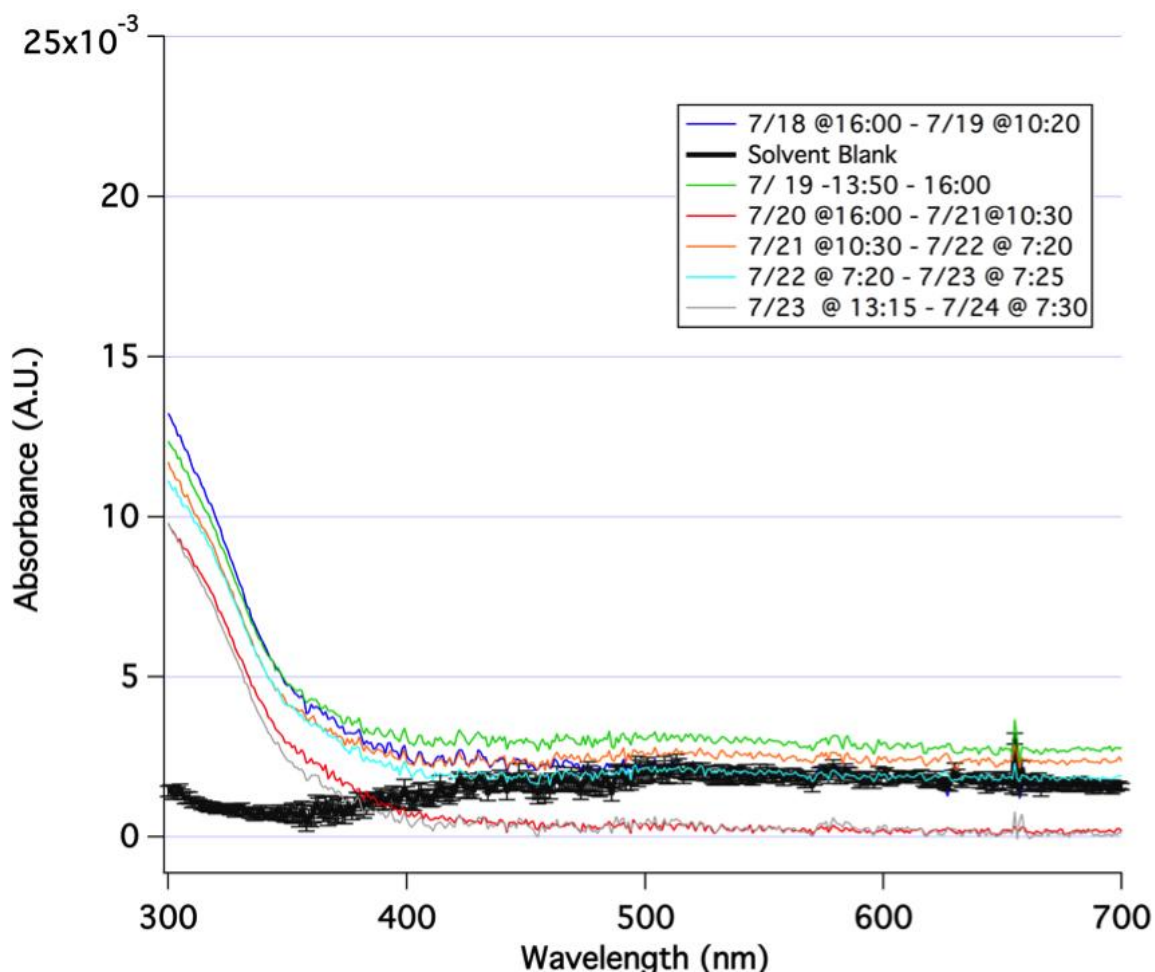


Figure C.2 Evaluation of possible “brown carbon” interference. UV-VIS Spectra of filter extracts collected from Houston, TX and a spectroscopic blank (black). Particles deposited onto a filter were extracted into 1.5 mL of 20% methanol: 80% water (v/v). Extracts were filtered through a 0.2 micron syringe filter prior to analysis. For reference, 4 mAU corresponds to a 1% change in transmittance. The particle samples exhibited increased absorbance in the 300 – 400 nm spectral window, but the lack of significant visible absorption suggests brown carbon did not play a significant role in absorbing light for the samples considered. Times indicated are local

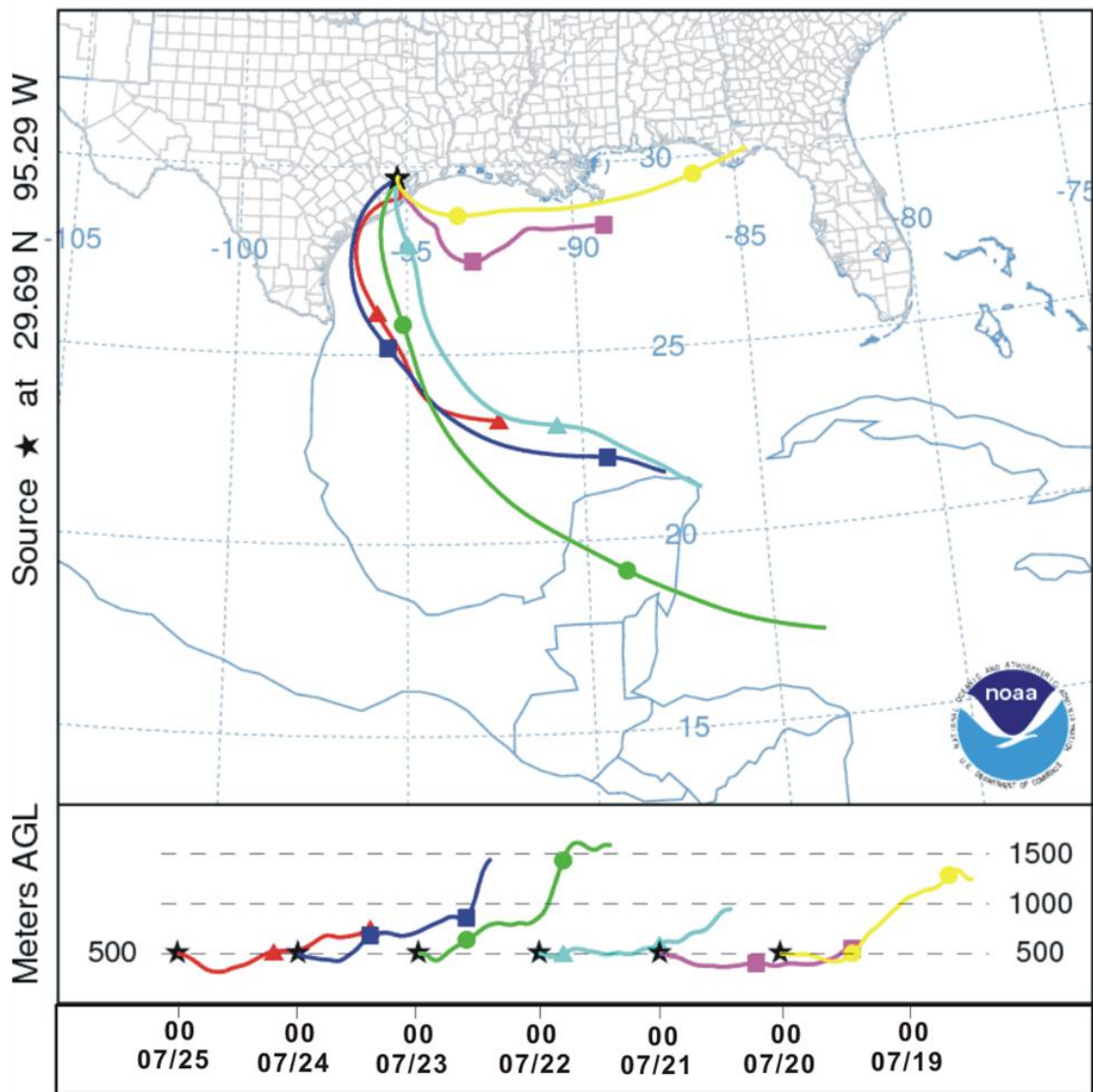


Figure C.3 NOAA HYSPLIT Back Trajectory Analysis during the sampling period. The authors gratefully acknowledge the NOAA Air Resources Laboratory (ARL) for the provision of the HYSPLIT transport and dispersion model and/or READY website (<http://www.ready.noaa.gov>) used in this publication.

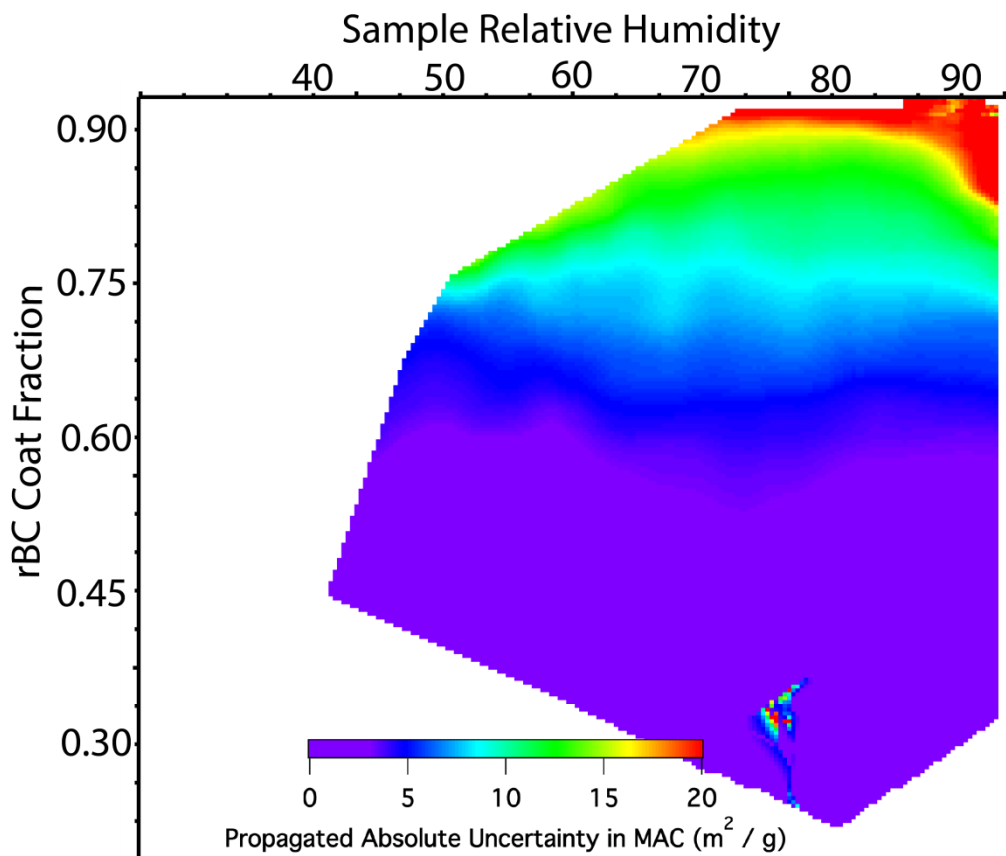


Figure C.4 Uncertainty analysis that accompanies Figure 4.7 of this work. Figure C.4 presents propagated absolute uncertainty in MAC vs. coat fraction and RH. Because higher BC coat fractions were often observed when rBC mass concentration and b_{abs} were very low, the propagated absolute uncertainty in MAC is not constant. Highest absolute uncertainty was present at high rBC coat fractions, where largest MAC enhancement was also observed. For this analysis, an absolute uncertainty of $b_{\text{abs}} = 2 \text{ Mm}^{-1}$ and $[\text{BC mass}] = 50 \text{ ng} / \text{m}^3$ were used. Uncertainty was propagated through the computation of MAC using the sum of squares of relative uncertainty approach.

REFERENCE

1. Lee, S. H.; Allen, H. C., *Anal Chem* **2012**, *84* (3), 1196-1201.
2. Pósfai, M.; Buseck, P. R., *Annual Review of Earth and Planetary Sciences* **2010**, *38* (1), 17-43.
3. IPCC, *Climate Change 2007: The Physical Science Basis* 2007.
4. Andreae, M. O.; Rosenfeld, D.; Artaxo, P.; Costa, A. A.; Frank, G. P.; Longo, K. M.; Silva-Dias, M. A. F., *Science* **2004**, *303* (5662), 1337-1342.
5. ZHANG Ren-Jian, H. K.-F., SHEN Zhen-Xing, *Atmospheric and Oceanic Science Letters* **2012**, *5* (2), 156-161.
6. Gauderman, W. J.; Avol, E.; Gilliland, F.; Vora, H.; Thomas, D.; Berhane, K.; McConnell, R.; Kuenzli, N.; Lurmann, F.; Rappaport, E.; Margolis, H.; Bates, D.; Peters, J., *N Engl J Med* **2004**, *351* (11), 1057-1067.
7. Pope, C. A., 3rd; Burnett, R. T.; Thurston, G. D.; Thun, M. J.; Calle, E. E.; Krewski, D.; Godleski, J. J., *Circulation* **2004**, *109* (1), 71-77.
8. Ostro, B.; Roth, L.; Malig, B.; Marty, M., *Environmental Health Perspectives* **2009**, *117* (3), 475-480.
9. Darrow, L. A.; Klein, M.; Strickland, M. J.; Mulholland, J. A.; Tolbert, P. E., *Environ Health Perspect* **2011**, *119* (5), 731-737.
10. Jay Turner, I. C., *Environmental Chemistry of Aerosols* 2008, 1-29.
11. Spracklen, D. V.; Jimenez, J. L.; Carslaw, K. S.; Worsnop, D. R.; Evans, M. J.; Mann, G. W.; Zhang, Q.; Canagaratna, M. R.; Allan, J.; Coe, H.; McFiggans, G.; Rap, A.; Forster, P., *Atmospheric Chemistry and Physics* **2011**, *11* (23), 12109-12136.
12. Jacobson, M. C.; Hansson, H. C.; Noone, K. J.; Charlson, R. J., *Reviews of Geophysics* **2000**, *38* (2), 267-294.
13. Warnke, T. H. a. J., Organic Aerosols. In *Volatile organic compounds in the atmosphere*, 1st ed.; Koppmann, R., Ed. Blackwell Pub.: Oxford ; Ames, Iowa, **2007**; pp xii, 500 p.

14. Jimenez, J. L.; Canagaratna, M. R.; Donahue, N. M.; Prevot, A. S. H.; Zhang, Q.; Kroll, J. H.; DeCarlo, P. F.; Allan, J. D.; Coe, H.; Ng, N. L.; Aiken, A. C.; Docherty, K. S.; Ulbrich, I. M.; Grieshop, A. P.; Robinson, A. L.; Duplissy, J.; Smith, J. D.; Wilson, K. R.; Lanz, V. A.; Hueglin, C.; Sun, Y. L.; Tian, J.; Laaksonen, A.; Raatikainen, T.; Rautiainen, J.; Vaattovaara, P.; Ehn, M.; Kulmala, M.; Tomlinson, J. M.; Collins, D. R.; Cubison, M. J.; Dunlea, E. J.; Huffman, J. A.; Onasch, T. B.; Alfarra, M. R.; Williams, P. I.; Bower, K.; Kondo, Y.; Schneider, J.; Drewnick, F.; Borrmann, S.; Weimer, S.; Demerjian, K.; Salcedo, D.; Cottrell, L.; Griffin, R.; Takami, A.; Miyoshi, T.; Hatakeyama, S.; Shimono, A.; Sun, J. Y.; Zhang, Y. M.; Dzepina, K.; Kimmel, J. R.; Sueper, D.; Jayne, J. T.; Herndon, S. C.; Trimborn, A. M.; Williams, L. R.; Wood, E. C.; Middlebrook, A. M.; Kolb, C. E.; Baltensperger, U.; Worsnop, D. R., *Science* **2009**, *326* (5959), 1525-1529.
15. Koppmann, R.; ebrary Inc., *Volatile organic compounds in the atmosphere*. 1st ed.; Blackwell Pub.: Oxford ; Ames, Iowa, **2007**; pp. xii, 500 p.
<http://site.ebrary.com/lib/yale/Doc?id=10236699>.
16. Finlayson-Pitts, B. J.; Pitts, J. N., *Chemistry of the upper and lower atmosphere : theory, experiments and applications*. Academic Press: San Diego, Calif. ; London, **2000**; p xxii, 969 p.
17. Donahue, N. M.; Robinson, A. L.; Stanier, C. O.; Pandis, S. N., *Environ Sci Technol* **2006**, *40* (8), 2635-2643.
18. Shiraiwa, M.; Ammann, M.; Koop, T.; Poschl, U., *Proceedings of the National Academy of Sciences of the United States of America* **2011**, *108* (27), 11003-11008.
19. Canagaratna, M. R.; Jayne, J. T.; Jimenez, J. L.; Allan, J. D.; Alfarra, M. R.; Zhang, Q.; Onasch, T. B.; Drewnick, F.; Coe, H.; Middlebrook, A.; Delia, A.; Williams, L. R.; Trimborn, A. M.; Northway, M. J.; DeCarlo, P. F.; Kolb, C. E.; Davidovits, P.; Worsnop, D. R., *Mass Spectrometry Reviews* **2007**, *26* (2), 185-222.
20. Jimenez, J., *Aerosol mass spectrometry web page*.
21. Gross, D. S.; Galli, M. E.; Kalberer, M.; Prevot, A. S. H.; Dommen, J.; Alfarra, M. R.; Duplissy, J.; Gaeggeler, K.; Gascho, A.; Metzger, A.; Baltensperger, U., *Analytical Chemistry* **2006**, *78* (7), 2130-2137.
22. Pratt, K. A.; Prather, K. A., *Mass Spectrometry Reviews* **2012**, *31* (1), 1-16.
23. Pratt, K. A.; Prather, K. A., *Mass Spectrometry Reviews* **2012**, *31* (1), 17-48.
24. Jayne, J. T.; Leard, D. C.; Zhang, X. F.; Davidovits, P.; Smith, K. A.; Kolb, C. E.; Worsnop, D. R., *Aerosol Science and Technology* **2000**, *33* (1-2), 49-70.

25. Drewnick, F.; Hings, S. S.; DeCarlo, P.; Jayne, J. T.; Gonin, M.; Fuhrer, K.; Weimer, S.; Jimenez, J. L.; Demerjian, K. L.; Borrmann, S.; Worsnop, D. R., *Aerosol Science and Technology* **2005**, *39* (7), 637-658.
26. Kimmel, J. R.; Farmer, D. K.; Cubison, M. J.; Sueper, D.; Tanner, C.; Nemitz, E.; Worsnop, D. R.; Gonin, M.; Jimenez, J. L., *International Journal of Mass Spectrometry* **2011**, *303* (1), 15-26.
27. Huffman, J. A.; Jayne, J. T.; Drewnick, F.; Aiken, A. C.; Onasch, T.; Worsnop, D. R.; Jimenez, J. L., *Aerosol Science and Technology* **2005**, *39* (12), 1143-1163.
28. Salcedo, D.; Onasch, T. B.; Canagaratna, M. R.; Dzepina, K.; Huffman, J. A.; Jayne, J. T.; Worsnop, D. R.; Kolb, C. E.; Weimer, S.; Drewnick, F.; Allan, J. D.; Delia, A. E.; Jimenez, J. L., *Atmospheric Chemistry and Physics* **2007**, *7*, 549-556.
29. Zhang, Q.; Alfarra, M. R.; Worsnop, D. R.; Allan, J. D.; Coe, H.; Canagaratna, M. R.; Jimenez, J. L., *Environ Sci Technol* **2005**, *39* (13), 4938-4952.
30. Crosier, J.; Jimenez, J. L.; Allan, J. D.; Bower, K. N.; Williams, P. I.; Alfarra, M. R.; Canagaratna, M. R.; Jayne, J. T.; Worsnop, D. R.; Coe, H., *Aerosol Science and Technology* **2007**, *41* (9), 865-872.
31. Nash, D. G.; Baer, T.; Johnston, M. V., *International Journal of Mass Spectrometry* **2006**, *258* (1-3), 2-12.
32. Wozniak, A. S.; Bauer, J. E.; Sleighter, R. L.; Dickhut, R. M.; Hatcher, P. G., *Atmospheric Chemistry and Physics* **2008**, *8* (17), 5099-5111.
33. Stenson, A. C.; Landing, W. M.; Marshall, A. G.; Cooper, W. T., *Analytical Chemistry* **2002**, *74* (17), 4397-4409.
34. Smith, J. S.; Laskin, A.; Laskin, J., *Analytical Chemistry* **2009**, *81* (4), 1512-1521.
35. Laskin, A.; Smith, J. S.; Laskin, J., *Environ Sci Technol* **2009**, *43* (10), 3764-3771.
36. Kujawinski, E. B.; Behn, M. D., *Analytical Chemistry* **2006**, *78* (13), 4363-4373.
37. Sleighter, R. L.; Hatcher, P. G., *Marine Chemistry* **2008**, *110* (3-4), 140-152.
38. Leclair, J. P.; Collett, J. L.; Mazzoleni, L. R., *Environ Sci Technol* **2012**.
39. Duarte, R. M. B. O.; Duarte, A. C., *TrAC, Trends Anal. Chem.* **2011**, *30* (10), 1659-1671.
40. Williams, B. J.; Goldstein, A. H.; Kreisberg, N. M.; Hering, S. V., *Aerosol Science and Technology* **2006**, *40* (8), 627-638.

41. Schnelle-Kreis, J.; Welthagen, W.; Sklorz, M.; Zimmermann, R., *Journal of Separation Science* **2005**, 28 (14), 1648-1657.
42. Liu, Z. Y.; Patterson, D. G.; Lee, M. L., *Analytical Chemistry* **1995**, 67 (21), 3840-3845.
43. David R. Worton, N. M. K., Gabriel Isaacman, Alexander P. Teng, Christopher Mcneish, Tadeusz Gorecki, Susanne V. Hering, and Allen H. Goldstein, *Aerosol Science and Technology* **2012**, 46, 13.
44. Hamilton, J. F.; Lewis, A. C.; Carey, T. J.; Wenger, J. C., *Analytical Chemistry* **2008**, 80 (2), 474-480.
45. Muller, L.; Reinnig, M. C.; Hayen, H.; Hoffmann, T., *Rapid Communications in Mass Spectrometry* **2009**, 23 (7), 971-979.
46. Pol, J.; Hohnova, B.; Jussila, M.; Hyotylainen, T., *Journal of Chromatography A* **2006**, 1130 (1), 64-71.
47. Bond, T. C.; Doherty, S. J.; Fahey, D. W.; Forster, P. M.; Berntsen, T.; DeAngelo, B. J.; Flanner, M. G.; Ghan, S.; Karcher, B.; Koch, D.; Kinne, S.; Kondo, Y.; Quinn, P. K.; Sarofim, M. C.; Schultz, M. G.; Schulz, M.; Venkataraman, C.; Zhang, H.; Zhang, S.; Bellouin, N.; Guttikunda, S. K.; Hopke, P. K.; Jacobson, M. Z.; Kaiser, J. W.; Klimont, Z.; Lohmann, U.; Schwarz, J. P.; Shindell, D.; Storelvmo, T.; Warren, S. G.; Zender, C. S., *Journal of Geophysical Research-Atmospheres* **2013**, 118 (11), 5380-5552.
48. Shrestha, G.; Traina, S. J.; Swanston, C. W., *Sustainability* **2010**, 2 (1), 294-320.
49. Wei, Y.; Ma, L.; Cao, T.; Zhang, Q.; Wu, J.; Buseck, P. R.; Thompson, J. E., *Anal Chem* **2013**, 85 (19), 9181-9188.
50. Liu, C.; Panetta, R. L.; Yang, P., *Aerosol Science and Technology* **2012**, 46 (1), 31-43.
51. Petzold, A.; Ogren, J. A.; Fiebig, M.; Laj, P.; Li, S. M.; Baltensperger, U.; Holzer-Popp, T.; Kinne, S.; Pappalardo, G.; Sugimoto, N.; Wehrli, C.; Wiedensohler, A.; Zhang, X. Y., *Atmospheric Chemistry and Physics* **2013**, 13 (16), 8365-8379.
52. Birch, M. E.; Cary, R. A., *Aerosol Science and Technology* **1996**, 25 (3), 221-241.
53. Cavalli, F.; Viana, M.; Yttri, K. E.; Genberg, J.; Putaud, J. P., *Atmospheric Measurement Techniques* **2010**, 3 (1), 79-89.
54. Bond, T. C.; Anderson, T. L.; Campbell, D., *Aerosol Science and Technology* **1999**, 30 (6), 582-600.

55. Arnott, W. P.; Moosmuller, H.; Rogers, C. F.; Jin, T. F.; Bruch, R., *Atmospheric Environment* **1999**, *33* (17), 2845-2852.
56. Lack, D. A.; Lovejoy, E. R.; Baynard, T.; Pettersson, A.; Ravishankara, A. R., *Aerosol Science and Technology* **2006**, *40* (9), 697-708.
57. Droplet Measurement Technologies
<http://www.dropletmeasurement.com/products/carbon-sensing>.
58. Schwarz, J. P.; Gao, R. S.; Fahey, D. W.; Thomson, D. S.; Watts, L. A.; Wilson, J. C.; Reeves, J. M.; Darbeheshti, M.; Baumgardner, D. G.; Kok, G. L.; Chung, S. H.; Schulz, M.; Hendricks, J.; Lauer, A.; Karcher, B.; Slowik, J. G.; Rosenlof, K. H.; Thompson, T. L.; Langford, A. O.; Loewenstein, M.; Aikin, K. C., *Journal of Geophysical Research-Atmospheres* **2006**, *111* (D16).
59. Schwarz, J. P.; Spackman, J. R.; Gao, R. S.; Watts, L. A.; Stier, P.; Schulz, M.; Davis, S. M.; Wofsy, S. C.; Fahey, D. W., *Geophysical Research Letters* **2010**, *37*.
60. Wexler, A. S.; Seinfeld, J. H., *Atmospheric Environment* **1991**, *25A*, 2731-2748.
61. Schaap, M.; van Loon, M.; ten Brink, H. M.; Dentener, F. J.; Builtjes, P. J. H., *Atmospheric Chemistry and Physics* **2004**, *4*.
62. Alastuey, A.; Querol, X.; Rodriguez, S.; Plana, F.; Lopez-Soler, A.; Ruiz, C.; Mantilla, E., *Atmospheric Environment* **2004**, *38* (30), 4979-4992.
63. Trebs, I.; Meixner, F. X.; Slanina, J.; Otjes, R.; Jongejan, P.; Andreae, M. O., *Atmospheric Chemistry and Physics* **2004**, *4*, 967-987.
64. Cheng, Y. F.; Su, H.; Rose, D.; Gunthe, S. S.; Berghof, M.; Wehner, B.; Achtert, P.; Nowak, A.; Takegawa, N.; Kondo, Y.; Shiraiwa, M.; Gong, Y. G.; Shao, M.; Hu, M.; Zhu, T.; Zhang, Y. H.; Carmichael, G. R.; Wiedensohler, A.; Andreae, M. O.; Poschl, U., *Atmospheric Chemistry and Physics* **2012**, *12* (10), 4477-4491.
65. Wei, Y.; Zhang, Q.; Thompson, J. E., *Atmospheric Chemistry and Physics Discussions* **2013**, *13* (11), 29413-29445.
66. Weber, R. J.; Orsini, D.; Daun, Y.; Lee, Y. N.; Klotz, P. J.; Brechtel, F., *Aerosol Science and Technology* **2001**, *35* (3), 718-727.
67. Orsini, D. A.; Ma, Y. L.; Sullivan, A.; Sierau, B.; Baumann, K.; Weber, R. J., *Atmospheric Environment* **2003**, *37* (9-10), 1243-1259.
68. Noblitt, S. D.; Lewis, G. S.; Liu, Y.; Hering, S. V.; Collett, J. L.; Henry, C. S., *Anal Chem* **2009**, *81* (24), 10029-10037.

69. Sorooshian, A.; Brechtel, F. J.; Ma, Y. L.; Weber, R. J.; Corless, A.; Flagan, R. C.; Seinfeld, J. H., *Aerosol Science and Technology* **2006**, *40* (6), 396-409.
70. Jimenez, J. L.; Jayne, J. T.; Shi, Q.; Kolb, C. E.; Worsnop, D. R.; Yourshaw, I.; Seinfeld, J. H.; Flagan, R. C.; Zhang, X. F.; Smith, K. A.; Morris, J. W.; Davidovits, P., *Journal of Geophysical Research-Atmospheres* **2003**, *108* (D7).
71. Huang, X. F.; He, L. Y.; Hu, M.; Canagaratna, M. R.; Sun, Y.; Zhang, Q.; Zhu, T.; Xue, L.; Zeng, L. W.; Liu, X. G.; Zhang, Y. H.; Jayne, J. T.; Ng, N. L.; Worsnop, D. R., *Atmospheric Chemistry and Physics* **2010**, *10* (18), 8933-8945.
72. Sun, Y.; Zhang, Q.; Macdonald, A. M.; Hayden, K.; Li, S. M.; Liggio, J.; Liu, P. S. K.; Anlauf, K. G.; Leaitch, W. R.; Steffen, A.; Cubison, M.; Worsnop, D. R.; van Donkelaar, A.; Martin, R. V., *Atmospheric Chemistry and Physics* **2009**, *9* (9), 3095-3111.
73. Redmond, H. E.; Dial, K. D.; Thompson, J. E., *Aeolian Research* **2010**, *2* (1), 5-26.
74. Thompson, J. E.; Smith, B. W.; Winefordner, J. D., *Anal Chem* **2002**, *74* (9), 1962-1967.
75. Li, L.; Chen, J. M.; Chen, H.; Yang, X.; Tang, Y.; Zhang, R. Y., *Journal of Aerosol Science* **2011**, *42* (4), 277-284.
76. Dial, K. D.; Hiemstra, S.; Thompson, J. E., *Anal Chem* **2010**, *82* (19), 7885-7896.
77. Thompson, J. E.; Barta, N.; Policarpio, D.; DuVall, R., *Optics Express* **2008**, *16* (3), 2191-2205.
78. Ma, L.; Thompson, J. E., *Analytical Chemistry* **2012**, *84* (13), 5611-5617.
79. Wilson, W. E.; Chow, J. C.; Claiborn, C.; Fusheng, W.; Engelbrecht, J.; Watson, J. G., *Chemosphere* **2002**, *49* (9), 1009-1043.
80. Kroll, J. H.; Donahue, N. M.; Jimenez, J. L.; Kessler, S. H.; Canagaratna, M. R.; Wilson, K. R.; Altieri, K. E.; Mazzoleni, L. R.; Wozniak, A. S.; Bluhm, H.; Mysak, E. R.; Smith, J. D.; Kolb, C. E.; Worsnop, D. R., *Nature Chemistry* **2011**, *3* (2), 133-139.
81. Heald, C. L.; Kroll, J. H.; Jimenez, J. L.; Docherty, K. S.; DeCarlo, P. F.; Aiken, A. C.; Chen, Q.; Martin, S. T.; Farmer, D. K.; Artaxo, P., *Geophysical Research Letters* **2010**, *37* (8).
82. Donahue, N. M.; Kroll, J. H.; Pandis, S. N.; Robinson, A. L., *Atmospheric Chemistry and Physics* **2012**, *12* (2), 615-634.

83. Ng, N. L.; Canagaratna, M. R.; Zhang, Q.; Jimenez, J. L.; Tian, J.; Ulbrich, I. M.; Kroll, J. H.; Docherty, K. S.; Chhabra, P. S.; Bahreini, R.; Murphy, S. M.; Seinfeld, J. H.; Hildebrandt, L.; Donahue, N. M.; DeCarlo, P. F.; Lanz, V. A.; Prevot, A. S. H.; Dinar, E.; Rudich, Y.; Worsnop, D. R., *Atmospheric Chemistry and Physics* **2010**, *10* (10), 4625-4641.
84. Zhang, Q.; Jimenez, J. L.; Canagaratna, M. R.; Ulbrich, I. M.; Ng, N. L.; Worsnop, D. R.; Sun, Y. L., *Analytical and Bioanalytical Chemistry* **2011**, *401* (10), 3045-3067.
85. Schmitt-Kopplin, P.; Gelencser, A.; Dabek-Zlotorzynska, E.; Kiss, G.; Hertkorn, N.; Harir, M.; Hong, Y.; Gebefugi, I., *Anal Chem* **2010**, *82* (19), 8017-8026.
86. Hatch, L. E.; Creamean, J. M.; Ault, A. P.; Surratt, J. D.; Chan, M. N.; Seinfeld, J. H.; Edgerton, E. S.; Su, Y. X.; Prather, K. A., *Environ Sci Technol* **2011**, *45* (12), 5105-5111.
87. Lin, M.; Walker, C.; Khlystov, A., *Atmospheric Chemistry and Physics* **2010**, *10*, 2145-2157.
88. Wang, X. F.; Gao, S.; Yang, X.; Chen, H.; Chen, J. M.; Zhuang, G. S.; Surratt, J. D.; Chan, M. N.; Seinfeld, J. H., *Environ Sci Technol* **2010**, *44* (12), 4441-4446.
89. Froyd, K. D.; Murphy, S. M.; Murphy, D. M.; de Gouw, J. A.; Eddingsaas, N. C.; Wennberg, P. O., *Proceedings of the National Academy of Sciences of the United States of America* **2010**, *107* (50), 21360-21365.
90. Lukacs, H.; Gelencser, A.; Hoffer, A.; Kiss, G.; Horvath, K.; Hartyani, Z., *Atmospheric Chemistry and Physics* **2009**, *9* (1), 231-238.
91. Kristensen, K.; Glasius, M., *Atmospheric Environment* **2011**, *45* (27), 4546-4556.
92. Surratt, J. D.; Gomez-Gonzalez, Y.; Chan, A. W. H.; Vermeulen, R.; Shahgholi, M.; Kleindienst, T. E.; Edney, E. O.; Offenberg, J. H.; Lewandowski, M.; Jaoui, M.; Maenhaut, W.; Claeys, M.; Flagan, R. C.; Seinfeld, J. H., *Journal of Physical Chemistry A* **2008**, *112* (36), 8345-8378.
93. Stone, E. A.; Yang, L. M.; Yu, L. Y. E.; Rupakheti, M., *Atmospheric Environment* **2012**, *47*, 323-329.
94. Miyazaki, Y.; Kawamura, K.; Jung, J.; Furutani, H.; Uematsu, M., *Atmospheric Chemistry and Physics* **2011**, *11* (7), 3037-3049.
95. Roach, P. J.; Laskin, J.; Laskin, A., *Anal Chem* **2010**, *82* (19), 7979-7986.
96. Chang-Graham, A. L.; Profeta, L. T.; Johnson, T. J.; Yokelson, R. J.; Laskin, A.; Laskin, J., *Environ Sci Technol* **2011**, *45* (4), 1257-1263.

97. Mazzoleni, L. R.; Ehrmann, B. M.; Shen, X. H.; Marshall, A. G.; Collett, J. L., *Environ Sci Technol* **2010**, *44* (10), 3690-3697.
98. Altieri, K. E.; Turpin, B. J.; Seitzinger, S. P., *Atmospheric Chemistry and Physics* **2009**, *9* (7), 2533-2542.
99. Putman, A. L.; Offenberg, J. H.; Fisseha, R.; Kundu, S.; Rahn, T. A.; Mazzoleni, L. R., *Atmospheric Environment* **2012**, *46*, 164-172.
100. Zheng, J. Y.; Shao, M.; Che, W. W.; Zhang, L. J.; Zhong, L. J.; Zhang, Y. H.; Streets, D., *Environ Sci Technol* **2009**, *43* (22), 8580-8586.
101. Meylan, W. M.; Howard, P. H., *Chemosphere* **1993**, *26* (12), 2293-2299.
102. Meylan, W. M.; Howard, P. H., *Environmental Toxicology and Chemistry* **1991**, *10* (10), 1283-1293.
103. Perri, M. J.; Lim, Y. B.; Seitzinger, S. P.; Turpin, B. J., *Atmospheric Environment* **2010**, *44* (21-22), 2658-2664.
104. Loeffler, K. W.; Koehler, C. A.; Paul, N. M.; De Haan, D. O., *Environ Sci Technol* **2006**, *40* (20), 6318-6323.
105. De Haan, D. O.; Corrigan, A. L.; Tolbert, M. A.; Jimenez, J. L.; Wood, S. E.; Turley, J. J., *Environ Sci Technol* **2009**, *43* (21), 8184-8190.
106. De Haan, D. O.; Tolbert, M. A.; Jimenez, J. L., *Geophysical Research Letters* **2009**, *36*.
107. Chang, J. L.; Thompson, J. E., *Atmospheric Environment* **2010**, *44* (4), 541-551.
108. Sun, Y. L.; Zhang, Q.; Anastasio, C.; Sun, J., *Atmospheric Chemistry and Physics* **2010**, *10* (10), 4809-4822.
109. Finlayson-Pitts, B. J.; Pitts, J. N., *Chemistry of the upper and lower atmosphere : theory, experiments and applications*. **2000**.
110. Bowman, F. M.; Odum, J. R.; Seinfeld, J. H.; Pandis, S. N., *Atmospheric Environment* **1997**, *31* (23), 3921-3931.
111. Pankow, J. F., *Atmospheric Environment* **1987**, *21* (11), 2275-2283.
112. Williams, B. J.; Goldstein, A. H.; Kreisberg, N. M.; Hering, S. V., *Proceedings of the National Academy of Sciences of the United States of America* **2010**, *107* (15), 6676-6681.

113. Rubel, G. O., *Atmospheric Environment Part a-General Topics* **1991**, 25 (5-6), 1009-1012.
114. Khan, I.; Brimblecombe, P., *Journal of Aerosol Science* **1992**, 23 (Supplement 1), 897-900.
115. Atkinson, R., *Atmospheric Environment* **2000**, 34 (12-14), 2063-2101.
116. Atkinson, R., *Atmospheric Chemistry and Physics* **2003**, 3, 2233-2307.
117. <http://kinetics.nist.gov/kinetics/index.jsp>.
118. <http://kinetics.nist.gov/solution/>.
119. Neeb, P., *Journal of Atmospheric Chemistry* **2000**, 35 (3), 295-315.
120. Atkinson, R., *International Journal of Chemical Kinetics* **1987**, 19 (9), 799-828.
121. Meylan, W. M.; Howard, P. H., *Environmental Toxicology and Chemistry* **2003**, 22 (8), 1724-1732.
122. Atkinson, R., *Atmospheric Environment* **2007**, 41 (38), 8468-8485.
123. Pfrang, C.; King, M. D.; Canosa-Mas, C. E.; Wayne, R. P., *Atmospheric Environment* **2006**, 40 (6), 1170-1179.
124. Oberg, T., *Atmospheric Environment* 2005, 39 (12), 2189-2200.
125. Gramatica, P.; Pilutti, P.; Papa, E., *Journal of Chemical Information and Computer Sciences* **2004**, 44 (5), 1794-1802.
126. Wang, Y. N.; Chen, J. W.; Li, X. H.; Wang, B.; Cai, X. Y.; Huang, L. P., *Atmospheric Environment* **2009**, 43 (5), 1131-1135.
127. Dutot, A. L.; Rude, J.; Aumont, B., *Atmospheric Environment* **2003**, 37 (2), 269-276.
128. Monod, A.; Doussin, J. F., *Atmospheric Environment* **2008**, 42 (33), 7611-7622.
129. Nguyen, T. B.; Bateman, A. P.; Bones, D. L.; Nizkorodov, S. A.; Laskin, J.; Laskin, A., *Atmospheric Environment* **2010**, 44 (8), 1032-1042.
130. Bateman, A. P.; Nizkorodov, S. A.; Laskin, J.; Laskin, A., *Physical Chemistry Chemical Physics* **2009**, 11 (36), 7931-7942.
131. Virtanen, A.; Joutsensaari, J.; Koop, T.; Kannosto, J.; Yli-Pirila, P.; Leskinen, J.; Makela, J. M.; Holopainen, J. K.; Poschl, U.; Kulmala, M.; Worsnop, D. R.; Laaksonen, A., *Nature* **2010**, 467 (7317), 824-827.

132. Koppmann, R. E., *Volatile Organic Compounds in the Atmosphere*. Wiley-Blackwell: **2007**.
133. Kroll, J. H.; Smith, J. D.; Che, D. L.; Kessler, S. H.; Worsnop, D. R.; Wilson, K. R., *Physical Chemistry Chemical Physics* **2009**, *11* (36), 8005-8014.
134. Lambe, A. T.; Onasch, T. B.; Croasdale, D. R.; Wright, J. P.; Martin, A. T.; Franklin, J. P.; Massoli, P.; Kroll, J. H.; Canagaratna, M. R.; Brune, W. H.; Worsnop, D. R.; Davidovits, P., *Environ Sci Technol* **2012**, *46* (10), 5430-5437.
135. Buseck, P. R.; Adachi, K.; Gelencsér, A.; Tompa, É.; Pósfai, M., *Atmospheric Chemistry and Physics Discussions* **2012**, *12* (9), 24821-24846.
136. Adachi, K.; Buseck, P. R., *Atmospheric Chemistry and Physics* **2008**, *8* (21), 6469-6481.
137. Moffet, R. C.; Prather, K. A., *Proceedings of the National Academy of Sciences of the United States of America* **2009**, *106* (29), 11872-11877.
138. Adachi, K.; Buseck, P. R., *Journal of Geophysical Research-Atmospheres* **2013**, *118* (9), 3723-3730.
139. McConnell, J. R.; Edwards, R.; Kok, G. L.; Flanner, M. G.; Zender, C. S.; Saltzman, E. S.; Banta, J. R.; Pasteris, D. R.; Carter, M. M.; Kahl, J. D., *Science* **2007**, *317* (5843), 1381-1384.
140. Kaden, D. A.; Hites, R. A.; Thilly, W. G., *Cancer Res* **1979**, *39* (10), 4152-4159.
141. Gotze, H. J.; Schneider, J.; Herzog, H. G., *Fresenius Journal of Analytical Chemistry* **1991**, *340* (1), 27-30.
142. Olson, K. L.; Harris, S. J.; Weiner, A. M., *Combustion Science and Technology* **1987**, *51* (1-3), 97-102.
143. Sunset Laboratory Home Page. <http://www.sunlab.com> (accessed Feb 1, 2013).
144. Borak, J.; Sirianni, G.; Cohen, H. J.; Chemerynski, S.; Wheeler, R., *Aiha Journal* **2003**, *64* (2), 260-268.
145. Miyazaki, Y.; Kondo, Y.; Sahu, L. K.; Imaru, J.; Fukushima, N.; Kano, M., *Journal of Environmental Monitoring* **2008**, *10* (10), 1195-1201.
146. Magee Scientific Home Page. <http://www.mageesci.com>
147. Stephens, M.; Turner, N.; Sandberg, J., *Applied Optics* **2003**, *42* (19), 3726-3736.
148. Thomson, K., *Applied Physics B-Lasers and Optics* **2009**, *96* (4), 581-581.

149. Droplet Measurement Technologies
<http://www.dropletmeasurement.com/products/carbon-sensing-instruments/sp2.html>
150. Wofsy, S. C.; Team, H. S.; Team, C. M.; Team, S., *Philosophical Transactions of the Royal Society a-Mathematical Physical and Engineering Sciences* **2011**, 369 (1943), 2073-2086.
151. Adler, G.; Riziq, A. A.; Erlick, C.; Rudich, Y., *Proceedings of the National Academy of Sciences of the United States of America* **2010**, 107 (15), 6699-6704.
152. Bond, T. C.; Bergstrom, R. W., *Aerosol Science and Technology* **2006**, 40 (1), 27-67.
153. Chylek, P.; Lesins, G. B.; Videen, G.; Wong, J. G. D.; Pinnick, R. G.; Ngo, D.; Klett, J. D., *Journal of Geophysical Research-Atmospheres* **1996**, 101 (D18), 23365-23371.
154. Fuller, K. A.; Malm, W. C.; Kreidenweis, S. M., *Journal of Geophysical Research-Atmospheres* **1999**, 104 (D13), 15941-15954.
155. Mikhailov, E. F.; Vlasenko, S. S.; Podgorny, I. A.; Ramanathan, V.; Corrigan, C. E., *Journal of Geophysical Research-Atmospheres* **2006**, 111 (D7).
156. Zhang, R. Y.; Khalizov, A. F.; Pagels, J.; Zhang, D.; Xue, H. X.; McMurry, P. H., *Proceedings of the National Academy of Sciences of the United States of America* **2008**, 105 (30), 10291-10296.
157. Bond, T. C.; Habib, G.; Bergstrom, R. W., *Journal of Geophysical Research-Atmospheres* **2006**, 111 (D20).
158. Schnaiter, M.; Linke, C.; Mohler, O.; Naumann, K. H.; Saathoff, H.; Wagner, R.; Schurath, U.; Wehner, B., *Journal of Geophysical Research-Atmospheres* **2005**, 110 (D19).
159. Cappa, C. D.; Onasch, T. B.; Massoli, P.; Worsnop, D. R.; Bates, T. S.; Cross, E. S.; Davidovits, P.; Hakala, J.; Hayden, K. L.; Jobson, B. T.; Kolesar, K. R.; Lack, D. A.; Lerner, B. M.; Li, S. M.; Mellon, D.; Nuaaman, I.; Olfert, J. S.; Petaja, T.; Quinn, P. K.; Song, C.; Subramanian, R.; Williams, E. J.; Zaveri, R. A., *Science* **2012**, 337 (6098), 1078-1081.
160. Thompson, J. E.; Hayes, P. L.; Jimenez, J. L.; Adachi, K.; Zhang, X. L.; Liu, J. M.; Weber, R. J.; Buseck, P. R., *Atmospheric Environment* **2012**, 55, 190-200.
161. Ma, L. L.; Thompson, J. E., *Anal Chem* **2012**, 84 (13), 5611-5617.
162. Thompson, J. E., *GIT Lab. J.* **2010**, 9-10.

163. Subramanian, R.; Kok, G. L.; Baumgardner, D.; Clarke, A.; Shinozuka, Y.; Campos, T. L.; Heizer, C. G.; Stephens, B. B.; de Foy, B.; Voss, P. B.; Zaveri, R. A., *Atmospheric Chemistry and Physics* **2010**, *10* (1), 219-237.
164. Slowik, J. G.; Cross, E. S.; Han, J. H.; Davidovits, P.; Onasch, T. B.; Jayne, J. T.; Williams, L. R.; Canagaratna, M. R.; Worsnop, D. R.; Chakrabarty, R. K.; Moosmuller, H.; Arnott, W. P.; Schwarz, J. P.; Gao, R. S.; Fahey, D. W.; Kok, G. L.; Petzold, A., *Aerosol Science and Technology* **2007**, *41* (3), 295-314.
165. Michelsen, H. A.; Tivanski, A. V.; Gilles, M. K.; van Poppel, L. H.; Dansson, M. A.; Buseck, P. R., *Applied Optics* **2007**, *46* (6), 959-977.
166. Vander Wal, R. L.; Ticich, T. M.; Stephens, A. B., *Applied Physics B-Lasers and Optics* **1998**, *67* (1), 115-123.
167. Kruger, V.; Wahl, C.; Hadeff, R.; Geigle, K. P.; Stricker, W.; Aigner, M., *Measurement Science & Technology* **2005**, *16* (7), 1477-1486.
168. Stipe, C. B.; Choi, J. H.; Lucas, D.; Koshland, C. P.; Sawyer, R. F., *Journal of Nanoparticle Research* **2004**, *6* (5), 467-477.
169. Clegg, S. L.; Brimblecombe, P.; Wexler, A. S., *Journal of Physical Chemistry A* **1998**, *102* (12), 2137-2154.
170. Qian, F.; Ma, L.; Thompson, J. E., *Journal of the European Optical Society-Rapid Publications* **2012**, *7*.
171. Khalizov, A. F.; Xue, H. X.; Wang, L.; Zheng, J.; Zhang, R. Y., *Journal of Physical Chemistry A* **2009**, *113* (6), 1066-1074.
172. Laborde, M.; Crippa, M.; Tritscher, T.; Juranyi, Z.; Decarlo, P. F.; Temime-Roussel, B.; Marchand, N.; Eckhardt, S.; Stohl, A.; Baltensperger, U.; Prevot, A. S. H.; Weingartner, E.; Gysel, M., *Atmospheric Chemistry and Physics* **2013**, *13* (11), 5831-5856.
173. Liu, D.; Allan, J.; Whitehead, J.; Young, D.; Flynn, M.; Coe, H.; McFiggans, G.; Fleming, Z. L.; Bandy, B., *Atmospheric Chemistry and Physics* **2013**, *13* (4), 2015-2029.
174. Liu, D.; Flynn, M.; Gysel, M.; Targino, A.; Crawford, I.; Bower, K.; Choulaton, T.; Juranyi, Z.; Steinbacher, M.; Huglin, C.; Curtius, J.; Kampus, M.; Petzold, A.; Weingartner, E.; Baltensperger, U.; Coe, H., *Atmospheric Chemistry and Physics* **2010**, *10* (15), 7389-7407.
175. Matsui, H.; Koike, M.; Kondo, Y.; Moteki, N.; Fast, J. D.; Zaveri, R. A., *Journal of Geophysical Research-Atmospheres* **2013**, *118* (5), 2304-2326.

176. Metcalf, A. R.; Craven, J. S.; Ensberg, J. J.; Brioude, J.; Angevine, W.; Sorooshian, A.; Duong, H. T.; Jonsson, H. H.; Flagan, R. C.; Seinfeld, J. H., *Journal of Geophysical Research-Atmospheres* **2012**, *117*.
177. Moteki, N.; Kondo, Y.; Miyazaki, Y.; Takegawa, N.; Komazaki, Y.; Kurata, G.; Shirai, T.; Blake, D. R.; Miyakawa, T.; Koike, M., *Geophysical Research Letters* **2007**, *34* (11).
178. Niu, H. Y.; Shao, L. Y.; Zhang, D. Z., *Atmospheric Environment* **2011**, *45* (16), 2699-2703.
179. Schwarz, J. P.; Gao, R. S.; Spackman, J. R.; Watts, L. A.; Thomson, D. S.; Fahey, D. W.; Ryerson, T. B.; Peischl, J.; Holloway, J. S.; Trainer, M.; Frost, G. J.; Baynard, T.; Lack, D. A.; de Gouw, J. A.; Warneke, C.; Del Negro, L. A., *Geophysical Research Letters* **2008**, *35* (13).
180. Shiraiwa, M.; Kondo, Y.; Moteki, N.; Takegawa, N.; Miyazaki, Y.; Blake, D. R., *Geophysical Research Letters* **2007**, *34* (16).
181. Bueno, P. A.; Havey, D. K.; Mulholland, G. W.; Hodges, J. T.; Gillis, K. A.; Dickerson, R. R.; Zachariah, M. R., *Aerosol Science and Technology* **2011**, *45* (10), 1217-1230.
182. Lack, D. A.; Cappa, C. D.; Cross, E. S.; Massoli, P.; Ahern, A. T.; Davidovits, P.; Onasch, T. B., *Aerosol Science and Technology* **2009**, *43* (10), 1006-1012.
183. Nessler, R.; Weingartner, E.; Baltensperger, U., *Journal of Aerosol Science* **2005**, *36* (8), 958-972.
184. Saathoff, H.; Naumann, K. H.; Schnaiter, M.; Schock, W.; Mohler, O.; Schurath, U.; Weingartner, E.; Gysel, M.; Baltensperger, U., *Journal of Aerosol Science* **2003**, *34* (10), 1297-1321.
185. Schnaiter, M.; Horvath, H.; Mohler, O.; Naumann, K. H.; Saathoff, H.; Schock, O. W., *Journal of Aerosol Science* **2003**, *34* (10), 1421-1444.
186. Shiraiwa, M.; Kondo, Y.; Iwamoto, T.; Kita, K., *Aerosol Science and Technology* **2010**, *44* (1), 46-54.
187. Xue, H. X.; Khalizov, A. F.; Wang, L.; Zheng, J.; Zhang, R. Y., *Physical Chemistry Chemical Physics* **2009**, *11* (36), 7869-7875.
188. Liu, S., Aiken, A. C., Gorkowski, K., Dubey, M., Herndon, S., Williams, L., Massoli, P., Fort-ner, E., Freedman, A., Worsnop, D. R., Ng, N. L., Mohr, C., Lopez-Hilfiker, F., Thornton, J., Allan, J., and Cappa, C. D., *32nd Annual Conference AAAR* **2013**, 393.

189. Jacobson, M. Z., *Science* **2013**, 339 (6118), 393.
190. Ramana, M. V., Ramanathan, V., Feng, Y., Yoon, S.-C., Kim, S.-W., Carmichael, G. R., Schauer, J. J., *Nature Geoscience* **2010**, 3, 542-545.
191. Ramanathan, V.; Vogelmann, A. M., *Ambio* **1997**, 26 (1), 38-46.
192. Redmond, H.; Thompson, J. E., *Physical Chemistry Chemical Physics* **2011**, 13 (15), 6872-6882.
193. Zadoo, S.; Thompson, J. E., *J Environ Monit* **2011**, 13 (11), 3294-3297.
194. ten Brink, H. M.; Khlystov, A.; Kos, G. P. A.; Tuch, T.; Roth, C.; Kreyling, W., *Atmospheric Environment* **2000**, 34 (25), 4291-4300.
195. Carrico, C. M.; Rood, M. J.; Ogren, J. A., *Journal of Geophysical Research-Atmospheres* **1998**, 103 (D13), 16565-16574.
196. Cropper, P. M.; Hansen, J. C.; Eatough, D. J., *Journal of the Air & Waste Management Association* **2013**, 63 (9), 1004-1011.
197. Kus, P.; Carrico, C. M.; Rood, M. J.; Williams, A., *Journal of Atmospheric and Oceanic Technology* **2004**, 21 (7), 981-994.
198. Liu, X. G.; Zhang, Y. H.; Cheng, Y. F.; Hu, M.; Han, T. T., *Atmospheric Environment* **2012**, 60, 59-67.
199. Lukacs, H.; Gelencser, A.; Hammer, S.; Puxbaum, H.; Pio, C.; Legrand, M.; Kasper-Giebl, A.; Handler, M.; Limbeck, A.; Simpson, D.; Preunkert, S., *Journal of Geophysical Research-Atmospheres* **2007**, 112 (D23).
200. Shapiro, E. L.; Szprengiel, J.; Sareen, N.; Jen, C. N.; Giordano, M. R.; McNeill, V. F., *Atmospheric Chemistry and Physics* **2009**, 9 (7), 2289-2300.
201. Jacobson, M. Z., *Journal of Geophysical Research-Atmospheres* **2012**, 117.
202. Pan, X. L.; Yan, P.; Tang, J.; Ma, J. Z.; Wang, Z. F.; Gbaguidi, A.; Sun, Y. L., *Atmospheric Chemistry and Physics* **2009**, 9 (19), 7519-7530.
203. Swietlicki, E.; Hansson, H. C.; Hameri, K.; Svenningsson, B.; Massling, A.; McFiggans, G.; McMurry, P. H.; Petaja, T.; Tunved, P.; Gysel, M.; Topping, D.; Weingartner, E.; Baltensperger, U.; Rissler, J.; Wiedensohler, A.; Kulmala, M., *Tellus Series B-Chemical and Physical Meteorology* **2008**, 60 (3), 432-469.

204. Massoli, P.; Bates, T. S.; Quinn, P. K.; Lack, D. A.; Baynard, T.; Lerner, B. M.; Tucker, S. C.; Brioude, J.; Stohl, A.; Williams, E. J., *Journal of Geophysical Research-Atmospheres* **2009**, 114.
205. Santarpia, J. L.; Gasparini, R.; Li, R. J.; Collins, D. R., *Journal of Geophysical Research-Atmospheres* **2005**, 110 (D3).
206. Yaws, C. L., *The Yaw's Handbook of Vapor Pressure Antoine Coefficients*. Gulf Publishing: **2007**.